Università degli Studi di Torino
Scuola di Dottorato in Scienze della Natura
e Tecnologie Innovative

Effects of Rotation in Turbulent Systems

Francesco Toselli

Università degli Studi di Torino
Scuola di Dottorato in Scienze della Natura
e Tecnologie Innovative

Dottorato in Fisica ed Astrofisica

Effects of Rotation in Turbulent Systems

Francesco Toselli

Tutor: Guido Boffetta

Effects of Rotation in Turbulent Systems

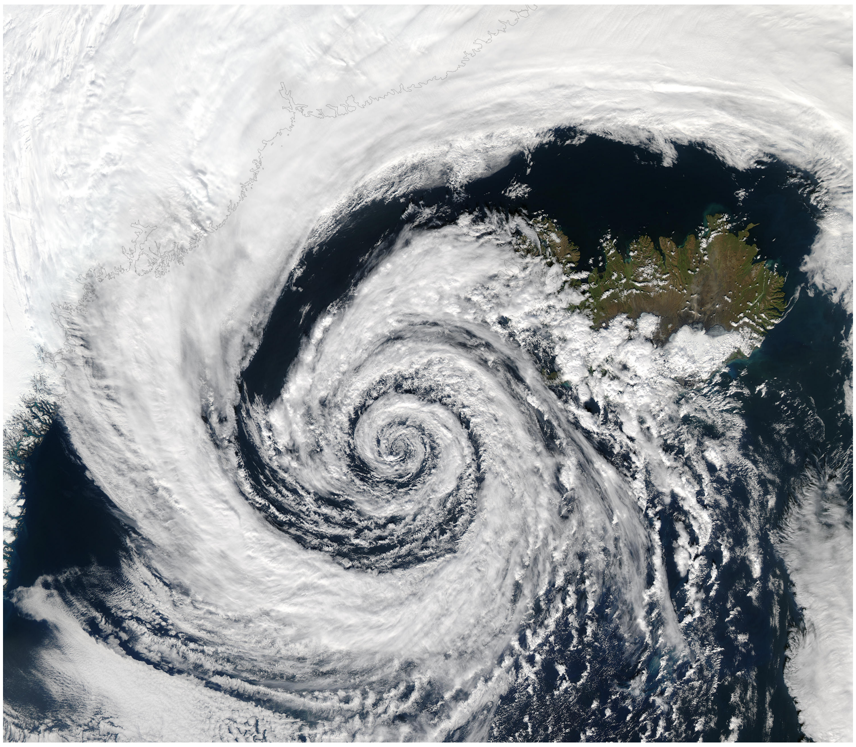

Turin, Italy
April 2021

Francesco Toselli

Abstract

Turbulence subjected to rotation is present in a wide range of natural phenomena, including geophysical and astrophysical flows, and engineering applications. In general, rotation affects the structure and the dynamics of turbulence through the Coriolis force, which also tends to make the flow two-dimensional via the Taylor-Proudman theorem. From a theoretical point of view, rotating turbulence is an active field of research, with many open questions in particular when combined with other ingredients such as confinement or stratification.

The project of this thesis, which has been developed in the period of three years, relies on the study of the effects of rotation on a turbulent flow in a simple homogeneous configuration in the absence of (or far from) boundaries. This simplification aims at understanding the effects induced directly by rotation without the complications produced by other ingredients.

The purpose of the thesis is to reach a physical understanding on how diverse turbulent systems can be affected by different rotation intensity. In particular, motivated by the important role played in atmospheric and oceanic environment, we investigate three particular effects induced by rotation, i.e. the asymmetry between cyclones and anticyclones, the formation of columnar structures and the role of rotation on the turbulent dimensional transition.

The work in this thesis is based on both laboratory experiments and direct numerical simulations, with also the development of data analysis software and the optimization of extisting codes.
Laboratory experiments have been performed in the TurLab facility in Turin where the experimental apparatus consists of a 6m diameter rotating platform, which is one of the largest in the world and allows to investigate the behavior of large scale motions and turbulent flows subjected to solid body rotation.
Numerical simulations are based on a series of codes which integrate the

Navier-Stokes equations in periodic boxes with pseudo-spectral methods. Additional terms, such as the Coriolis acceleration, and fields, i.e. an active temperature field in the Boussinesq approximations, have been also considered. Numerical code are fully parallelized with MPI protocol and have been runned on several architectures, mainly including MARCONI and GALILEO supercomputers, available at the High Performance Computing (HPC) department of CINECA which is the main italian supercomputing center.

More in detail, this thesis is made of three parts:
Part I consists of an introduction to the basic concepts of turbulence theory (Chapter 1) and to the principal action of rotation on a generic flow (Chapter 2). These two chapters are meant to provide the reader with the tools able to clarify the results presented in the last part.

Part II introduces the experimental tools I used and the numerical methods implemented in the models. Here the focus is on the Turin laboratory where I conducted experiments of turbulence under rotation, with the analysis tools exploited (Chapter 3). Furthermore, a brief overview on the numerical methods is discussed, describing my code implementation in order to improve and optimize the computational efficiency (Chapter 4).

Part III collects the results of the work done during the PhD which led to three publications on international journals (one in submission) and represents the core of the present thesis.

- Chapter 5: G. Boffetta, F. Toselli, M. Manfrin, S. Musacchio, Cyclone–anticyclone asymmetry in rotating thin fluid layers , *Journal of Turbulence*, 1 (2020).
  https://doi.org/10.1080/14685248.2020.1855352

- Chapter 6: F. Toselli, S. Musacchio and G. Boffetta, Effects of rotation on the bulk turbulent convection, *Journal of Fluid Mechanics*, 881, 648 (2019).
  https://doi.org/10.1017/jfm.2019.764

- Chapter 7: S. Musacchio, F. Toselli, G. Boffetta, The kolmogorov flow in a rotating frame - in preparation

The first work (presented in Chapter 5) addresses the problem of the asymmetry between the statistics of cyclones and anticyclones in rotating turbulent flows by a combination laboratory experiments and direct numerical simulations. The main result of our work indicates that rotation, combined with the flow confinement, can retard the developing of such asymmetry. Moreover in spite of some flow structural differences between experiments and numerical simulation, mainly related to their boundary conditions, the observed effects on the cyclone-anticyclone asymmetry statistics are similar.

In the second work (Chapter 6) we study the effect of rotation on turbulent heat transfer. In detail the behavior of an unbounded system, where homogeneous turbulent convection is produced by a mean vertical temperature gradient, is investigated by means of direct numerical simulations of bulk turbulent convection. Here we find that the quasi-bidimensionalization of the flow and the formation of vertical columnar structures, due to rotation, produce strong correlations between temperature and vertical velocity. These elements seem to be responsible for the observed increase of the heat transport inside the system.

Finally, in Chapter 7 we study the effect of rotation on the a simple channel flow given by the celebrated Kolmogorov flow. Here, we mainly consider the action of rotation on the mean flow and its impact on the friction and stress coefficient variation. Furthermore, a comparison between the velocity and stress vector orientation is presented, showing that their alignment is strongly influenced by the rotation intensity.

Acknowledgements - Ringraziamenti

Vorrei innanzitutto ringraziare Guido Boffetta, il mio supervisor, per la sua totale disponibilità e pazienza. Grazie per i suoi preziosi insegnamenti e la sua comprensione in ogni circostanza.
Il secondo ringraziamento va a Stefano Musacchio: con la sua costante presenza e continua attenzione mi ha sempre infuso fiducia e sicurezza. Inoltre la sua disponibilità, le lunghe chiamate su Skype e i suoi numerosi consigli sono sempre stati fondamentali e illuminanti.
Grazie anche a Filippo De Lillo per avermi supportato (e sopportato) per diversi anni in ufficio. Grazie per i momenti di confronto, per la sua immensa disponibilità e per la sua immancabile allegria nella professionalità.
Vorrei inoltre ringraziare Miguel Onorato con cui ho avuto l'opportunità di lavorare in progetti paralleli che hanno inoltre portato al deposito di un brevetto. Questo piccolo traguardo raggiunto insieme è stato per me una grande soddisfazione.
Grazie a loro per avermi trasmesso tutte le conoscenze acquisite in questo settore.

Desidero ringraziare in modo particolare Matteo: è stato per me un collega e un amico con cui ho condiviso la maggior parte dei dubbi, dei problemi, ma anche delle soddisfazioni e dei risultati. Grazie inoltre ad Alessandro, Giovanni, Francesco, Marta e Leonardo con cui ho condiviso parti differenti del mio percorso di ricerca universitaria.
Grazie agli amici di sempre: a quelli più vicini e a quelli che mi han lasciato troppo presto. Tutti loro sono sempre stati per me fonte di sostegno.

Grazie infine alla mia famiglia: ai miei genitori che mi hanno sempre sostenuto e supportato incondizionatamente in ogni mia scelta.
A te, Sonia che sei diventata la mia nuova famiglia: per essere sempre al mio fianco, credendo in me ogni singolo istante. Il tuo amore e la tua pazienza mi hanno sempre permesso di superare ogni difficoltà...insieme.

Contents

List of Figures

Part I

Turbulence, Dimensions & Rotation

Chapter 1

Introduction to turbulence

Turbulent phenomena are observed every day and appear in flows of different scales and sizes: from large-scale processes such as the atmospheric jets or oceanic currents, to local problems such as a pipe flow or the efficiency of a wind turbine. From a theoretical point of view, turbulence can be defined as a state in a physical system, out of equilibrium, with a large number of degrees of freedom, characterized by spatial and temporal disorder usually associated with a random and chaotic flow. Turbulence is generated by an excess of kinetic energy injection in fluid flow, which overcomes the damping effect of the fluid's viscosity. The scale of injection, where the turbulence is excited, usually differs strongly from the scale of damping, where dissipation takes place. Moreover the nonlinear interations strongly act in the so-called inertial range by transferring energy from larger scales (injection scale) towards smaller ones (damping scale). These various "active scales", the transfer of energy through a cascade-like process and the presence of dynamically conserved quantities are the turbulence key features and represent the crucial issue in turbulence. Indeed, those characteristics produce a mixing enhancement and an unpredictability of fluid motion even if we know the initial conditios of the system. For this complex nature of turbulent flows, problems can rarely be solved analytically and so we have to rely on experimental studies or numerical simulations using a statistical analysis. Even if the classical physics laws that rule the turbulent behaviour are well known equations, nowadays a full understanding of turbulence is still missing. The first person that studied and tried to describe turbulence through his observations was Leonardo da Vinci in the XV century; after him, in the XIX century, the works of L. Euler, L. M. H. Navier, G. G. Stokes, L. F. Richardson and O. Reynolds have given the basis of turbulence as research field. Finally in the last century, N. Kolmogorov strongly influenced the research field by introducing the first statistical theory and significantly changing the turbulence problem approach. His work in 1941 remains a major source of inspiration for turbulent research.

1.1 Navier-Stokes equations

The dynamics of an incompressible fluid is determined by the well known Navier-Stokes equations:

$$\partial_t \boldsymbol{u} + \boldsymbol{u} \cdot \nabla \boldsymbol{u} = -\frac{1}{\rho} \nabla p + \nu \nabla^2 \boldsymbol{u} + \boldsymbol{f} \tag{1.1}$$

$$\nabla \cdot \boldsymbol{u} = 0 \tag{1.2}$$

In these equations, derived by L. M. H. Navier and G. G. Stokes in the early 1800's, $\boldsymbol{u} = (u, v, w)$ represents the velocity field of the fluid assumed incompressible with equation 1.2, p is the pressure, ρ the fluid density, $\nu = \frac{\mu}{\rho}$ is its kinematic viscosity (with μ its dynamic viscosity) and $\boldsymbol{f}$ represents the sum of the external forces per unit mass which supports the system motion. The Navier-Stokes equations take origin from the conservation of mass and momentum per unit volume; moreover their different terms represent respectively:

- $\boldsymbol{u} \cdot \nabla \boldsymbol{u}$ the non-linear term or inertial term which is responsible for the trasnfer of kinetic energy in the turbulent cascade.
- $-\frac{\nabla p}{\rho}$ the pressure gradients which guarantee the incompressibility of the flow. They are determined by the Poisson equation

  $$\partial^2 p = -\rho \partial_i \partial_j u_i u_j \tag{1.3}$$

  which is obtained by taking the divergence of equation 1.1.
- $\nu \nabla^2 \boldsymbol{u}$ the viscous term, proportional to viscosity. It acts mainly at smaller scales by dissipating energy, so it is easy to understand that it is the dominant term in the laminar regime and it tends to stop the flow motion in absence of the forcing term $\boldsymbol{f}$.

In order to solve the Navier-Stokes equations 1.1, both initial conditions and boundary conditions are needed. To achieve the maximum symmetry in the system, it is advantageous not to have any boundaries: in this way one can assume that the fluid fills all the $\mathbb{R}^3$ space. However, the boundlessness of the space can lead to mathematical issues. For this reason, to simply overcome the problem, it is quite typical to deal with periodic boundary conditions in the space variable $\boldsymbol{r} = (x, y, z)$:

$$\boldsymbol{u}(x + aL, y + bL, z + cL) = \boldsymbol{u}(x, y, z) \tag{1.4}$$

for every integer value of a, b, c and for all x, y, z. In this way the flow is restricted to a periodic box of extension L (where $L \in \mathbb{R}$ is a positive number, called period) such as: $0 \leq x < L, 0 \leq y < L, 0 \leq z < L$.

With the periodic boundary conditions it's quite easy to show that the pressure term can be eliminated from Navier-Stokes equations 1.1 by using the Poisson equation 1.3 [36]. By going from the $\boldsymbol{r}$-$space$ (physical space) to the $\boldsymbol{k}$-$space$ (Fourier space) one can write the pressure using Fourier series:

$$p(\boldsymbol{r}) = \sum_{\boldsymbol{k}} e^{i\boldsymbol{k}\cdot\boldsymbol{r}} \hat{p}_{\boldsymbol{k}} \tag{1.5}$$

therefore, from eq.1.3 we obtain

$$\hat{p}_{\boldsymbol{k}} = -\frac{k_i k_j}{k^2} (u_j \hat{u}_i)(\boldsymbol{k}), k \neq 0 \tag{1.6}$$

where k is the modulus of the wavevector $\boldsymbol{k}$. Finally, after returning in the physical space, the expression of the pressure is

$$p(\boldsymbol{r}) = \nabla^{-2} \partial_i \partial_j (u_i u_j) \tag{1.7}$$

consequently the Navier-Stokes equations can be rewritten as

$$\partial_t u_i + (\delta_{il} - \nabla^{-2} \partial_i \partial_l) \partial_j (u_j u_l) = \nu \nabla^2 u_i \tag{1.8}$$

by imposing the divergence conditions 1.2.

An alternative way to elimitate the non-local pressure term is to introduce the vorticity, defined as $\boldsymbol{\omega} = \nabla \times \boldsymbol{u}$. The vorticity field equation of motion is now derived by taking the curl of the Navier-Stokes equations 1.1, then using the identity $\boldsymbol{u} \cdot \nabla \boldsymbol{u} = \frac{1}{2} \nabla |\boldsymbol{u}|^2 - \boldsymbol{u} \times (\nabla \times \boldsymbol{u})$, obtaining the following equation:

$$\partial_t \boldsymbol{\omega} + (\boldsymbol{u} \cdot \nabla) \boldsymbol{\omega} = (\boldsymbol{\omega} \cdot \nabla) \boldsymbol{u} + \nu \nabla^2 \boldsymbol{\omega} \tag{1.9}$$

The left hand side of this equation represents the convective derivatives of the vorticity, while on the right hand side of the equation we have the non linear term $(\boldsymbol{\omega} \cdot \nabla) \boldsymbol{u}$, also called the vortex-stretching term, that implies lengthening of vortices associated with a corresponding increase of the vorticity component in the stretching direction. The last contribution to the equation is brought by the dissipative term.

1.1.1 Reynolds number

Equation 1.1 can be made non-dimensional by introducing a characteristic length scale L and a specific velocity U of the flow. If we consider a simple case of a pipe flow: L can be identified as the diameter of the pipe and U as the mean-flow velocity. In this way, taking the density equal to 1 by rescaling the pressure, we can get:

$$\partial_t \boldsymbol{u} + \boldsymbol{u} \cdot \nabla \boldsymbol{u} = -\nabla p + \frac{1}{Re}\nabla^2 \boldsymbol{u} + \boldsymbol{f} \tag{1.10}$$

where $Re = \frac{UL}{\nu}$ is the definition of the famous Reynolds number that gives a measure of the nonlinearity of the system. This adimensional number is the only control parameter of the flow and was introduced by Osborne Reynolds in 1883, who showed that a transition between laminar and turbulent flow occurs when the Re number reaches a critical value [81]. This value depends on the geometries of the flow, but the crucial thing is that the transition from laminar to turbulent flow always occurs near the critical Reynolds as seen in figure 6.3.

The Reynolds number is defined as the ratio between the inertial forces and the viscous ones:

$$\frac{UL}{\nu} \sim \frac{\boldsymbol{u} \cdot \nabla \boldsymbol{u}}{\nu \nabla^2 \boldsymbol{u}} \tag{1.11}$$

Due to its mathematical definition, we can have a laminar regime when the viscosity dominates over the inertial term while the so called fully developed turbulence is achieved in the opposite case or in the ideal limit in which $\nu \to 0$ and $Re \to \infty$. In the transition from laminar regime to fully developed turbulence, symmetries that characterize the Navier-Stokes equations (see [36]) are firstly broken and then, at very high Reynolds number, all or some

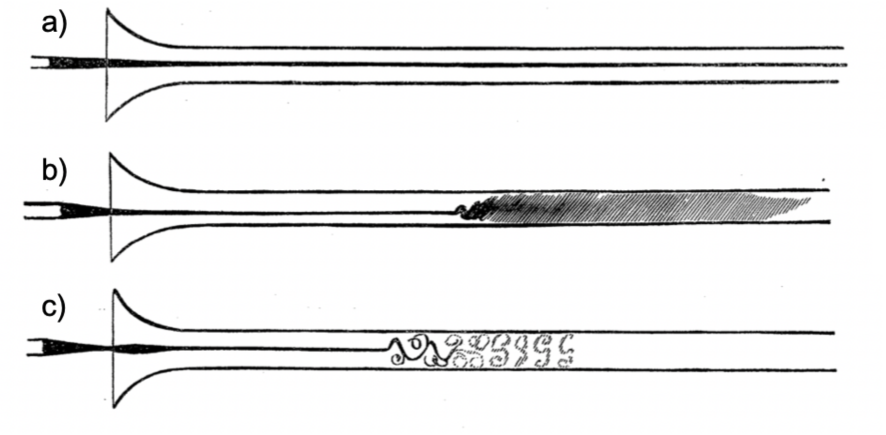

Figure 1.1: Original sketches by Reynolds work [81]. In his experiments water flows through a horizontal pipe where some dye is added in order to visualize the flow. From top to bottom the Reynolds number is increased and the system evolves from laminar (a) to turbulent (c) after the critical value is exceeded.

of them are restored in a statistical sense when fully developed turbulence is reached.

1.1.2 Conservation laws

In turbulence is important to discuss the global conservation laws, involving the integration over the entire volume occupied by the fluid. As in the previous section, periodic boundary conditions 1.4 are assumed and angular brackets $\langle ... \rangle$ are used to denote averages over the periodic box.
The main known conservaton laws are:

- The conservation of momentum
$$\frac{d}{dt}\langle \boldsymbol{u} \rangle = 0 \tag{1.12}$$
- The conservation of energy
$$\frac{d}{dt}\langle \frac{1}{2}\boldsymbol{u}^2 \rangle = -\nu \langle \boldsymbol{\omega}^2 \rangle \tag{1.13}$$
where $\boldsymbol{\omega} = \nabla \times \boldsymbol{u}$.
- The conservation of helicity
$$\frac{d}{dt}\langle \frac{1}{2}\boldsymbol{u} \cdot \boldsymbol{\omega} \rangle = -\nu \langle \boldsymbol{\omega} \cdot \nabla \times \boldsymbol{\omega} \rangle \tag{1.14}$$

All these laws can be easily proven: for the momentum conservation all terms of 1.1, being spatial derivatives of periodic functions, vanish when the average is taken and the only terms that survives is the temporal derivative $\partial_t u_i$. For the energy relation one can multiply 1.1 by u_i and use the incompressibility 1.2; after averaging over space the pressure term and the nonlinear term go to zero because they are evaluated at the boundaries after being integrated by parts. Moreover, since boundaries and functions are periodic, the identity $\langle \boldsymbol{u} \cdot \nabla^2 \boldsymbol{u} \rangle = -\langle \nabla \times \boldsymbol{u} \cdot \nabla \times \boldsymbol{u} \rangle$ is used to rewrite the viscous term. Finally, the helicity balance relation can be proven by taking the scalar product between the vorticity equation 1.9 and the vector $\boldsymbol{u}$ and averaging over space: the only term that survives is the viscous one, expressed by the known identity $\langle \boldsymbol{u} \cdot \nabla^2 \boldsymbol{\omega} \rangle = -\langle \nabla \times \boldsymbol{u} \cdot \nabla \times \boldsymbol{\omega} \rangle$.
At this point some important notation can be introduced:

$$\begin{aligned} E &\equiv \langle \frac{1}{2}|\boldsymbol{u}|^2 \rangle \\ Z &\equiv \langle \frac{1}{2}|\boldsymbol{\omega}|^2 \rangle \\ H &\equiv \langle \frac{1}{2}\boldsymbol{u} \cdot \boldsymbol{\omega} \rangle \end{aligned} \tag{1.15}$$

where E^1 is the mean energy, Z the mean enstrophy and H the mean helicity. With these new quadratic quantities defined in 1.15, the energy and helicity balance equations can be expressed as:

$$\frac{d}{dt}E = -2\nu Z, \qquad \frac{d}{dt}H = -2\nu H_\omega \tag{1.16}$$

where the quantity $H_\omega \equiv \langle \frac{1}{2}\boldsymbol{\omega} \cdot \nabla \times \boldsymbol{\omega} \rangle$ represents the mean vertical vorticity. The energy balance shows that, for $\nu = 0$ and in the abscence of other external forcing, the dynamics conserve the kinetic energy which is, under this conditions, an inviscid invariant. Furthermore, one of the most frequently used quantities in turbulence is the so called *energy dissipation rate*

$$\epsilon \equiv -\frac{dE}{dt} \tag{1.17}$$

that in the limit of $\nu \to 0$ does not vanish but reaches a constant value equal to $\lim_{\nu\to 0} 2\nu Z$. This phenomenon is known as dissipative anomaly and implies that, in order to mantain the energy dissipation finite, the total enstrophy needs to diverge as $Z \propto \nu^{-1}$ by compensating the decreasing viscosity. The enstrophy growth, in three dimensions, is phisically explained by the vortex stretching term that produces diverging velocity gradient in the limit $Re \to \infty$. In two dimensions, instead the enstrophy is conserved because the vortex-stretching term goes to zero.

1.1.3 Energy budget

As shown in the global energy balance 1.13 the nonlinear term in Navier–Stokes equation does not change the total kinetic energy. Nevertheless it has a primary role in turbulence, because it is responsible for the energy redistribution among the various scales of motion: such energy transfer between different modes is the origin of the turbulent cascade.

In order to describe the transfer of energy we need a qualitative definition for the concept of *scale*: if a typical turbulent flow image (characterized by greater structures and smaller ones like filaments or small eddies) is shown through a slide projector, the very high quality details of the image can be blurred by going out of focus where only greater structures can be appreciated. This defocusing is equivalent to a filtering which can act by attenuating or removing high harmonics in the the spatial Fourier decomposition of the image. The cutoff K of the filtering obviously depends on the chosen defocusing and is associated with a scale $\ell \sim K^{-1}$.

---

[1] It is actually the mean energy per unit mass, but considering an incompressible fluid with constant density the distinction is not important.

In the same way the idea can be mathematically formalized introducing the Fourier series of a periodic function f

$$f(\boldsymbol{r}) = \sum_{\boldsymbol{k}} e^{i\boldsymbol{k}\cdot\boldsymbol{r}} \hat{f}_{\boldsymbol{k}} \tag{1.18}$$

and defining respectively the low-pass and the high-pass filtered function:

$$f_K^<(\boldsymbol{r}) = \sum_{\boldsymbol{k} \leq K} e^{i\boldsymbol{k}\cdot\boldsymbol{r}} \hat{f}_{\boldsymbol{k}} \qquad f_K^>(\boldsymbol{r}) = \sum_{\boldsymbol{k} > K} e^{i\boldsymbol{k}\cdot\boldsymbol{r}} \hat{f}_{\boldsymbol{k}} \tag{1.19}$$

where the length $\ell \sim K^{-1}$ is the scale of the filtering. In this way only frequencies above or below the threshold cutoff K are filtered. The example in figure 1.2 clarifies the idea of low/high-pass filtering.

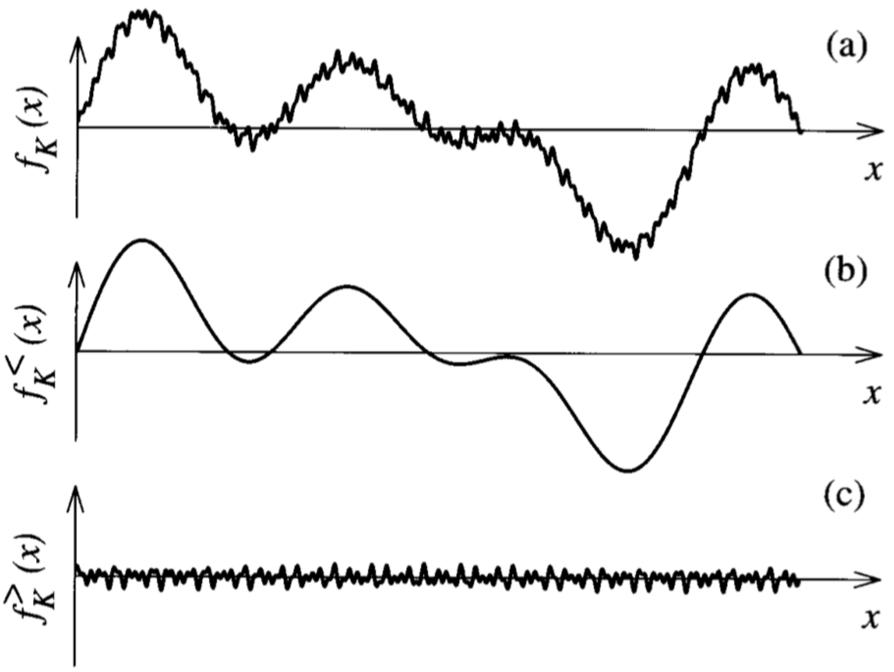

Figure 1.2: A signal (a) where a low-pass filtering (b) and a high-pass filtering (c) are applied.

In three-dimensional turbulence, under periodic boundaries conditions, the same concept of filtering can be used on the velocity field by defining the functions $\boldsymbol{u}_K^<(\boldsymbol{r})$ and $\boldsymbol{u}_K^>(\boldsymbol{r})$ which represent eddies of scale greater than ℓ and eddies of scale smaller than ℓ.

Such notation can be used to study the energy budget of the low-pass filtered velocity field: indeed by taking the scalar product of $\boldsymbol{u}_K^<$ with the Navier-Stokes equation written for the relative low-filtered velocity field, and then semplifying some terms using periodicity and vector identities, one can collects the remaining terms to obtain the scale-by-scale energy budget equation:

$$\partial_t \mathcal{E}_K = -\Pi_K - 2\nu\Omega_K + \mathcal{F}_K \tag{1.20}$$

where $\mathcal{E}_K \equiv \frac{1}{2}\langle|\boldsymbol{u}_K^<|^2\rangle$ is the cumulative energy, $\Omega_K \equiv \frac{1}{2}\langle|\boldsymbol{\omega}_K^<|^2\rangle$ the cumulative enstrophy and $\mathcal{F}_K \equiv \langle \boldsymbol{f}_K^< \cdot \boldsymbol{u}_K^< \rangle$ is the cumulative energy injection due to the forcing. All these terms are defined between wavenumber 0 and K.
Finally, the flux of energy through wavenumber K is described with $\Pi_K \equiv \langle \boldsymbol{u}_K^< \cdot (\boldsymbol{u}_K^< \cdot \nabla \boldsymbol{u}_K^>)\rangle + \langle \boldsymbol{u}_K^< \cdot (\boldsymbol{u}_K^> \cdot \nabla \boldsymbol{u}_K^>)\rangle$ and represents the amount of energy that flows towards smaller scales due to nonlinear interactions.
To sum up, the equation 1.20 shows that the energy variation in time, at scales smaller than $\ell \sim K^{-1}$, is equal to the energy injection at such specific scales ($\mathcal{F}_K$) minus the energy flux towards smaller scales (Π_K) and minus the energy dissipation ($2\nu\Omega_K$). In a classical fully developed turbulent system, where high Reynolds number are reached, there is a remarkable scale separation between large scales where the energy is injected and the small scales where dissipation localizes: in the so called inertial range (the intermediate range of scale) the energy is conserved and transferred scale-by-scale.

1.2 Turbulence phenomenology

In the previous section the role of the nonlinear term in Navier–Stokes equation is explained to correspond to an energy transfer in Fourier space between modes, in the inertial range. Using another approach, which consists of a simple dimensional analysis of the Navier-Stokes equation, one can understand the essential phenomenology of turbulence.

1.2.1 Richardson cascade

The basics of turbulence phenomenology can be described by the concept of turbulent cascade proposed by Richardson in 1920. In figure 1.3 the whole process is described: initially some kinetic energy is injected at large scales by an external forcing which allows the formation of eddies of size ℓ_0. Due to the fluid motions, these eddies are stretched and deformed until they reach smaller scales through a process of breaking. This process is repeated and the energy continues to flow towards smaller scales forming smaller structures. At the end, when enough small scales are reached, the viscosity acts dissipating eddies in form of heat.
Let us now consider u_ℓ the mean flow velocity at scale ℓ, $\tau_\ell \sim \ell/u_\ell$ the time at the relative scale required to transfer energy from ℓ-scale eddies to smaller ones and $\tau_\ell^{diss} \sim \ell^2/\nu$ the time required by the viscous term to dissipate the kinetic energy of a ℓ-scale eddie. At this point, one can identify three different range of scales:

- **Injective range**: corresponds to the large scales (ℓ_0) where the external forcing injects the kinetic energy.

- **Inertial range**: where the energy is conserved and transported to smaller scales. Here the time required for energy transfer is still shorter than the dissipative time $\tau_\ell << \tau_\ell^{diss}$.
- **Dissipative range**: when the time required for energy transfer becomes of the same order of the dissipative time. In this range the energy dissipation starts to overcome the transfer and the energy cascade is stopped.

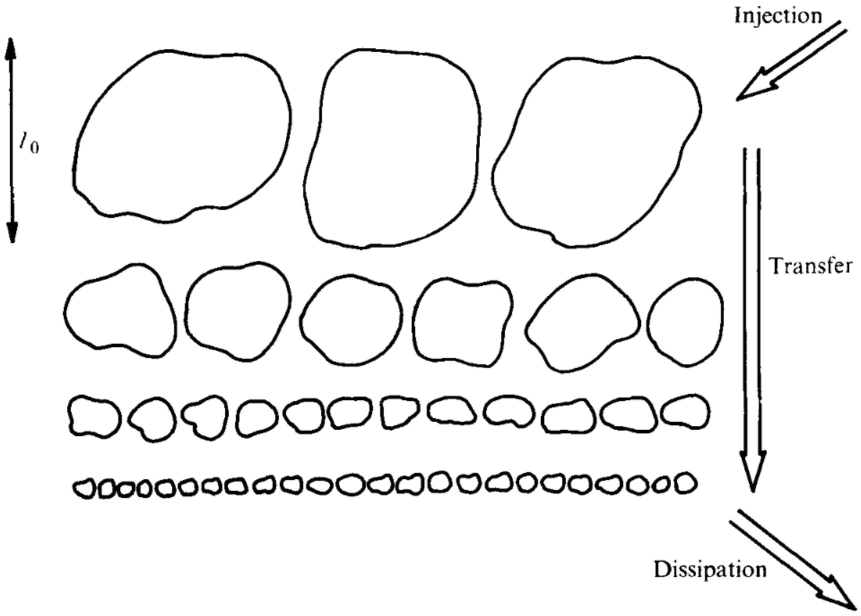

Figure 1.3: Sketch of the turbulent cascade, described by the celebrated rhyming verse by Richardson: *"Big whorls have little whorls that feed on their velocity, and little whorls have lesser whorls and so on to viscosity"*.

A simple dimensional analysis, by looking at the energy at scale ℓ, i.e. $E(\ell) \propto u_\ell^2$, allows to identify the Kolmogorov scaling laws. Indeed, the energy dissipation rate can be written as:

$$\varepsilon \sim \frac{E(\ell)}{\tau_\ell} \sim u_\ell^2 \frac{u_\ell}{\ell} \tag{1.21}$$

that does not depend on the viscosity ν. As a consequence, the characteristic Kolmogorov scalings for times and velocities are respectively:

$$u_\ell \sim \varepsilon^{1/3} \ell^{1/3}, \qquad \tau_\ell \sim \varepsilon^{-1/3} \ell^{2/3} \tag{1.22}$$

The so called Kolmogorov scale η, is finally identified as the scale under which the linear viscous term dominates the fluid motions. Once the border between the inertial and the dissipative range is reached, indeed, the dissipative time

τ_ℓ^{diss} is equivalent with the transfer time τ_ℓ and the Kolmogorov scale can be define as:

$$\eta \sim \nu^{3/4} \varepsilon^{-1/4} \tag{1.23}$$

As said before, increasing the Re number and mantaining a constant forcing at the larger scale, the inertial range is extended. The portion of the system in this range is far from both the forcing and the dissipative range; here turbulence properties are universal because they are independent on how the system dissipates energy and how the latter is produced at larger scales.

1.2.2 Kolmogorov theory (K41)

Inspired by the Richardson qualitative concept of cascade, in 1941 Kolmogorov defined a theoretical framework for turbulence, now known as the K41 theory. His theory is proposed under specific hypotheses and applies to homogenous and isotropic turbulence (i.e. statistically invariant under translation and rotation of the coordinates reference frame). Nevertheless, his original work is still considered the only approach that provides the best description of turbulence.
The K41 work is made quantitative thanks to some assumptions:

- *In the limit of infinite Reynolds, all symmetries are restored in a statistical sense at small scales.*
  This is the hypothesis of local isotropy: small scales are defined as ($\ell \ll \ell_0$), where ℓ_0, called the integral scale, is characteristic of the production of turbulence. Moreover, the homogeneity at small scales is defined in terms of velocities increments:

  $$\delta \boldsymbol{u}(\boldsymbol{r}, \boldsymbol{\ell}) \equiv \boldsymbol{u}(\boldsymbol{r} + \boldsymbol{\ell}) - \boldsymbol{u}(\boldsymbol{r}) \tag{1.24}$$

  and means that also the velocity fluctuations remain invariant for space translation (i.e. $\delta \boldsymbol{u}(\boldsymbol{r} + \boldsymbol{r}', \boldsymbol{\ell}) = \delta \boldsymbol{u}(\boldsymbol{r}, \boldsymbol{\ell})$).

- *In the limit of infinite Reynolds, the turbulent flow is self-similar at small scales.*
  This is the self-similarity hypothesis: thus, there exists a unique scaling exponent $h \in \mathbb{R}$ such that

  $$\delta \boldsymbol{u}(\boldsymbol{r}, \lambda \boldsymbol{\ell}) = \lambda^h \delta \boldsymbol{u}(\boldsymbol{r}, \boldsymbol{\ell}) \tag{1.25}$$

  for every $\boldsymbol{r}$ and $\boldsymbol{\ell}$ in the limit where $\lambda \ell \ll \ell_0$.

- *In the limit of infinite Reynolds, the turbulent flow has a finite nonvanishing mean rate of energy dissipation ε.*

Moreover, we can define the longitudinal structure function, i.e. the p-th moment of the velocity increments, as:

$$S_p(\ell) = \langle (\delta u_{||})^p \rangle \tag{1.26}$$

where $\delta \boldsymbol{u}_{||}(\boldsymbol{r}, \boldsymbol{\ell}) = \delta \boldsymbol{u}(\boldsymbol{r}, \boldsymbol{\ell}) \cdot \boldsymbol{\ell}/|\boldsymbol{\ell}|$ is the longitudinal velocity increment. Using the Karman-Howarth-Monin relation, Kolmogorov obtained an exact result for the third order structure function:

$$S_3(\ell) = \langle (\delta u_{||})^3 \rangle = -\frac{4}{5}\varepsilon \ell \tag{1.27}$$

The equation 1.27 represents the famous four-fifths law that allows to fix the value for the scaling exponent $h = 1/3$ and to write the generic structure function scaling law

$$S_p(\ell) = C_p \varepsilon^{\frac{p}{3}} \ell^{\frac{p}{3}} \tag{1.28}$$

by using the self-similarity hipothesis. Here C_p are all dimensionless unknown constant, except for $C_3 = -4/5$ that is a universal constant since the four-fifths law holds without any need to assume self-similarity.
Starting from 1.28 a particular case can be derived, when $p = 2$, for the second order structure function, introducing the well known two-third law:

$$S_2(\ell) = C_2 \varepsilon^{\frac{2}{3}} \ell^{\frac{2}{3}} \tag{1.29}$$

This relation equals the so called five-third law for the energy spectrum

$$E(k) \equiv 2\pi k \langle |\hat{\boldsymbol{u}}(\boldsymbol{k})|^2 \rangle \sim \varepsilon^{\frac{2}{3}} k^{-\frac{5}{3}} \tag{1.30}$$

An analogue derivation can be done by using dimensional arguments: with the same assumption of a constant, non-vanishing, rate of energy dissipation written as $\varepsilon \sim u_\ell^3/\ell$, one can write

$$u_\ell \sim \varepsilon^{\frac{1}{3}} \ell^{\frac{1}{3}} \tag{1.31}$$

obtaining again the two-third law

$$\langle \delta u_\ell^2 \rangle \sim \varepsilon^{\frac{2}{3}} \ell^{\frac{2}{3}} \tag{1.32}$$

A simple explanation is presented in figure 1.4 where all energetic ranges of a three-dimensional turbulent system are shown, including the five-third spectrum power law scaling. Moreover, equation 1.28 and 1.30 are fairly well supported by experimental and numerical data.
All these scaling relations are intended for the application within the inertial range, where scales are much smaller than the scales at which turbulence is produced and much larger than the Kolmogorov dissipation scale η at which

direct energy dissipation becomes relevant. Focusing on the range between the inertial and the dissipation range, the time, velocity and length scale can be introduced:

$$\begin{aligned} \tau_\eta &\equiv \left(\frac{\nu}{\varepsilon}\right)^{1/2} \\ u_\eta &\equiv (\varepsilon\nu)^{1/4} \\ \eta &\equiv \left(\frac{\nu^3}{\varepsilon}\right)^{1/4} \end{aligned} \tag{1.33}$$

Moreover, looking at the Reynolds number at the Kolmogorov scale, one can get $Re_\eta = \eta u_\eta/\nu = 1$, and understand that this scale is characterized by dissipative eddies which stop the energy cascade. Finally, in order to understand how many scales are involved in the turbulent system, the ratios between the integral and the Kolmogorov scale can be computed: keeping in mind that $\varepsilon \sim u_{\ell_0}^3/\ell_0$ one can express the ratios in terms of Reynolds number

$$\begin{aligned} \tau_{\ell_0}/\tau_\eta &\sim Re^{1/2} \\ u_{\ell_0}/u_\eta &\sim Re^{1/4} \\ \ell_0/\eta &\sim Re^{3/4} \end{aligned} \tag{1.34}$$

understanding that, as Reynolds increases, the ratio between scales η/ℓ_0 decreases. Thus, in fully developed turbulence, the inertial range is confirmed to be composed by a large amount of scales.

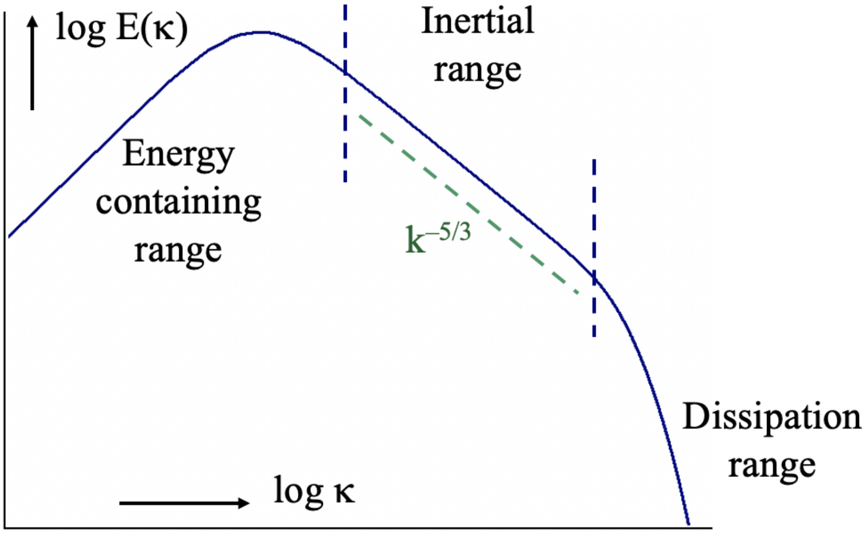

Figure 1.4: Sketch of the turbulent spectrum, with the inertial range scaling law characterized by the slope $\propto k^{-5/3}$, generally observed in turbulence.

1.3 Turbulence and dimensions

Changing the system from three towards two dimension implies radical alteration in the flow turbulent behaviour. Indeed, new phenomena can arise and be observed when we consider a two-dimensional or quasi-two-dimensional flow.

Two-dimensional turbulence describes the behaviour of high-Reynolds-number solutions of Navier–Stokes equation which depends only on two coordinates (e.g., horizontal (x, y) components). In this case, the third component of the velocity follows an advection-diffusion equation without back-reaction on the horizontal flow. Hence, without loss of generality, one may assume that the velocity has only two components.

The classical theory of two-dimensional turbulence derives from the works of Batchelor and Kraichnan [4, 55], which showed that the conservation of vorticity along the streamlines, which occurs in two dimensions, produces crucial changes in the behaviour of turbulence. Moreover, the study of incompressible two-dimensional flows at high Reynolds numbers presents several reasons of interest. One field of study is understanding the physics of plasma, where turbulent plasma flows can be confined by strong magnetic fields and can be described by the two-dimensional magnetohydrodynamics [8]. However the principal reason for studying two-dimensional, or quasi-two-dimensional flows, is due to its crucial role in understanding geophysical flows like oceans or the atmosphere. Indeed, because of the two effects of stratification and earth rotation, their intermediate-scale dynamics can be approximated and described as a two-dimensional flow.

From a computational point of view, the Navier–Stokes equation in two dimensions has the important feature to be less demanding respect to the three-dimensional one; this allows to reach higher Re numbers in numerical simulations. Moreover, besides being a simpler version of the three dimensional system, two-dimensional turbulence shows totally different characteristics which lead to new observable phenomena, such as the inverse energy cascade or the formation of coherent vortices from an initial vorticity disorder. All these topics are discussed in next sections.

1.3.1 The two-dimension vorticity equation

Considering a two dimensional system, one can express the incompressible velocity field u in terms of the stream function ψ as:

$$\boldsymbol{u} = (\partial_y \psi, -\partial_x \psi) \tag{1.35}$$

At this point, the vorticity field, defined as the curl of velocity field, $\omega = \nabla \times \boldsymbol{u}$, in two dimensions has only one non-zero component which is the one orthogonal to the horizontal velocity plane and is related to the streamfunction by

$$\omega = -\nabla^2\psi \tag{1.36}$$

Thus, it is convenient to rewrite the two-dimensional Navier–Stokes equation in terms of the vorticity scalar field:

$$\partial_t \boldsymbol{\omega} + \boldsymbol{u} \cdot \nabla \boldsymbol{\omega} = \nu \nabla^2 \boldsymbol{\omega} + \boldsymbol{f}_\omega \tag{1.37}$$

where the term $\boldsymbol{f}_\omega$ represents an external force acting as a source of enstrophy on the largest scales. By compensating the viscous dissipation with this forcing term, the equation allows to reach a statistical stationary state.
As a consequence of having only one non-zero vorticity component, the vorticity equation, previously written in three dimensions, looses its non-linear vortex stretching term: the next section explains the presence of new system invariances and different flow characteristics.

1.3.2 Invariances and turbulent cascades in two dimensions

The main difference with the three-dimensional case is the conservation of vorticity along fluid trajectories when viscosity and external forcing are ignored. The origin of this phenomenon is due to the vanishing, in two dimensions, of the so-called *vortex stretching term* $(\boldsymbol{\omega} \cdot \nabla)\boldsymbol{u}$ of equation 1.9 that appears as a forcing term in the evolution equation for vorticity in the three-dimensional case where it is responsible for the unbounded growth of enstrophy in the limit $Re \to \infty$. Hence, in the absence of external friction and forcing and in the inviscid limit $\nu = 0$ the vorticity equation simply shows that the material derivative of the vorticity vanishes along the fluid trajectories.

$$\frac{D\omega}{Dt} = \partial_t \omega + \boldsymbol{u} \cdot \nabla \omega = 0 \tag{1.38}$$

Thus, since the vortex stretching is absent, implies that the vorticity of the considered flow is globally conserved and consequently, also the total enstrophy Z which is the integral of the square vorticity 1.15, becomes a new inviscid quadratic invariant of the flow. Moreover, assuming periodic boundary conditions and in absence of external forcing $f = 0$, in two dimensions the enstrophy is constrained by the energy balance equation, which is obtained from the vorticity Navier-Stokes equation 1.37.
In contrast to the three-dimensional case, in two-dimensional turbulence the viscous dissipation of energy vanishes in the limit $Re \to \infty$ (i.e., $\nu \to 0$)

$$\lim_{\nu \to 0} -2\nu Z = \lim_{\nu \to 0} \frac{dE}{dt} = 0 \tag{1.39}$$

so it is impossible to have a cascade of energy with constant flux toward small scales. Moreover, the presence of two different quadratic flow invariants (i.e., the energy and the enstrophy) totally modifies the picture of the turbulent cascade. The comprehension of the new cascades phenomena in two-dimensional turbulence was given by Kraichnan in the sixties [55], discovering the double cascade process. On one hand enstrophy plays the role of the energy in three-dimension being mainly transferred to smaller scales (high wavenumbers) where it is dissipated by viscosity, while on the other hand the energy is transported to large scales (lower wavenumbers).
As well as in the three-dimensional case, the scaling laws in both cascades can be obtained from dimensional analysis of Navier–Stokes equation. For the inverse energy cascade, one can assume the constant energy flux $\Pi(\ell) = -\varepsilon$ towards large scales: this reproduces the same scaling laws for velocity obtained in the three-dimnesional case 1.31. Hence, the prediction for the energy spectrum of the *inverse energy cascade* remains:

$$E(k) = C\varepsilon^{\frac{2}{3}}k^{-\frac{5}{3}} \tag{1.40}$$

Physically, the inverse energy cascade brings to the formation of large clusters vortices, with sizes of the injection range, which are continuously generated by the forcing. Shortly after they are formed, they get distorted and strained by the action of other neighboring eddies, and thus tend to aggregate with other eddies of same vorticity sign. For this reason, the presence of forcing as a constant energy input for a long time combined with an abscence of large-scale energy dissipation, can lead to a motion of energy at large scales which eventually reaches the integral scale and accumulates at low wave numbers. If the system does not present a friction terms, able to dissipate the accumulated energy, the formation of a condensate [26, 70] (which is a phenomenon similar to the Bose-Einstein condensation) can be observed. Numerically, one can overcome the problem by introducing a friction term $-\alpha\omega$ in the vorticity equation 1.37 which is physically argued with the presence of the Ekman friction in thin layers [76]. In the experiments energy is dissipated by the friction produced along the walls that bound the system.
Conversely, an analogue of the K41 energy cascade towards small scales, in the sense that the transfer develops at constant rate across the scales, is the direct enstrophy cascade [4]. Indeed, considering scales smaller than the forcing one can mantain the same assumption of a constant enstrophy flux $\varepsilon_\omega = Z(\ell)/\tau_\ell$ and obtain different scaling laws. Indeed, considering that the enstrophy of an ℓ-size eddie can be estimated as $Z(\ell) \sim u_\ell^2/\ell^2$, the velocities scaling law will be:

$$u_\ell \sim \varepsilon_\omega^{\frac{1}{3}}\ell \tag{1.41}$$

and the prediction for the energy spectrum of the *direct enstrophy cascade* reads

$$E(k) = C' \varepsilon_\omega^{\frac{2}{3}} k^{-3} \tag{1.42}$$

On physical grounds, the process prevailing in the cascade is essentially the elongation of the vorticity structures [36].

A scheme of the double cascade process can be seen in figure 1.5 where respectively the direct enstrophy cascade and the inverse energy cascade are represented.

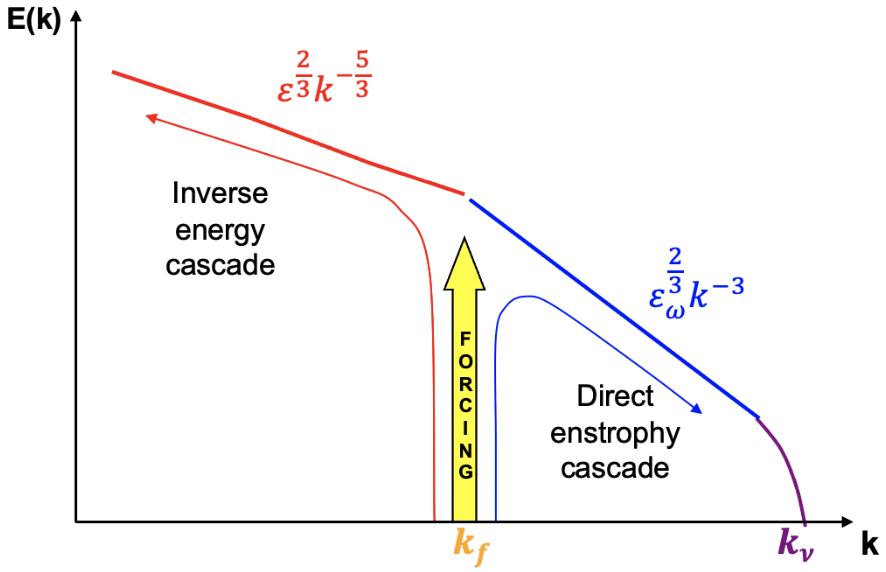

Figure 1.5: Scheme of a forced two dimensional turbulence spectrum: in red the inverse energy cascade characterized by the slope $\propto k^{-5/3}$, in blue the direct enstrophy cascade characterized by the slope $\propto k^3$.

1.3.3 Coherent structures

In two-dimensional or quasi-two-dimensional turbulence decay, the transfer of energy towards large scales (i.e., inverse energy cascade) brings to the formation of coherent structures and vortices which organize from a starting background disorder. Initially the flow organizes into a limited number of coherent vortices which contains most of the system vorticity and that are surrounded by a background of incoherent structures at smaller scales, with lower vorticity. As the time grows, two vortices of the same vorticity sign can be advected one near the other and they can merge in a bigger one with the result of a decay in the total vortices number [94]. The final stage will be the formation of a condensate [85, 26, 70] where only a vorticiy dipole survives: this dipole can then decay because of diffusion. Typical environmental systems when this structures can be observed are the atmosphere [74] and the ocean where often are subjected to the formation of this large scales vortices [59]. The study of this structures is crucial to be able to improve the modelling and better understand our climate and weather. As we see in the next section, the presence of the Coriolis force in the system can induce a strong bidimensionalization of the flow and hence brings to the formation of self-organized coherent structures.

Chapter 2

Rotation

The presence of the Earth's rotation means that we continuously experience an apparent force known as the Coriolis force. This force leads to a deflection of the wind direction to the right in the northern hemisphere and to the left in the southern hemisphere. The reason why the wind-flow around low and high-pressure systems circulates in opposing directions in each hemisphere is explained by the presence of the rotation.

The effects of rotation on turbulence concern all domains of fluid dynamics. In typical natural or industrial situations, rotation is often coupled with other dynamical factors such as shear flow deformation, buoyancy (e.g., atmospheric and oceanic motion), or other factors like combustion. According to these various and complex situations, there is much to be gained by understanding the specific role of rotation in the absence of any other external mechanisms. Moreover, rotation also causes a bidimensionalization of the flow leading to a possible change in the characteristics of the system. The study of rotating flows is therefore interesting from the point of view of both topological flow structure and turbulence modelling in many different fields such as astrophysics, engineering (e.g. turbomachinery), but most of all in geophysics where oceanic and atmospherical motion flow are studied to understand our Earth and to better predict our climate.

2.1 The Coriolis force

It is crucial to realize that this force becomes more and more important when applied to global-scale motions in the atmosphere and ocean, because of the much larger spatial scales involved respect to our everyday experience like for example the carousel. For instance, the mean motions of the upper layers of the ocean can be understood, in a first approximation, as a balance between the main driving force (e.g., density gradients and wind drag) and the Coriolis force which enters as the results of the Earth rotation.

To understand how the Coriolis force arises, one can consider a body of mass m at the equator that is stationary respect to the solid Earth. With a planet rotation with an angular velocity Ω, in an external reference frame the mass will have a linear velocity ΩR, where R is the Earth radius. If now the body moves polewards on the globe surface, with no friction and along the meridian direction, it will present a smaller velocity Ωr with r corresponding to the smaller distance from the rotation axis. In this way the mass will appear, to an observer on the rotating system, to be moving with a relative velocity $u = \Omega(R - r)$ and if it continues to move at higher latitudes with a constant velocity, it will be observed to accelerate eastwards. The force responsible of this acceleration is the Coriolis force.

The magnitude of the Coriolis force f can easily be obtained starting from the conservation of the angular momentum $I = m\Omega r^2$. Indeed it needs to apply a torque equal to the variation of angular momentum:

$$\frac{dI}{dt} = \frac{d}{dt}(m\Omega r^2) = 2m\Omega r\frac{dr}{dt} = rf \tag{2.1}$$

Considering the polar coordinates for a poleward velocity u we also have $\frac{dr}{dt} = \frac{dy}{dt}sin\Phi = vsin\Phi$, where Φ is the latitude.

The intensity of the Coriolis force per unit mass reads:

$$f = 2\Omega usin\Phi \tag{2.2}$$

with its vector relation being $\boldsymbol{f} = 2\boldsymbol{\Omega} \times \boldsymbol{u}$. Hence, considering a poleward-motion, the force is perpendicular to the displacement and deviates towards east in either hemisphere. Conversely, for a motion away from the pole in either hemisphere, the body is accelerated in the opposite direction.

2.1.1 Geostrophic balance

Geostrophic balance is arguably the most central concept in atmosphere physic, physical oceanography and also in the study of dynamical meteorology [77, 98]. It is important to realize that, although higher-order processes are responsible for all the interesting dynamics, almost all large-scale flows in the atmosphere and ocean are in geostrophic balance to a leading order. The only place where geostrophic balance never occurs is at the equator, where there is no Coriolis force. Indeed, considering the Navier-Stokes equation in presence of the Coriolis forces, the momentum budget reads:

$$\partial_t \boldsymbol{u} + \boldsymbol{u} \cdot \nabla \boldsymbol{u} = -\frac{1}{\rho} \nabla p + \nu \nabla^2 \boldsymbol{u} - 2\boldsymbol{\Omega} \times \boldsymbol{u} \tag{2.3}$$

In this equation, we consider a large scale current in either ocean or atmosphere, it is easy to consider the two horizontal component and see that the contribution terms of pressure gradient and Coriolis forces are almost always much larger than the other terms, such as molecular viscous forces. Thus, it seems to be completely justifiable to neglect friction and other time derivative terms which should be enormously greater to be able to compensate the force of pressure and rotation.

Making this approximation, the remaining terms in the Navier-Stokes equation are the pressure forces $\frac{-1}{\rho}\nabla p$ and the rotation term $2\boldsymbol{\Omega} \times \boldsymbol{u}$ that can balance each other. Hence, considering the equation 2.3 for the two horizontal components, respectively x and y, one obtains the geostrophic equation:

$$\begin{aligned} \frac{\partial p}{\partial x} &= f\rho v \\ \frac{\partial p}{\partial y} &= -f\rho u \end{aligned} \tag{2.4}$$

where u and v are the two horizontal velocity components, while f is the Coriolis force at 2.2.

This is called the geostrophic balance: with this assumption one can calculate the internal pressure field from the density distribution using the hydrostatic approximation and this horizontal pressure gradient can be used to predict the velocity field.

In order to understand how geostrophic balance emerges, one can describe a moving fluid parcel that starts to be accelerated because of a pressure gradients between two different regions. As the parcel moves, it is deflected by the Coriolis force that operates in a direction perpendicular to the direction of the current, until it flows parallel to the isobars: here the pressure gradient and the Coriolis force cancel each other. In conclusion, a key feature of geostrophic balance is that rather than flowing from high to low pressure, the fluid actually moves parallel to lines of equal pressure (Fig. 2.1). Using this feature, ocean currents velocities can be estimated from altimetry satellite data only by knowing the pressure field distribution [101]

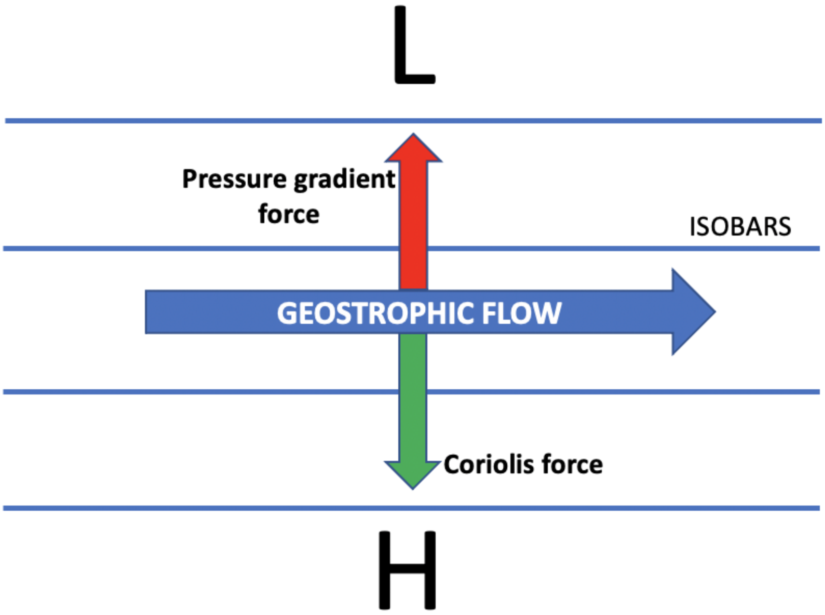

Figure 2.1: Scheme of a geostrophic flow currents which follows the isobars, showing a balance between pressure and Coriolis forces. Viewing in the direction of the flow, low pressure region is to the left and high pressure region is to the right.

2.1.2 Rossby and Ekman number

The time, space and velocity scales are crucial in determining the relevance of the Coriolis force. Whether rotation is important in a system can be determined by its Rossby number, which is defined as the ratio between the inertial forces and the Coriolis ones, respectively represented in the Navier-Stokes equations as $\boldsymbol{u} \cdot \nabla \boldsymbol{u} \sim \frac{U^2}{L}$ and $2\boldsymbol{\Omega} \times \boldsymbol{u} \sim 2\Omega U$. Here, U is the velocity of the system while L represents the typical motion length scales. The dimensionless Rossby number

$$Ro = \frac{U}{2\Omega L} \tag{2.5}$$

can therefore be used to describe a fluid flow in a rotating frame. A small Rossby number indicates a system is strongly affected by Coriolis forces, and a large Rossby number indicates a system in which inertial forces dominate. Indeed it is commonly used in geophysical phenomena in the oceans and atmosphere, where it characterizes the importance of Coriolis accelerations arising from planetary rotation. For instance in tornadoes, where the the Coriolis force is negligible and balance is between pressure and centrifugal forces, the Rossby number is large. In low-pressure systems, centrifugal forces are negligible and balance between Coriolis and pressure forces occurs; this produce a low Rossby number. In conclusion, when the Rossby number is large the effects of planetary rotation are unimportant and can be neglected. When it is small, the effects of planetary rotation are large, and the net acceleration is comparably small.

A second adimensional number that can be defined in a rotating system is the Ekman number which determines the ratio between the frictional force per unit mass to the Coriolis acceleration.

$$Ek = \frac{\nu}{2\Omega L^2} \tag{2.6}$$

where L is the length scale (typically the vertical one) and ν is the kinematic viscosity of the fluid. Hence, for geophysical flows where dissipative terms are negligible respect to the effects of rotation, the Ekman number must satisfy $Ek << 1$.

2.2 Rotating flow

Through the action of the Coriolis force, Earth's rotation imparts a special character to large-scale motions flow such as the water masses in the atmosphere or the ones in oceans. In the absence of planetary rotation, typical magnitudes of the horizontal and vertical motion components (that can be expressed as u and w, respectively) would scale relative to one another in proportion to their respective horizontal length (L) and vertical length scales (H) of the horizontal and vertical motions:

$$\frac{u}{L} \sim \frac{w}{H} \tag{2.7}$$

Boundary layer turbulence and convection, whose timescales are much shorter then the planetary rotation do, in fact, scale in such a manner.
However, the vertical component of large-scale motions is smaller than would be expected on the basis of their aspect ratio. This is due to the rotation which suppresses part of the vertical motions, furthermore generating other typical phenomena which are described in this section.

2.2.1 Taylor Proudman theorem

The Taylor Proudman theorem is one of the most known effects produced by rotation in a generic flow. The theorem states that when ρ is constant, the velocity cannot vary along the direction of the rotation axis and the flow shows a two-dimensional behaviour. It can be rigorously proved by taking the curl of the equation of geostrophic balance

$$\nabla \times (2\boldsymbol{\Omega} \times \boldsymbol{u}) = -\frac{1}{\rho} \nabla \times (\nabla p) \tag{2.8}$$

using the vector identity

$$\nabla \times (A \times B) = A(\nabla \cdot B) - (A \cdot \nabla)B + (B \cdot \nabla)A - B(\nabla \cdot A) \tag{2.9}$$

and remembering that $\nabla \cdot \boldsymbol{u} = 0$ and $\nabla \times (\nabla p) = 0$.
Moreover, since the angular velocity is divergence-free, $\nabla \cdot \boldsymbol{\Omega} = 0$ is also needed.
The result is the Taylor-Proudman theorem that reads:

$$(\boldsymbol{\Omega} \cdot \nabla)\boldsymbol{u} = 0. \tag{2.10}$$

Hence, considering the product expansion

$$\Omega_x \frac{\partial \mathbf{u}}{\partial x} + \Omega_y \frac{\partial \mathbf{u}}{\partial y} + \Omega_z \frac{\partial \mathbf{u}}{\partial z} = 0 \tag{2.11}$$

with a rotation along the vertical axis (for wich $\Omega_x = \Omega_y = 0$ and $\Omega_z \neq 0$), the equation reduces to the solution

$$\frac{\partial \mathbf{u}}{\partial z} = 0. \tag{2.12}$$

In conclusion, all three components of the velocity vector are uniform along any line parallel to the vertical axis.

This result leads to the formation, and experimental observations, of the so called *Taylor-Proudman columns*: imaginary cilinders wich are projected above and below a solid body (e.g, obstacle placed at a certain level inside the flow as in figure 2.2) and that are parallel to the rotation axis. At levels below the top of the obstacle, the flow must of course go around it. But the Taylor-Proudman theorem assures that the flow must be the same at all levels in the fluid: so, at all heights, the flow is deflected as if the bump on the boundary extended all the way through the fluid. Taylor columns is a simplified, experimentally observed effect of what transpires in the Earth's atmosphere and oceans.

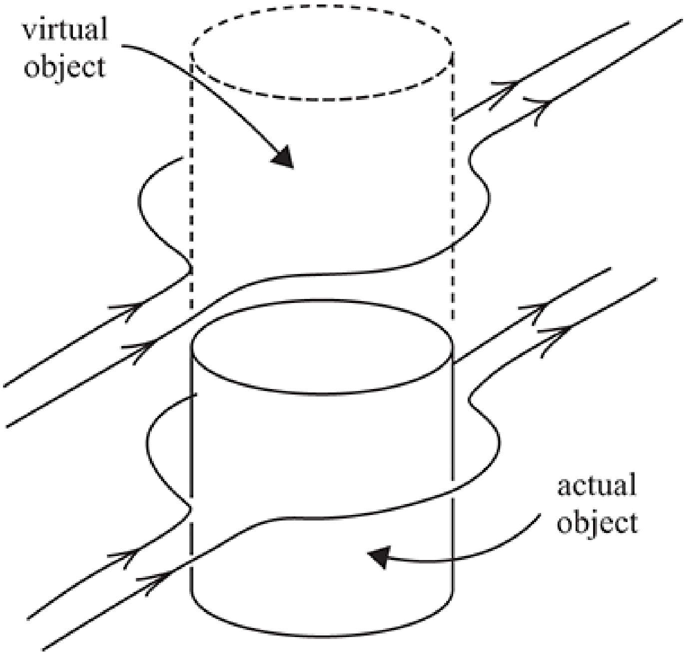

Figure 2.2: The T-P theorem demands that vertical columns of fluid act as if they were rigid and move along contours of constant fluid depth. Horizontal flow is thus deflected as if the obstacle extended through the whole depth of the fluid [17].

2.2.2 Ekman transport

Another phenomenon induced in flows which are under rotation is the Ekman transport, which has a significant impact on the biogeochemical properties of the world's ocean. This phenomenon was first noticed during an Artic expedition by the explorer Fridtjof Nansen, who recorded that icebergs were transported along a deviated direction respect to the blowing wind. Indeed, the Ekman transport occurs when ocean surface waters are influenced by a friction force acting on them. Generally, in the absence of rotation, the friction force casted by the wind stress would generate a flow motion with a velocity vector presenting the same orientation of the forcing. However, due to the influence of the Coriolis effect, the ocean water deviates with an angle from the direction of the surface wind. Because of the two different orientation of the Coriolis force respect to the motion, the direction of transport is dependent on the hemisphere.

The process is explained in figure 2.3 where the frictional movement of the surface layer of water induces a motion on the directly underneath layer, which then sets in motion the next layer under that, and so on as the water gets deeper. Clearly some energy is lost in each transition, so each successive layer of water will not move as far as the layer above it. Moreover, the Coriolis Effect deflects each layer relative to the layer above it and the resulting deviation of the successive layers therefore creates a spiraling pattern of water motion called the Ekman spiral, while the depth in which this net transport occurs is calle Ekman layer. In the northern hemisphere, Ekman transport occurs at 90° clockwise from wind direction, while in the southern hemisphere it occurs with the same angle direction anticlockwise.

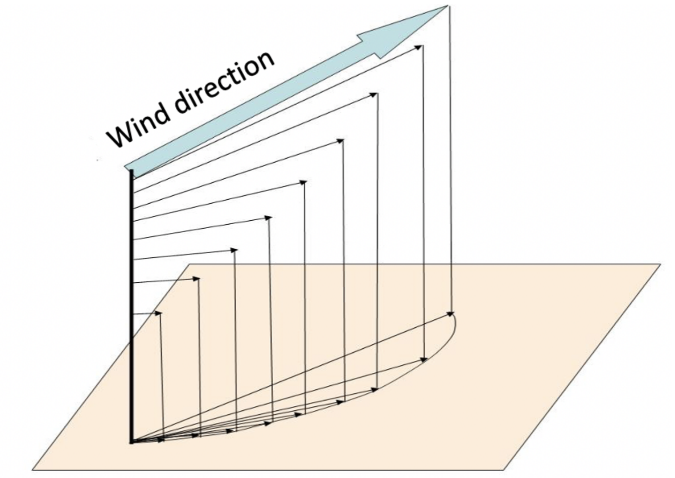

Figure 2.3: Sketch of the Ekman spiral in the Northern Hemisphere. If the magnitudes and directions of the movements of each layer are added together, the result is that the net movement in the Ekman layer is 90° to the right relative to the original wind direction.

Since the wind varies from place to place, so does the Ekman transports: it converges in some regions and diverges in others. Here vertical flows are developed at the bottom of the surface boundary layer to replace or remove

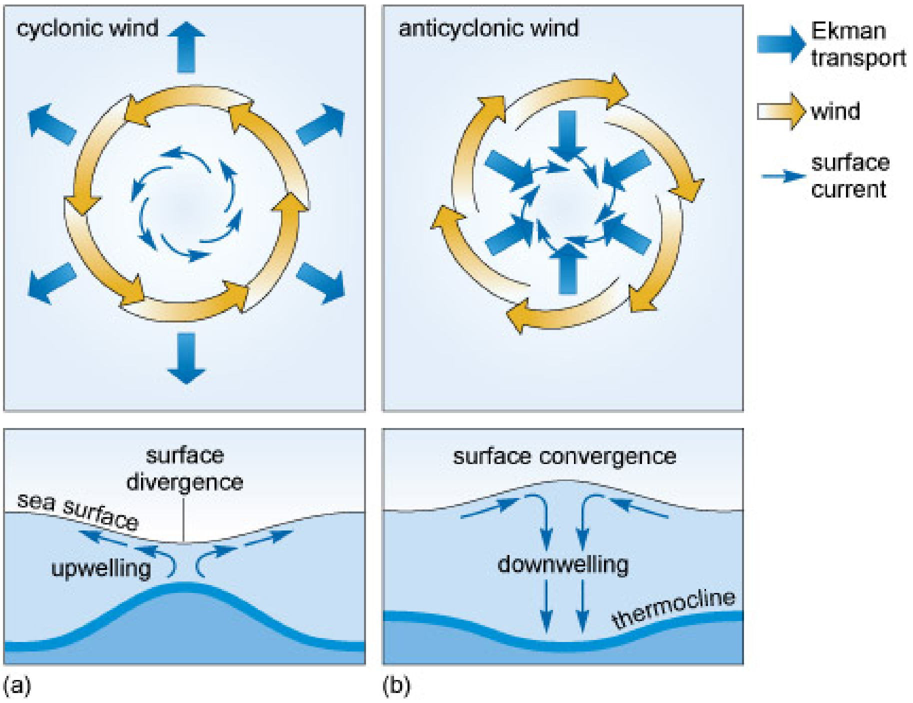

Figure 2.4: Effect of a cyclonic (a) and an anticyclonic (b) wind on the surface of the ocean in the Northern Hemisphere. In (a) there is a divergence at the surface which depresses the surface of the ocean and raises water from beneath the thermocline towards the surface, producing an Ekman suction (upwelling). In (b) the surface waters converges and pushes the sea surface upwards, depressing the thermocline with an Ekman pumping (downwelling). Figure from www.open.edu.

the converging water masses.

This process of flow generation below the surface layer through vertical movements with water displacement brings to phenomena of downwelling or upwelling (see figure 2.4). The upwelling regions are characterized by the phenomenon called *Ekman suction* where surface water diverges causing new water masses to rise from below. On the other hand the phenomenon called *Ekman pumping* represents the component of the Ekman transport where water masses are pushed downward in the downwelling process. Hence, according the mass conservation, in reference to Ekman transport, any water displaced within an area must be replenished.

This can be done by either Ekman suction or Ekman pumping depending on wind patterns, and both of them are really important for the study of the coastal upwelling and downwelling of water masses.

2.2.3 Dimensional transition in turbulent systems

Talking about turbulent systems, here the Coriolis force is responsible for an energy transfer among scales which is redistributed by rotation in its own-specific way. This focus particular attention on questions about the linear

[30, 88] or nonlinear [84] nature of the effect of rotation on turbulent flows, and a univocal answer is not yet available, since an accurate analysis of the different timescales and topological effects involved in the dynamics is required.

Above all, different effects may drive rotating flows to different regimes, depending on the value of Rossby and Reynolds number: for low Reynolds number, in the linear rotating regime, inertial waves propagation (i.e, plane waves that follow the linearized momentum equations in a rotating frame [43, 60]) is observed; while for high Reynolds and vanishing Rossby number, weak interactions are expected to occur and the wave turbulence regime [72, 5] arises.

In sufficiently energetic flows (high Re), while still considering an important rotation ($Ro < 1$), the quasi-two-dimensional turbulence [21, 32] can be observed: here the flow exhibits a dynamics very similar to what is found in a two-dimensional system, with the vertical velocity behaving as a passive scalar [33].This phenomenon has been observed in several numerical simulations where is also clear a split of the energy cascade (described in section 1.3.2). In this regime it is important to remark that the rotation needs to have an intermediate intensity, such that the Coriolis force will not be too strong to overwhelm nonlinear interactions or too weak to be neglected.

Finally, in the limit of high Reynolds and Rossby numbers, the rotation has low intensity and a three dimensional isotropic turbulent regime is recovered.

2.2.4 Breaking of symmetry

Another remarkable feature of rotating turbulent flows is the breaking of symmetry between cyclonic and anticyclonic vortices. Cyclones are defined as those vortices which spin in the same direction of the angular velocity Ω, while anticyclones are rotating in the opposite direction.

The cyclone–anticyclone asymmetry is a generic feature of rotating flows, which originates from the modification of stretching and tilting of the vorticity by the Coriolis force, suggesting a more pronounced asymmetry at $Ro \simeq O(1)$. Indeed, during the process of columnar structures formation, the distribution of elongated vortices becomes asymmetric, such that cyclones formation is favored. Moreover, as explanation of this phenomenon, it has been shown that the cyclones and anticyclones have different stability properties [3] and different probabilities to be generated at finite Rossby number [87]. In homogeneous rotating turbulence the cyclonic–anticyclonic asymmetry is reflected in the asymmetry of the pdf (probability density function) of the vertical vorticity ω_z, as shown in the work of chapter 5. The statistical characterisation of this asymmetry can be done through the observation of a nonzero value of the third-order moment of vertical vorticity $\langle \omega_z^3 \rangle$ (or the skewness $S_\omega = \langle \omega_z^3 \rangle / \langle \omega_z^2 \rangle^{3/2}$).

The predominance of cyclonic vortices has been observed both in experiments [88, 62, 66] and numerical simulations [3, 99, 84, 100, 7] of rotating turbulence and, eventhough the physical mechanisms acting on the Earth's geophysical flows are more complex than in idealized rotating turbulence, similar asymmetries have been observed also in the tropopause and in the stratosphere.

The asymmetry is expected to strongly depend on the details of the forcing and boundary conditions. The published work described in chapter 5 will focus on the study of this phenomenon depending on the vertical confinement of the flow.

Part II

Experimental tools & Numerical methods

Chapter 3

The experimental apparatus

This chapter provides the reader with a description of the experimental setup principal components (3.1) and the analysis technique (3.2) employed in one of my principal works. To get through the content, see chapter 5.

3.1 The laboratory:TurLab

The Turlab facility, built at the Physics Department of Turin University in 2004, has one of the largest rotating platforms in the world, available for scientific investigations of turbulence in presence of rotation and/or stratification.
In order to allow the study of fluid dynamics in the best conditions, it is located on the fourth underground floor, where a proper control on variables such as light, temperature, dust and external vibrations can be guaranteed. In this section a description of the main tools equipped in the laboratory is given to the reader.

3.1.1 Rotating platform

The experimental apparatus consists of a $6m$ diameter rotating platform. On the platform a rotating tank of a $5m$ diameter is installed: it can reach a maximum rotation velocity of around $20rpm$. Between the platform and the edge of the tank can be placed cameras, pc used for the acquisition, the laser and its cooling system.
Generally, it is possible to fill the tank until a water height of about 80 cm can be reached. However, due to possible high rotations, it is always important to adjust the water inside the tank, considering the formation of the paraboloid due to centrifugal force and hence, accordingly to avoid water leakage. The paraboloid formation is also important to consider in order to obtain final images with the right focus and high quality for the post-processing and analysis. On the internal side walls of the tank there are optical crystal-clear

windows which allow to observe the fluid inside the tank, in particular the region illuminated by the laser sheet.
Concerning our experiments, turbulence inside the tank was generated by periodic oscillations of a comb (shown in Figure 3.3), formed by a series of spaced paddles, that moves back e forward along a motorized linear guide placed in the radial direction. The comb motion can be controlled by an external software directly connected to the linear guide, being able to smoothly reduce its velocity before inverting the direction of motion avoiding wave perturbations on the surface.
The spacing between paddles can be modified in order to change the forcing scale energy injection and hence also the flow Reynolds number. In this way, vortices with a length scale of the order of the spacing paddles distance are generated and a study of the flow turbulent characteristics can be performed.

Figure 3.1: Image of the Turin rotating platform.

3.1.2 Laser

The experiment's lighting system is composed by a Quantum Opus solid state diode green laser with a maximum output power of $6W$, a direct transmission without optic fiber and a wavelength of $532nm$. Through semicilindrical concave lenses with different focal point, the laser beam can be expanded in a laser sheet which can be oriented both horizontally or vertically according to the experiment. Indeed the presence of a channel arranged in a radial direction and covered by a rectangular optical crystal plate that completes the bottom of the tank, allows an illumination from below and therefore implies an optimal study of the boundary layer of the fluid in contact with the bottom floor. The orientation of the laser sheet can however be improved thanks to the use of a system of adjustable mirrors. Moreover, in order to cover a large part of the apparatus, the laser light can be spread by a maxima divergence lens.

In our experiments, shown in Figure 3.3, the Opus laser was positioned laterally, opposite to the forcing comb, producing an horizontal sheet, parallel to the tank floor and $6cm$ above it. For any type of experiment it is necessary to find, through different pre-tests, the best setup that leads to the best configuration in terms of image sharpness and particle detectiion.

3.1.3 Seeding particles

The seeding of a flow with little particles is a fundamental part of the experimental setup, in order to track the particles motion and then to be able to reconstruct the flow velocity field. Indeed, considering the Particle Image Velocimetry (PIV) technique, described in section 3.2, the light diffusion properties of these particles are crucial characteristics for the quality of this technique based on tracers. Moreover, to obtain good measures, an homogeneous seeding of the flow is necessary.

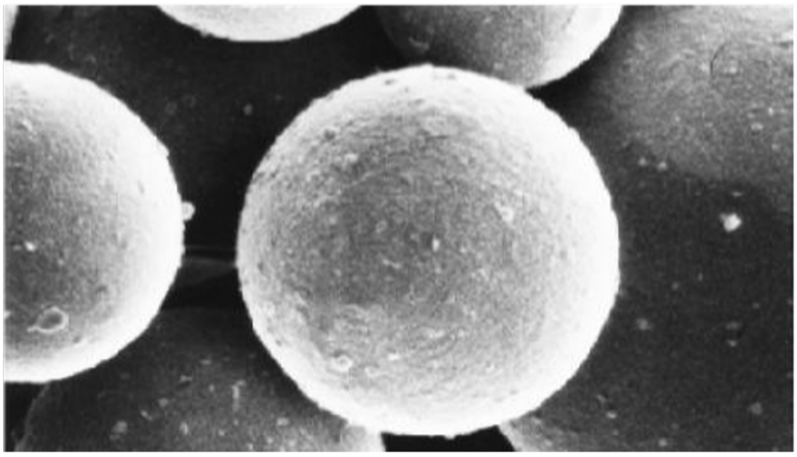

Figure 3.2: Zoomed imaged of particle tracers.

For this reason, a large quantity of particles need to be injected. Moreover, the seeding particles material influences the character of the image field: particles used are made of polyamide and present a mean diameter of some tens of μm. Ideally they ought to be spherical, homogeneous and to have high diffusivity to minimize the input light energy. Actually, particles tracers are not perfect spheres, they have a radius distribution and they don't maximize diffusivity (Example shown in Figure 3.2). Usually, before being incorporated into the flow inside the tank, they are treated with a wetting agent that increased their suspension and hence a homogeneous distribution can be achieved. Moreover, they need to be meshed in the flow some hours before the measures acquisition in order to get the best homogeneity inside the flow and, at the same time, to avoid the particle sedimentation.

3.1.4 Digitals cameras

Several cameras, with high spatial resolution and sensibility, are equipped in the laboratory in order to acquire images for the PIV analysis. Each camera is able to acquire in stand alone or in synchronized mode, with a selection of both the grey scale (in terms of pixel depth $8-10$ bits) and the frame rate ($1-60$ Hz).

The frame rate needs to be properly chosen depending on the flow velocity: nor too high, in order to allow a minimum displacement of tracer particles, neither too low, to avoid a excessive displacement having the risk of loosing groups of particles between a couple of consecutive frames. Generally, to optimize the analysis, a frame rate which allows to acquire $5-10$ pixel particle displacement can be setted.

It is furthermore important to choose the right iris opening and image focus: indeed, the aim on having brighter frames to analyse sometimes it results in too much blurry images. Hence, usually it is better to privilege the image focus and possibly change the brightness at a later time via software.

When a particle is enlightened by the laser sheet, Mie scattering [31] is produced and the related intensity light power particle emitted is:

$$P_p = \frac{\pi r^2 P_l}{dS} \tag{3.1}$$

where r is the particle radius, d the laser sheet thickness, S is the laser sheet extension and P_p is the laser power. The real low P_p value justifies the need to use very sensitive cameras.

Regardless of the cameras characteristics, the water needs to be as clean as possible to correctly identify particles inside the flow, which is why small amounts of chlorine can be sometime added to the liquid. Indeed, especially for those experiments that last several days, the presence of environmental bacteria could really create a major problem, causing particles agglomeration and variation in their dimensions. Nevertheless, also the pre-tests are important in order to select the best recording flow region, according to the images illumination, the presence/absence of vortices following the mean rotating flow. For istance, in some tests we observed the presence of macular

areas without particles tracer in the water, most likely due to the paddles-generated whirlwinds which, being stabilized by rotation, could expel the tracer with the result of a non-homogeneous seeding.
Finally, the acquisition can be performed by two pc that collect data through a camera link connection. These systems can control cameras, their parameters, the synchronization and the acquisition settings. Each pc is able to acquire directly onto hard drives ensuring very long acquisitions on many consecutive experiments before exporting data.
Concerning our experiments, for each analized flow configuration, a few dozen of short acquisitions have been made in order to have a solid statistics. The camera was placed above the comb passage, recording a portion of the flow perturbed by the paddles (see Figure 3.3). The huge amount of acquired frames can be hence analysed and post-processed with data analysis technique described hereafter.

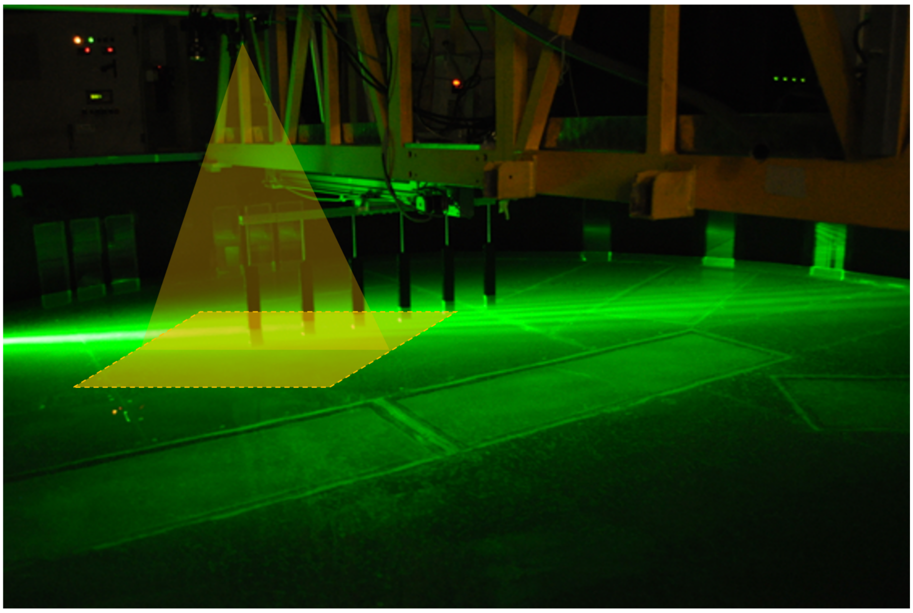

Figure 3.3: Scheme, in orange, of the experimental recorded area. In the image, also the comb and the laser are shown.

3.2 Data analysis: Particle Image Velocimetry technique

Particle Image Velocimetry (PIV) is an optical method adopted in flow analysis [79]. This technique is appropriate to describe fluid evolution in a specific area or volume. PIV is used to match pattern in two time-consecutive images of the flow. The field's displacement, proportional to velocity, is obtained from the direct cross-correlation between a couple of pictures. As previously described, the fluid is seeded with a lot of particles, with a density similar to the fluid's one, which accurately follow the fluid motion. At the same time, particles must be very small because the goal is to minimise inertia and interaction with the fluid and to avoid sedimentation effects. The field of view is usually enlightened with a laser sheet and the velocity field projection is obtained on this plane of measurement. In particular, the particles reflect light (Mie scattering) which is captured by a camera.
The following section provides an overview of such technique and briefly describes the software used for the experimental analysis.

3.2.1 Principles of PIV

The experimental set-up for a PIV experiment usually consists of different subsystems. Studying a fluid, the first thing to do is to add solid tracers. The illuminated particles scatter the light that is recorded in a sequence of frames. The displacement of the particles over the time has to be determined through evaluation of the recordings. To be able to handle the great amount of images and retrieve physical informations by camera, a sophisticated post-processing is required.
For evaluation, the recordings are divided in small sub-area called "interrogation windows". The local displacement vector is determined for each interrogation area by a cross-correlation statistical method in which a pair of interrogation areas are evaluated.
A common set-up for PIV can be seen in figure 3.4.
The assumption that is made is that each particle in the interrogation area has moved homogeneously between two different recorded frames. The process of interrogation is then repeated for each interrogation areas of the PIV recordings. A digital camera is usually used to record the different images, after having carefully chosen the acquisition rates, depending on the actual problem that is going to be studied.
Some characteristic of the PIV technique are here listed:

- **Whole field technique and indirect velocity measurement**
  PIV is a technique that allows to record images of large part of flow

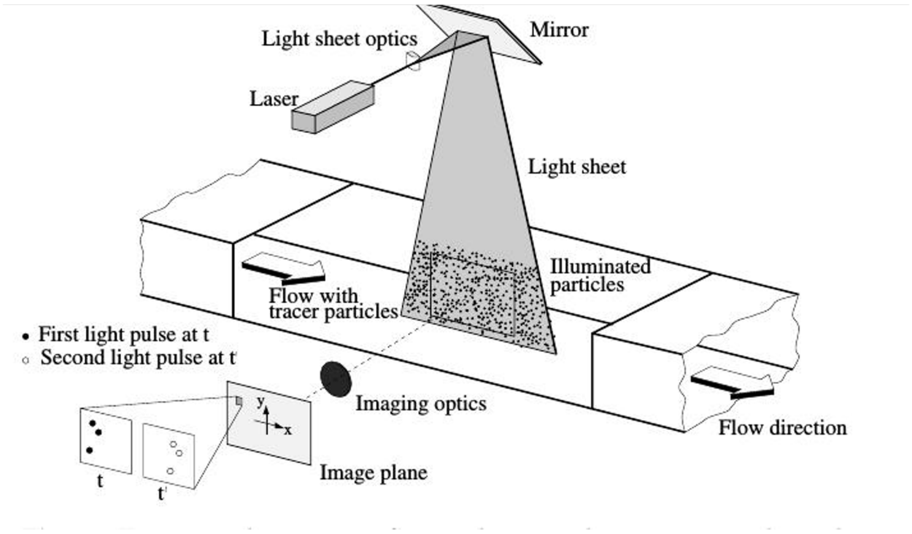

Figure 3.4: Scheme of an experimental set-up for PIV analysis in a wind tunnel [79].

fields, depending on the experimental set-up, in a variety of applications in gas and liquid media. Moreover, PIV measures the velocity of a fluid element by measurement of the velocity of suitable tracer particles within the flow.

- **Non intrusive velocity measurement**
  In contrast of measurement techniques that employ probes, the PIV, being an optical technique, works in a non intrusive way that allow application of this technique in high speed flows where the flow may be disturbed by the presence of the probes.

- **Importance of the particles distribution in the flow**
  Qualitatively three different types of particle density can be distinguished. In the case of low density the images corresponding to the same particle originating from different illuminations can be identified. For this reason, low particle density also requires tracking methods for evaluation (the so called "Particle Tracking Velocimetry" or PTV).
  Considering medium particle density, the images of individual particles can be detected as well and is required to apply the standard statistical PIV evaluation techniques. Remember that PTV adopts a Lagrangian description, while PIV is suitable for Eulerian fields.
  Finally, in a case of high particle density, it is not even possible to detect individual particles as they overlap in most cases, forming speckles. This situation is called "Laser Speckle Velocimetry".

- **Spatial resolution**
  The size of the interrogation areas during evaluation must be small

enough for the velocity gradients not to have significant influence on the results. Furthermore, it determines the number of independent velocity vectors and therefore the maximum spatial resolution of the velocity map which can be obtained at a given spatial resolution of the recording camera.

- **Temporal resolution**
  Most PIV systems allow to record with high spatial resolution, but at relative low frame rates. However, the recent development of high-speed lasers and cameras allows time resolved measurements of most liquid and low-speed aerodynamic flows.

In order to process a flow velocity vector field, a direct cross-correlation, or covariance, method between image pairs (divided in small boxes) is used in PIV technique. The final displacement vector is obtained as the vector that determines the maximum of cross-correlation for each box.
The basic algorithm starts with the selection of the elementary box, called *pattern box*, in which the correlations will be calculated along both directions x and y. The minimum value for the box is the one that include at least 5 particles and the box size needs to be properly choose according to the characteristics of the flow, but it is preferable not to choose a too large box that is too large since the velocity is obtained as an avarage in the pattern box, a box that is too large leads to a lower spatial resolution. Moreover, being the supposed pure translation motion valid only in a local limit, the larger the box, the more the deformation effects increase, with a lower correlation quality.
The second step is to define a *search box* which must contain the expected optimum pattern position in the second frame. Here an excessive size leads to an increased computation cost and appearance of false vectors, due to spurious correlation maxima, while a smaller search box can produce false vectors due to the missing of the real correlation maximum.
Then the algorithm computes the cross-correlation working with the images pixel intensities: here the velocity vector is obtained as the displacement that maximizes the correlation. However, the occasional occurence of secondary maxima of the correlation is one of the major problems of the analysis. Usually those multiple peaks are caused by a low particle density or bad illumination. To limit those false velocity vectors, it is possible to reduce the search box, using a priori knowledge of the velocity field; alternatively, if the correlation of false vectors remains high, a threshold on the standard deviation of the velocity distribution can be introduced in order to flag those flase vectors which deviate too much in terms of module or component directions. These kind of filtering allows to remove false vectors and eventually interpolate us-

ing the neighbour vector values, in order to obtain good ones.

Finally, since the images are in pixel units, a conversion into physical coordinates needs to be considered; so, in every PIV analysis it is necessary to introduce a step of calibration, inserting a calibration target board, with known pattern and dimensions.

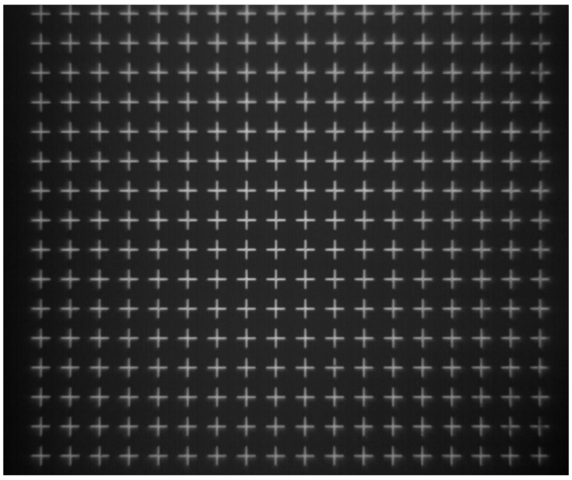

Figure 3.5: Example of a target board used to the transformation from pixel to physical units.

3.2.2 OpenPIV software

In this short paragraph I present the analysis software that I used on the experimental PIV data and that I helped to implement by improving some scripts concerning the organization and transposition of the computed velocity field matrices.

The OpenPIV software is an open-source package for analysing images of particles flow and producing velocity fields. In addition the software allows the use of additional tools for post-processing the PIV results. Here I present the principal software features, while further details can be found in [6]. The software architecture is built both in Python and Matlab to provide the users with an intuitive and fast post-processing tools.

First of all a Graphical User Interface comprises several subroutines that allow to import PIV images, pre-process them, analyse using cross-correlation algorithm, filter and interpolate the flow field, and export the velocity vector maps as ASCII files. After the loading of raw images, the GUI allows the user to choose the main PIV parameters such as time interval between frames (Δt), scale (i.e., pixels/meter), image pre-processing function (e.g., contrast enhancement).

Furthermore, also a precise region-of-interest (ROI) can be selected inside the image for the PIV analysis, together with the interrogation window size and the pixels spacing/overlap between each window.

The cross-correlation algorithm is applied to sub-image square or rectangular interrogation windows. OpenPIV utilizes an FFT-based cross-correlation algorithm to process pairs of frames, therefore the interrogation window sizes are typically of $2^n \times 2^n$. The windows spacing/overlap value controls the spatial resolution of the x, y grid at which horizontal and vertical velocity components (u, v) can be estimated. Larger interrogation window size reduces resolution but are less affected by the background noise.

The kind of threshold vector filtering can be chosen a priori between two options: the outlier velocity threshold or the signal-to-noise ratio (S/N) type threshold. The latter is in turn divided in two implementations: one compares the peak in the correlation plane with the mean of the correlation field, while the other estimates the ratio between the highest peak with the second highest one. There are no default thresholds values and a try-out has to be perform in order to find out the best value.

OpenPIV also applies global and local filtering. The global filter removes vectors with length that are larger than the mean of the flow field plus N times its standard deviation; defined in a statistical sense as global outliers. The N value is selected through the GUI global filter parameter.

Moreover, local filter is performed on small neighbourhoods of vectors using a 3×3 kernel, removing vectors which length differs more than 3 times standard deviation respect to the local mean of the 8 nearest neighbour vectors. Typically it is desired to reach about 5% of erroneous vectors: the missing ones are later filled using iterative interpolation, based on the valid neighbourhood vector values. This is also a reason for the Matlab version to generate three lists of ASCII files: raw data, filtered data and finally interpolated data (see an example in Figure 3.6). After the file creation, a second GUI called Spatial and Temporal Analysis toolbox, allows to load the created vector velocity maps into a 3D flow velocity array where the third dimension is the frame number of the flow field in the ensemble. Thanks to the toolbox, various flow characteristics are calculated.

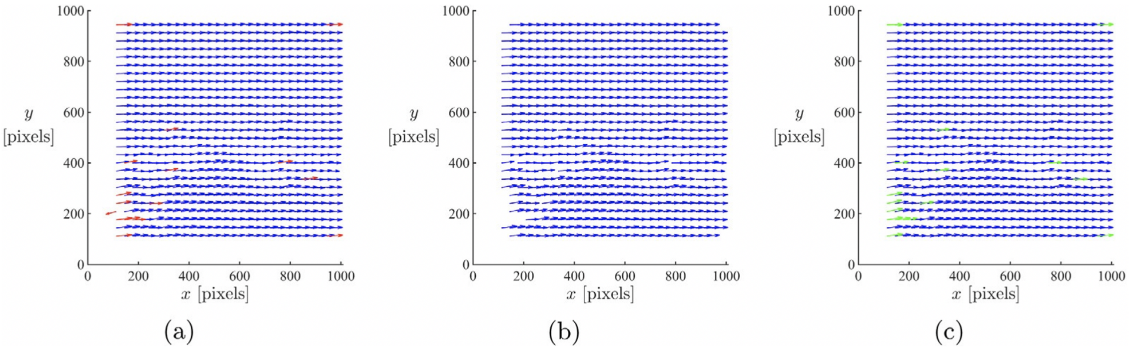

Figure 3.6: Velocity vector maps from OpenPIV analysis files. Panel (a) represent raw data with red outlier velocity vectors, in (b) filtered data, and in panel (c) the final velocity vector maps where the interpolated vectors are colored in green.[6]

Data can be automatically decomposed into mean and turbulent fluctuations and provides both qualitative and quantitative visualization tools of a large variety of flow properties including the spatial velocity derivatives, vorticity, strain rate and turbulent parameters like turbulent kinetic energy, production, dissipation and enstrophy.

Qualitatively, the toolbox offers several options to show the calculated flow properties in the form of colored contour maps, contour lines and vector representation. Quantitatively, it offers the user to plot the properties in a 2D format, by selecting regions of interests, or cross-sections. The flow characteristics computed in this toolbox are then exported as binary Matlab file.

Chapter 4

Numerical method

This chapter briefly describes the numerical methods adopted in all simulations presented in part III where my works are proposed. Moreover, in section 4.2 an overview on the modelling implementation and code optimization carried out during my PhD is given.
The majority of the code simulation and implementation has been done on HPC CINECA clusters: in particular on MARCONI and GALILEO supercomputers (see https://www.hpc.cineca.it/content/hardware for details of the hardware characteristics).

4.1 Pseudospectral method

This section gives a brief explanation on the use of the pseudo-spectral code used to integrate the rotating Navier-Stokes equation in an unbounded space, with periodic boundary conditions.
The integration of the following set of PDE is needed:

$$\begin{cases} \partial_t \boldsymbol{u} + \boldsymbol{u} \cdot \nabla \boldsymbol{u} = -\nabla p + \nu \nabla^2 \boldsymbol{u} - 2\boldsymbol{\Omega} \times \boldsymbol{u} + \boldsymbol{f} \\ \nabla \cdot \boldsymbol{u} = 0 \end{cases} \tag{4.1}$$

where $\boldsymbol{u} = (u, v, w)$ is the velocity vector, p is the pressure, ν is the kinematic viscosity, $\boldsymbol{\Omega} = (\Omega_x, \Omega_y, \Omega_z)$ is the angular velocity vector and $\boldsymbol{f}$ represents an external forcing. The solution of the problem requires to specify both the initial and boundary conditions. Concerning boundary conditions, we assume periodic boundary conditions, i.e. $u_i(x) = u_i(x + L)$. From a physical point of view, this allows to look for universal behavior considering an homogeneous flow far from boundaries. From a numerical point of view, this is convenient because it simplifies the code making it efficient. Assuming periodic boundary conditions fixes a uniform discretization and the Fourier representation of the velocity field.

4.1.1 Fourier transforms and FFT

The definition of Fourier transform can be done considering, for simplicity, a scalar field u discretized on N points $x_i = i\delta x$ with $\delta x = L/N$ and $i = 0, \ldots, N-1$. Hence the direct (forward) and inverse (backward) Fourier transforms are

$$\begin{aligned} u_n &= \sum_{k=0}^{N-1} \hat{u}_k e^{i\frac{2\pi}{N}nk} \\ \hat{u}_k &= \frac{1}{N} \sum_{n=0}^{N-1} u_n e^{-i\frac{2\pi}{N}nk} \end{aligned} \tag{4.2}$$

where $u_n = u(x_n)$ and $\hat{u}_k$ is the Fourier component at fixed wavenumber k. Because of the discretization one have $\hat{u}_{N-k} = \hat{u}_{-k}$ with the Nyquist frequency (i.e. the higher frequency representable) being $k = N/2$ [22].
With the normalization factors in (4.2), the Parseval identity is written as

$$\sum_{n=0}^{N-1} |u_n|^2 = N \sum_{k=0}^{N-1} |\hat{u}_k|^2 \tag{4.3}$$

and thus, defining the average as $\langle u \rangle \equiv \frac{1}{L} \int_0^L u(x)dx$, the kinetic energy can be written as

$$E \equiv \frac{1}{2}\langle u^2 \rangle = \frac{1}{2} \sum_{k=0}^{N-1} |\hat{u}_k|^2 \tag{4.4}$$

Moreover, if the considered field is real $u \in \mathbb{R}$, from (4.2), the reality conditions is $\hat{u}_{-k} = \hat{u}_k^*$ and thus the Fourier representation requires only the positive wavenumbers. In the three-dimensional case the Fourier transform $\hat{u}(k_x, k_y, k_z)$ involves in general N^3 complex components. If $u \in \mathbb{R}$ one can still reduces the components by a factor 2. Indeed, for simplicity, most of the multidimensional Fourier transforms, consider the following wavenumbers

$$k_x \in [0, \ldots, \frac{N}{2}] \tag{4.5}$$

$$k_y, k_z \in [-\frac{N}{2} + 1, \ldots, 0, \ldots, \frac{N}{2}]. \tag{4.6}$$

Eventhough this representation uses more memory than what is necessary (N^3 real numbers), the resulting code is much simpler, as the codification of the Fourier transform in N^3 real numbers would be much more complex than in the one-dimensional case.
Considering the one-dimensional transform in (4.2), the evaluation of the Fourier transform $\hat{u}_k$ for all the values of k requires N^2 operations. This is numerically very expensive, expecially when N is large or in more dimensions. The idea of Fast Fourier Transform (FFT) is to drastically reduce the number

of these operations. These method, originally introducted by Gauss [42], becomes popular in the sixties, after the work of Cooley & Tuket [29]. Despite being used to solve partial differential equations, fluid flows, density functional theory, etc., the FFT remains one of the most significant algorithms which crosses various disciplines in science and society such as signal processing, image analysis or radio astronomy.

The basic idea is to write the Fourier series in (4.2) as a sum of two terms, one corresponding to odds n and the other to even n:

$$\begin{aligned}\hat{u}_k = & \sum_{n=0}^{N/2-1} e^{i\frac{2\pi}{N}k(2n)} u_{2n} + \sum_{n=0}^{N/2-1} e^{i\frac{2\pi}{N}k(2n+1)} u_{2n+1} = \\ = & \sum_{n=0}^{N/2-1} e^{i\frac{2\pi}{\frac{N}{2}}kn} u_{2n} + e^{i\frac{2\pi}{N}k} \sum_{n=0}^{N/2-1} e^{i\frac{2\pi}{\frac{N}{2}}kn} u_{2n+1} = \\ = & \hat{u}_k^{(\mathrm{e})} + e^{i\frac{2\pi}{N}k} \hat{u}_k^{(\mathrm{o})}\end{aligned} \tag{4.7}$$

This result means that Fourier transform can be obtained by computing two series with half the length and with all even indices, respectively all odd indices, as new data vectors.

In this way one can reduce the original Fourier transform on N points to two Fourier transforms on $N/2$ points. Since the number of operations is proportional to the number of points square, in the latter case one need to perform only $O(N^2/2)$ operations and thus a gain of a factor two is achieved. The idea of FFT is then to repeat this splitting procedure recursively. If the number of points is a power of two, $N = 2^m$, after repeating m times the procedure one obtains that the computation of the FFT on N points involves $O(N \log N)$ operations.

4.1.2 Physical and Fourier space operations

The idea of using Fourier representation on a periodic grid is that derivatives and integrals become simple multiplicative operations. From the definitions (4.2), the exact Fourier representation of $\partial_x u(x)$ is simply $(2\pi/L)ik\hat{u}_k$ and, for simplicity, one can consider the period $L = 2\pi$. The enormous advantage of Fourier representation became evident for more complex operations such as, taking into account the Navier-Stokes equations 4.1, the inversion of a Laplacian:

$$\widehat{(\nabla^{-2}u)}_k = -\hat{u}_k/k^2 \tag{4.8}$$

The drawback of Fourier representation are the nonlinear terms that become convolutions involving $O(N^2)$ operations. For example

$$u\partial_x u \xmapsto{F} \sum_m \hat{u}(k-m)im\hat{u}(m) \tag{4.9}$$

For this reason, the idea of the pseudo-spectral method is to perform linear operations, such as derivatives, in Fourier space and to calculate the products of nonlinear terms in physical space. A scheme for computing the term (4.9) is

$$\begin{tikzcd}
\hat{u}(k) \arrow[r, mapsto, "FFT^{-1}"] & u(x) \arrow[dr] & & \\
& & u\partial_x u \arrow[r, mapsto, "FFT"] & \widehat{u\partial_x u} \\
ik\hat{u}(k) \arrow[r, mapsto, "FFT^{-1}"] & \partial_x u(x) \arrow[ur] & &
\end{tikzcd} \tag{4.10}$$

and thus requires 3 Fourier transforms. Indeed, this is the usual numerical method to compute convolutions, by means of efficient FFT, since this method remains much faster than the direct evaluation of the convolution.
As an example, our $3D$ code integrates the Navier-Stokes equations for the vorticity field 1.9 here rewritten as:

$$\partial_t \boldsymbol{\omega} - \nabla \times (\boldsymbol{u} \times \boldsymbol{\omega}) = \nu \Delta \boldsymbol{\omega} \tag{4.11}$$

Introducing now a vector potential $\boldsymbol{b}$ defined as $\boldsymbol{u} = \nabla \times \boldsymbol{b}$ one can write $\boldsymbol{\omega} = \nabla(\nabla \cdot \boldsymbol{b}) - \Delta \boldsymbol{b}$.
Moreover, since the vector potential is divergence-free, onee can take $\nabla \cdot \boldsymbol{b} = 0$ and hence $\boldsymbol{\omega} = -\Delta \boldsymbol{b}$. The equation of motion written for $\boldsymbol{b}$ are

$$\partial_t \boldsymbol{b} + \Delta^{-1}\left[\nabla \times (\boldsymbol{u} \times \boldsymbol{\omega})\right] = \nu \Delta \boldsymbol{b} \tag{4.12}$$

Here the numerical scheme integrates (4.12) by computing $\boldsymbol{u}$ and $\boldsymbol{\omega}$ from $\boldsymbol{b}$ in Fourier space, the product $\boldsymbol{u} \times \boldsymbol{\omega}$ in physical space and then derivatives back in Fourier space.
To conclude, since in a pseudospectral code approximately the $70\% - 80\%$ of the total time is spent on the forward and inverse Fourier transforms, a good thing is to find the best FFT routine which better optimize the code speed without loosing in precision.

4.2 Parallel computing library

FFT-based spectral methods are the core of all Direct Numerical Simulation (DNS) codes used in fundamental studies of turbulence and transitional flows and, nowadays, these simulations are pushing the limits of high-performance supercomputers with huge computational domains and a tremendous amount of variables. Considering such applications, it is important to ensure the best possible algorithms in terms of serial/parallel FFT which takes the majority of the time computation being therefore the determining factor in the code speedness.

Usually an FFT on multidimensional data can be performed as a sequence of one-dimensional transforms along each dimension, using a transpose approach. Considering for example a multidimensional array of shape $N_x \times N_y \times N_z$, one can firstly perform a $N_x \times N_y$ serial transform of length N_z along the thirs axis, followed by a $N_x \times N_z$ transform of length N_y along the second axis and then finally compute the $N_y \times N_z$ transform of length N_x along the first axis.

This can cause problems when the computational domain is very large and can't be fitted in the memory of a single core unit. In these case the domain need to be distributed among several units where only a small part of the multidimensional array is available on each processor. Hence, the computation of a multidimensional FFT need to be supported by global redistribution operations and decomposition algorithms, by ensuring that array data for a serial one-dimensional transform is locally available when needed. The main used parallel implementation are based on transpose algorithms [35], where the array is reorganized by a single step of global transposition so that the dimension to be transformed becomes local, and then serial 1D FFT can be applied.

During my PhD i contributed to optimize our numerical parallel codes, where a simultaneous use of multiple compute resources is exploited to numerically integrate the physics equations. My contribution had been to modify the actual matrix fields organization (see 4.2.1) and to test/implement a new FFT field decomposition (see 4.2.2) according to the opensource library P3DFTT [75] with the aim of optimize computing performance. Hereafter the two principal decomposition method are described.

4.2.1 Slab decomposition

The first main used method refers to the so called *slab decomposition* where a global array data is divided in one or more 2D planes, each one assigned to a core processor task. Since, using slab decomposition, only one axis of a multidimensional array is distributed between core processors and the grid is divided along a single dimension, the method involves a 1D domain decomposition (see Fig. 4.1(a)). This method implies a very high efficiency on a limited number of cores because, after a FFT along the two local directions, it only requires one global array transpose and the computation of the FFT along the third axis direction, minimizing the communication between cpu processors.

However, considering a 3D-array domain of dimension N_x, N_y and N_z, this approach works well only as long as the number of processors does not exceed the linear grid size N, with $N = min(N_x, N_y, N_z)$. This could result in sudden loss of scalability due to load imbalance, as some tasks could be without work. This is a severe limitation since nowadays petascale supercomputer platforms offer several hundreds of thousands of cores for calculation.

To overcome this issue, and obtain a global code gain in speed/efficiency, a different kind of decomposition can be implemented.

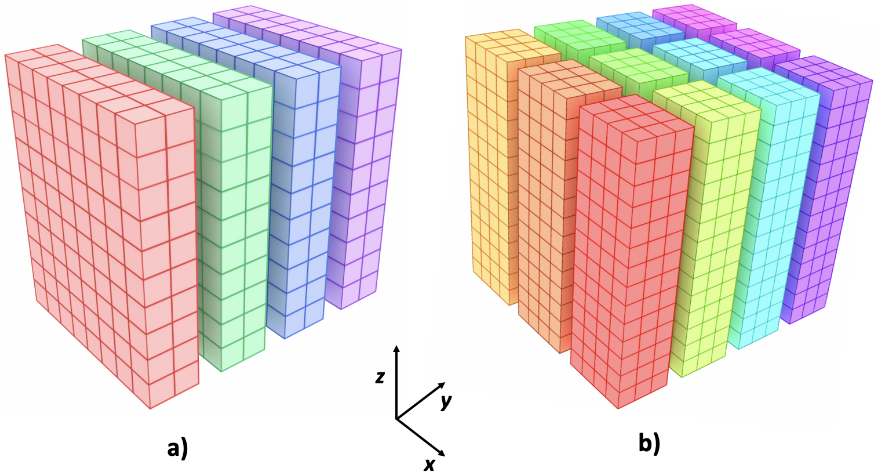

Figure 4.1: Left panel a) represents a slab (1D) decomposition of a global array that is distributed along y among 4 CPUs, with x, z dimensions locally contained in the same processor. Right panel b) shows a pencil (2D) decomposition of a global array divided in pencils aligned in the local z-direction and distributed among 3 CPUs in the x-direction and 4 CPUs in the y-direction, with a total of 12 tasks. Part of the figure from [24].

4.2.2 Pencil decomposition

The next logical step of parallel computing is reached with the so called *pencil decomposition*, where two axes of a multidimensional array are here distributed (2D decomposition).

With a huge global array distribution, pencil decomposition requires more information exchange between cores in terms of FFT computation, resulting in a higher difficulty in code implementation and in a lower efficiency respect to the slab method which has less communication between each processor. Despite paying an higher cost in terms of MPI communications, the algorithm ensures higher scalability. Indeed, it possess a better scaling respect to the 1D decomposition since the maximum number of processors can be as large as N^2 (equal to the maximum number of pencils) in a N^3 domain. For this reason, the 2D pencil decomposition becomes a valid choice for large-scale simulations using hundreds of thousands of processors.

Figure 4.1(b) shows an example of a global array domain where, instead of slabs, each processor/task is responsible for a rectangular column (pencil) of the data array. Here the domain is organized in pencil which possess, along one axes (here the z), all grid points. In this way, corresponding to the idea of the transpose approach previously described, the one-dimensional FFT always proceeds locally along the pencils oriented direction. Considering the other two directions the domain is divided and each subgroup of grid points is distributed among processors. Hence, in order to locally compute the 1D FFT, a transposition of the global array it is first necessary. For a global 3D Fourier transform, having a 2D pencil decomposition, are thus needed three FFT computation and two transpose stages.

Thus, using the library P3DFFT (several details can be found in [75]), I implemented a pencil decomposition on our code and tested it, verifying final FFT results to be equal to the ones of our previous slab decomposition code. Moreover, following [75] I arranged in a two-dimensional virtual grid with dimensions $M_1 \times M_2$ (rows × columns) which controls the dimensions of each pencil being respectively $(N_x, N_y/M_1, N_z/M_2)$. Clearly, as long as the product $M_1 \times M_2 = P$, with P the total number of tasks/processors, there is some freedom in choosing the grid dimensions. Tests need to be conducted also to find an optimal choice of M_1, M_2 since code performance depends also on the supercomputer platform organization.

Intuitively, the optimal performance might have seemed the one which maximize the number of pencils in both directions, producing a processor dimensions distribution of $M_1 \times M_2$ square grid. However, testing the same global array domain with different pencil decompositions I verified that, for our platform (HPC CINECA center), the maximum performance is achieved when the value of M_1 remains close to the number of cores contained inside a single node.

The observed result could have the following explanation: with such a value of M_1, the first row-transpose can always occur all within a single node, avoiding communication among cores of different nodes and saving time in terms of algorithm computation.

In conclusion, the 1D slab decomposition is faster on a limited number of computing cores and possesses a lower scaling respect to the 2D pencil decomposition. Even if the latter requires more communication between cores, the continuous rise in technology and the availability of massively parallel supercomputers make it the better solution in a perspective of code optimization and speed. However, this kind of decomposition need to be tested according to the kind of the available platform in order to optimize the gain during matrix transposition and cores communication.

Part III

Works & Results

Chapter 5

Cyclone–anticyclone asymmetry in rotating thin fluid layers

This chapter has been published:
G. Boffetta, F. Toselli, M. Manfrin, S. Musacchio, Cyclone–anticyclone asymmetry in rotating thin fluid layers, *Journal of Turbulence*, 1 (2020).
https://doi.org/10.1080/14685248.2020.1855352

The following study reports a series of laboratory experiments and numerical simulations of freely-decaying rotating turbulent flows confined in domains with variable height. We show that the vertical confinement has important effects on the formation of large-scale columnar vortices, the hallmark of rotating turbulence, and in particular delays the development of the cyclone-anticyclone asymmetry. We compare the experimental and numerical results face-to-face, showing the robustness of the obtained results.

5.1 Introduction

A distinctive feature of turbulent rotating flows is the spontaneous formation of coherent columnar vortices aligned in the direction of the rotation axis. The presence of these long-living, quasi-two-dimensional structures has been observed both in experiments [49, 62, 88, 66] and in numerical simulations [3, 99, 84, 100, 7]. The mechanisms which cause their formation, in particular concerning the interplay between inertial waves and nonlinear triadic interactions, have been subject of intense studies (for a recent review see, e.g., Ref. [41]).
Remarkably, most of these vortices are always co-rotating with the flow, i.e., they are cyclones. The predominance of cyclones over anticyclones have been reported and investigated in a large number of numerical and experimental studies, both in freely decaying turbulence [3, 16, 96, 68, 67, 78, 66] and

forced turbulence [40, 83, 37, 7]. It has been observed also in atmospheric measurements [27, 47] and in rotating thermal convection [25, 46, 97]. The symmetry-breaking is typically quantified in terms of the skewness $S_\omega = \langle\omega_z^3\rangle/\langle\omega_z^2\rangle^{3/2}$ of the vorticity ω_z in the direction of the rotation vector $\boldsymbol{\Omega} = \Omega \boldsymbol{e}_z$. Other indicators have been recently introduced, including third-order two-point velocity correlation functions [38], the skewness of the azimuthal velocity increments [32] and the alignment statistics between vorticity and the rotation vector [71].

Two types of arguments have been proposed to explain this phenomenon. First, cyclones have a larger vortex stretching $(2\Omega+\omega_z)\partial u_z/\partial z$ in a rotating flow with given vertical strain $\partial u_z/\partial z$. As a consequence, an isotropic turbulent flow suddenly put into rotation develops a positive skewness S_ω [39]. The second type of explanations is based on the Rayleigh stability criterion, which shows that anticyclonic vortices are more subject to centrifugal instabilities [3, 87].

Previous studies have shown that the asymmetry is strongly dependent on the Rossby number Ro. In particular, it is maximum for Ro of order unity [16]. In decaying rotating flows the skewness S_ω grows in time as Ro decreases from an initial large value [68, 66, 71]. A recovery of the symmetry has been observed in the late stage of the decay, when $Ro \ll 1$ [68, 66]. Much less is known about the dependence of the asymmetry on the the height H of the fluid in the direction of the rotation axis, because this phenomenon is typically studied in domains with aspect ratio of order unity. Recently, it has been shown that the confinement of the flow in a thin layer causes a reduction of the asymmetry in forced rotating turbulence [32].

The aim of this study is to investigate, by means of experiments and numerical simulations of freely decaying rotating turbulence how the cyclone-anticyclone asymmetry is affected by the thickness of the flow. This issue is closely connected to the puzzling relation between rotation and two-dimensionalization in turbulence. On the one hand, it is well known that rotation induces a two-dimensionalization of turbulent flow, which becomes almost invariant along the rotation vector $\boldsymbol{\Omega}$. On the other hand, the Coriolis force affects the dynamics of the velocity field only if the latter has non-vanishing gradients in the direction of $\boldsymbol{\Omega}$. In particular, in a perfectly two-dimensional (2D) flow the effects of rotation disappear because the Coriolis force is canceled by pressure gradients. Considering that the reduction of the thickness H of the layer enhances the two-dimensionalization of the flow [32], we expect that also the cyclone-anticyclone asymmetry should be suppressed by the confinement.

In our study, the comparison of experiments and numerical simulations is not intended to reproduce exactly the same physical setup. Our aim is to compare two systems with structural differences related to their boundary conditions. In the experiment, the turbulent flow is subject to friction with the bottom wall of the tank, which causes the development of an Ekman layer. In the numerics the boundary conditions are periodic in all directions and the bottom friction is absent. In the numerical simulations the large-scale energy transfer induced by rotation and vertical confinement [32] eventally leads to the phenomenon of spectral condensation at the horizontal scale of box. In the experiments this phenomenon does not occur because the turbulent flow is surrounded by still fluid and the diameter of the tank is much larger than the typical size of the vortices generated by the comb. Despite these differences, we show that the effects of the vertical confinement on the cyclone-anticyclone asymmetry is similar: it causes a retardation of the growth of S_ω.

5.2 Experimental setup and procedure

The experiments have been performed in the rotating tank of the TurLab facility in Turin. The tank has a diameter of $5m$ and it rotates anticlockwise with periods that range from 90 to 3 seconds. In the experiment the period of rotation was set to $T = 17.6s$, corresponding to an angular velocity $\Omega = 2\pi/T = 0.357 rad/s$.
The tank has been filled with fresh water at four different heights $H = (10, 16, 24, 32)cm$. Water is seeded with Polyamide particles (Arkema Orgasol), with density of 1.03 g/cm^3 and diameter $d = 20 \pm 2\,\mu m$, which are used for the visualization of the flow using the Particle Image Velocimetry technique (see Section 3.2 for a complete description). The particles are illuminated by an horizontal laser sheet, at $6cm$ above the floor of the tank, generated by a Quantum Opus solid state diode green laser. The images are acquired by a 8-bits camera Dalsa Falcon 4M60 with 2352×1728 pixels resolution (further details of the tank and of the acquisition system can be found in [34]). The camera is located $1.43m$ above the horizontal laser sheet. Before the beginning of the experiment, the fluid is set to solid body rotation by increasing gradually the angular velocity of the tank. Then, trails of vortices are generated by the horizontal motion of a comb, which is mounted on a motorized linear guide. The comb is composed by six vertical flat plates of width $a = 2.3cm$ with a mesh size of $M = 10cm$. It moves with constant velocity $V = 18cm/s$ over a distance $L = 90cm$. In order to avoid the formation of waves, the velocity of the comb is smoothly reduced to zero close to the extremities of the guide, before inverting the direction of motion. The comb Reynolds and Rossby numbers, defined in terms of the comb velocity

V and and the mesh spacing M as in [66], are $Re_c = VM/\nu = 1.8 \times 10^4$ and $Ro_c = V/(2\Omega M) = 2.5$. A schematic of the experimental setup is represented in Figure 5.1.

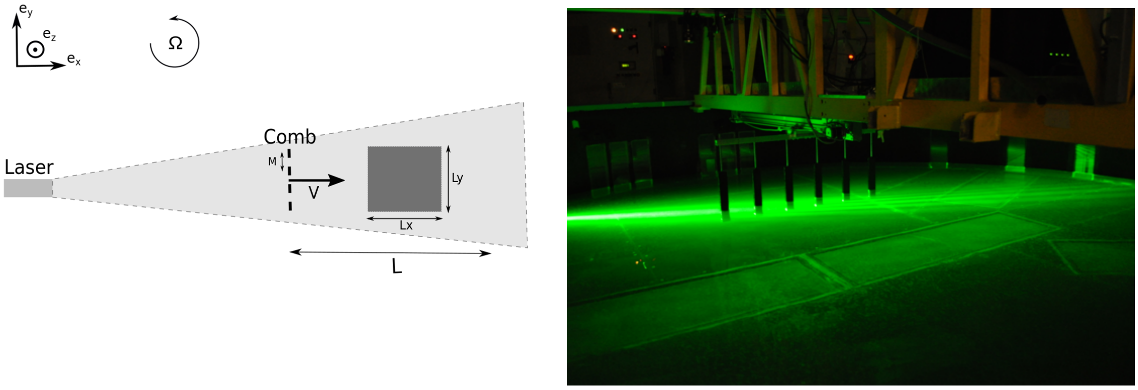

Figure 5.1: Left panel: Schematic of the experimental setup. Right panel: Photo of the experimental setup

After 10 minutes of initial forcing, the comb is stopped and the decay of the flow is recorded for 1 minute with an acquisition rate of $60Hz$. The forcing is resumed for a duration of 2 minutes and then stopped before the next recording. The procedure is repeated 15 times for each height H of the fluid layer.

As described in Section 3.2 of Chapter 3, the velocity fields are obtained by standard PIV analysis, using the Open Source Particle Image Velocimetry software (OpenPIV, for more detail see [95]) with an interrogation window of 32x32 pixels size and an overlap of 16 pixels. The resulting velocity fields cover a rectangular area of size $L_x = 28cm$ and $L_y = 20.5cm$ and are defined on a grid of 116×85 points with a uniform spatial resolution of $\Delta x = \Delta y = 0.241cm$. We reconstructed the velocity fields with a sampling rate of $0.1s$, skipping an initial time of $0.5s$ from the last passage of the comb to avoid the disturbances of the free surface.

The measured velocity fields are the superposition of the turbulent fields $\boldsymbol{u}(\boldsymbol{x}, t)$ and a uniform velocity $\boldsymbol{U}(t)$ which is due to the large-scale circulation induced by the comb and the inertial waves. The inertial waves manifest in the time series of $U_x(t)$ and $U_y(t)$ as oscillations with period which is half of the rotation period of the tank $T_{IW} = T/2$ and a phase shift of $\pi/2$ between U_x and U_y. Before proceeding to the analysis of the data we have subtracted the uniform velocity $\boldsymbol{U}(t)$ (as in [66]).

The time-series presented in section 6.4 are first averaged at fixed time over the ensemble of 15 experiments at given height and further time-averaged over a window of $1s$. The experimental data have been nondimensionalized using the comb scale M, the rms horizontal velocity at initial time

$u_0 = \langle (u_x^2 + u_y^2)/2 \rangle^{1/2}(t=0)$ and the timescale $T_0 = M/u_0$.

5.3 Numerical simulations

Besides the experiments, we also performed a series of direct numerical simulations (DNS) of an incompressible velocity field in a rotating domain with variable height. The dynamics of the velocity field $\boldsymbol{u}(\boldsymbol{x}, t)$ is described by the rotating Navier-Stokes equation:

$$\partial_t \boldsymbol{u} + \boldsymbol{u} \cdot \boldsymbol{\nabla} \boldsymbol{u} + 2\boldsymbol{\Omega} \times \boldsymbol{u} = -\frac{\boldsymbol{\nabla} p}{\rho} + \nu \nabla^2 \boldsymbol{u} \tag{5.1}$$

where $\boldsymbol{\Omega} = (0, 0, \Omega)$ is the angular velocity of the reference frame, ρ is the uniform density of the fluid, ν is the kinematic viscosity, and the pressure p is determined by the condition $\nabla \cdot \mathbf{u} = 0$.

As described in Chapter 4, we perform Direct Numerical Simulation by means of a standard $2/3$-dealiased, pseudospectral code with second-order Runge-Kutta integration scheme. The velocity field is defined on a triply-periodic domain with fixed horizontal sizes $L_x = L_y = 2\pi$ and variable height $H = (1/4, 1/2, 1) \times 2\pi$. It is discretized on a uniform grid at resolution $N_x = N_y = (H/L_x)N_z = 512$. For each height H we consider two values of the angular velocity $\Omega = (1, 2)$. The viscosity is set to $\nu = 10^{-3}$.

At time $t = 0$, the velocity field is initialized as the superposition of a large-scale two-dimensional, two-component (2D2C) flow, and a small three-dimensional, three-component (3D3C) perturbation. The 2D2C large-scale flow mimics the 2D vortices generated by the comb in the experiment. Nonetheless, it is worth to notice that the initial flows in the DNS and experiments are not identical. In the DNS the small 3D perturbation requires some time to develop the 3D turbulent flow. In the experiments, 3D turbulence is already present in the initial flow as a result of the previous passeges of the comb.

The velocities u_x and u_y of the 2D2C flow are defined in Fourier space as the sum of random Gaussian horizontal modes $(k_x, k_y, k_z = 0)$ with $k_h = (k_x^2 + k_y^2)^{1/2}$ in the range $4 < k_h < 6$. The 3D3D perturbation is defined in the Fourier space as the sum of random Gaussian modes in the shell $2 < |\boldsymbol{k}| < 8$. The amplitude of the perturbation field is 5×10^{-4} smaller than the 2D2C flow.

For each height H we performed 10 simulations with different initial random flow, keeping constant the kinetic energies of the base flow and of the perturbation. The time-series presented in section 6.4 are obtained from the ensemble average at fixed time of the data obtained in the 10 simulations with given H. The data of the DNS are nondimensionalized using the scale

$L_0 = 2\pi/4$, corresponding to the largest wave-length of the initial flow, the rms horizontal velocity at initial time $u_0 = \langle (u_x^2 + u_y^2)/2 \rangle^{1/2}(t = 0)$, ($u_0 = 0.93$ for all (H, Ω)) and the timescale $T_0 = L_0/u_0$.

5.4 Experimental and numerical results

In Figure 5.2 we show two examples of the typical vorticity fields obtained in the experiments and in the DNS. More precisely, the left panel shows a square portion (with size $L_y \times L_y$) of the vertical vorticity field $\omega_z = \partial_x u_y - \partial_y u_x$ at time $t = 1.8T_0$ in the experiments at $H = 32cm$, while the right panel shows a section at $z = 0$ of the vertical vorticity field $\omega_z(x, y, z = 0)$ at time $t = 7.1T_0$ in the simulations at $H = \pi/2$ and $\Omega = 1$. In both the experiments and the DNS it is clearly visible the presence of large-scale cyclonic vortices (represented in red).

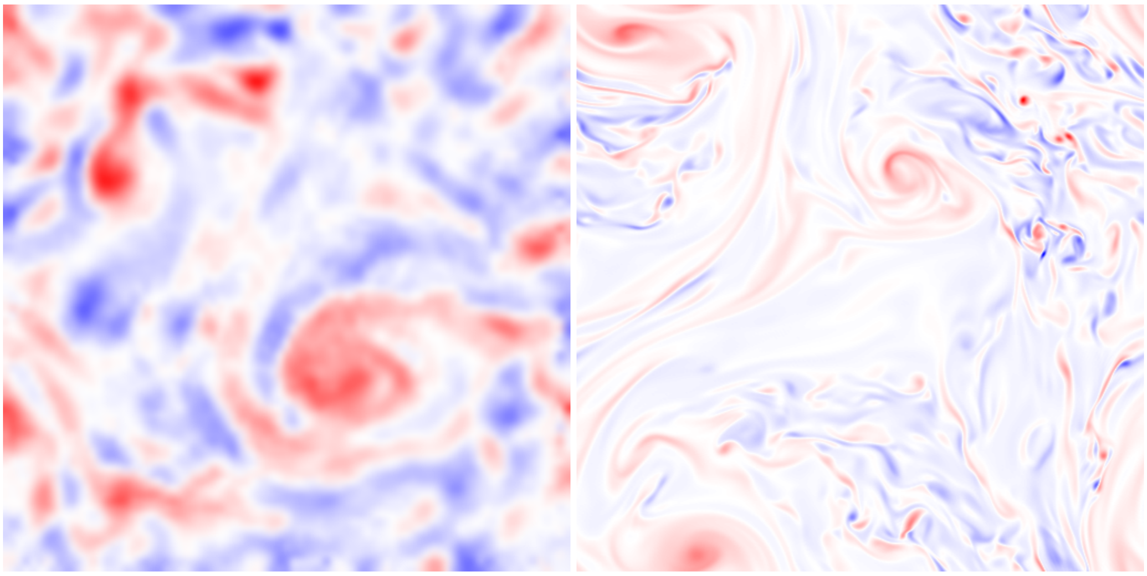

Figure 5.2: Vertical vorticity field in the experiments with $H = 32cm$ at time $t = 1.8T_0$ (left panel) and in the DNS with $H = \pi/2$ and $\Omega = 1$ at time $t = 7.1T_0$ (right panel). Cyclonic vortices are represented in red.

The formation of these structures during the decay of the rotating flow causes an increase of the horizontal correlation scale. In order to quantify this effect we first compute the longitudinal correlation function of horizontal velocity $C(r, t) = \langle u_\alpha(\boldsymbol{x}, t) u_\alpha(\boldsymbol{x} + r\boldsymbol{e}_\alpha, t) \rangle / \langle u_\alpha(\boldsymbol{x}, t)^2 \rangle$ with $\alpha = (x, y)$. Then we define the correlation length $L_c(t)$ as the scale at which $C(L_c) = 0.8$. The time evolution of L_c is shown in Figure 5.3. In both the experiment and the DNS we observe a weak dependence of L_c on H. The scale L_c increases almost linearly in time for $t > T_0$. Previous studies have reported a different scaling $L_c(t) \simeq t^\beta$ with exponent β in the range $(0.2, 0.4)$ [50, 66]. We note that the growth of L_c is faster in the DNS than in the experiments: in the DNS the average growth rate of L_c is $L_c/L_0 \simeq 0.05t/T_0$, while in the experiments it is $L_c/M \simeq 0.03t/T_0$. This effect could be caused by the 2D2C initial condition in the DNS, which induce a 2D dynamics characherized by stronger large-scale energy transfer.

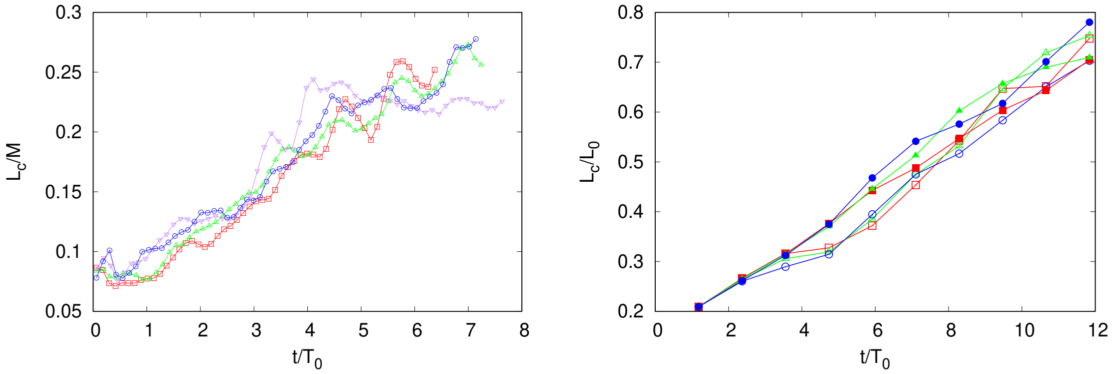

Figure 5.3: Left panel: Velocity correlation length L_c in the experiments at $\Omega = 0.357 rad/s$ with $H = 10cm$ (red squares), $H = 16cm$ (green triangles), $H = 24cm$ (purple down-pointing triangles) and $H = 32cm$ (blue circles). Right panel: Velocity correlation length L_c in the DNS with $H = \pi/2$ (red squares), $H = \pi$ (green triangles) and $H = 2\pi$ (blue circles) at angular velocity $\Omega = 1$ (empty symbols) and $\Omega = 2$ (filled symbols).

The growth of the correlation scale influences the time evolution of the Reynolds and Rossby numbers, defined as

$$Re(t) = \frac{u_h(t)L_c(t)}{\nu} \ , \quad Ro(t) = \frac{u_h(t)}{2\Omega L_c(t)} \ , \tag{5.2}$$

where $u_h(t)$ is the rms horizontal velocity $u_h = (\langle (u_x^2 + u_y^2)/2 \rangle^{1/2})$. As shown in Figure 5.4 (left panel), in the experiments, after an initial rapid decay at $t < T_0$, the Reynolds number remains approximatively constant with some fluctuations (similarly to what observed in [66]). Conversely, in the DNS we observe an almost linear increase of $Re(t)$, which indicates that the growth of $L_c(t)$ overwhelms the decay of the velocities. We argue that the difference between the behavior of two systems could be ascribed to their different boudary conditions. In the experiments the bottom friction (which is absent in the DNS) causes a faster decay of the velocities, resulting in a different temporal evolution of Re. The dependence of $Re(t)$ on H is unclear: in the experiments with the thinner layer ($H = 10cm$) the values of Re are on average smaller than those measured with the thickest layer ($H = 32cm$), but we observe the opposite behavior in the DNS with $\Omega = 1$.

The Rossby number decreases in time both in the experiments and in the numerics (see Figure 5.5) and it is almost independent on H. At long times $t > T$ we observe a scaling regime $Ro(t) \simeq t^{-1}$. This scaling has been

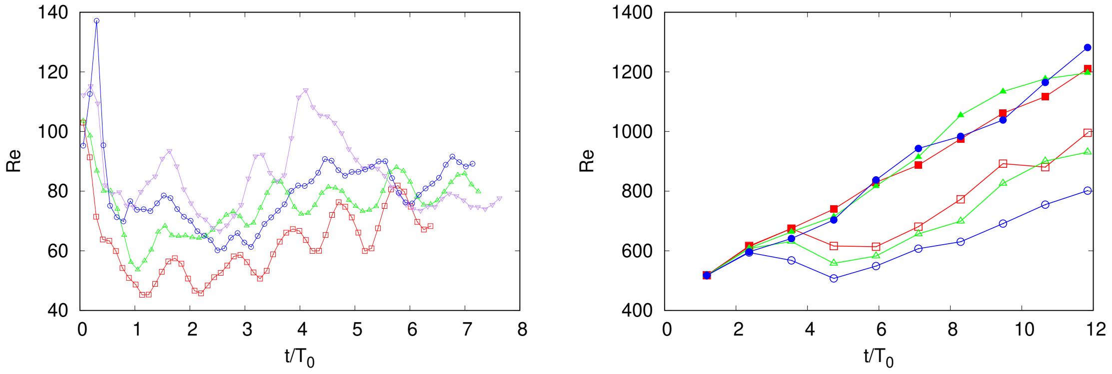

Figure 5.4: Reynolds number $Re = L_c u_{rms}/\nu$ in the experiments (left panel) and in the DNS (right panel) at angular velocity $\Omega = 1$ (empty symbols) and $\Omega = 2$ (filled symbols). Symbols as in Figure 5.3.

previously reported in [66]. The decay of the Rossby number indicates that the Coriolis force prevails over the inertial forces at long times. Therefore the effects of rotation are expected to become more pronounced as the system evolves.

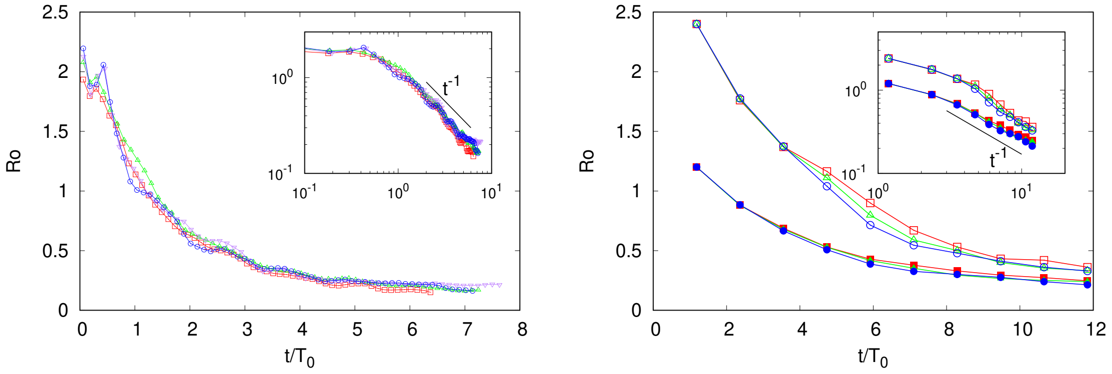

Figure 5.5: Rossby number $Ro = u_{rms}/2\Omega L_c$ in the experiments (left panel) and in the DNS (right panel) at angular velocity $\Omega = 1$ (empty symbols) and $\Omega = 2$ (filled symbols). Symbols as in Figure 5.3.

In Figure 5.6 we compare the energy spectra $E_h(k)$ of the horizontal velocity fields u_x, u_y in the experiments at $t = 1.8T_0$ (left panel) and in the DNS at time $t = 7.1T_0$ (right panel). In the experiments we observe a power-law spectrum $E_h(k) \simeq k^{-2}$ in the wavenumber range $6 < kM < 20$. A similar spectral slope is observed also in the DNS at $\Omega = 1$ in the range $10 < kL_0 < 30$, while the simulations with $\Omega = 2$ have steeper spectra. In both the experiments and DNS the spectra are almost independent on the heights H. In the spectra of the DNS it is possible to observe a beginning of accumulation of energy in the lowest accessible mode. The spectral condensation is clearly visible in the spectra at late times of the DNS (not shown).

Conversely, this phenomenon is not observed in the experiments because of the large scale separation between the diameter of the tank and the typical size of the vortices produced by the comb.

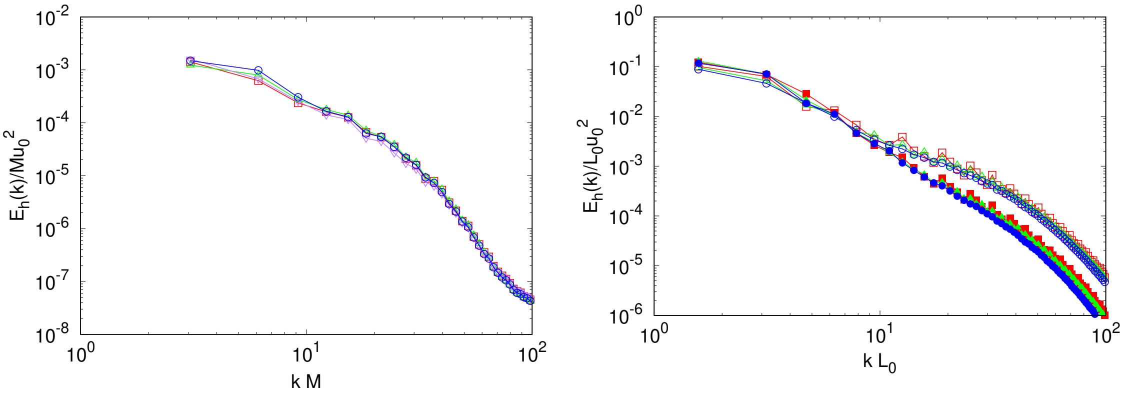

Figure 5.6: Horizontal energy spectra in the experiments at time $t = 1.8T_0$ (left panel) and in the DNS at time $t = 7.1T_0$ (right panel) at angular velocity $\Omega = 1$ (empty symbols) and $\Omega = 2$ (filled symbols). Symbols as in Figure 5.3.

The results presented so far do not show a strong dependence on the height of the fluid layer. On the contrary, the effect of varying H is clearly visible in the statistics of the vertical component of the vorticity $\omega_z = \partial_x u_y - \partial_y u_x$. The probability distribution functions (PDF) of ω_z are shown in Figure 5.7 for different values of H at a fixed time $t = 1.8T_0$ in the experiments and $t = 7.1T_0$ in the DNS. The PDFs corresponding to the large H are characterized by a positive skewness $S_\omega = \langle \omega_z^3 \rangle / \langle \omega_z^2 \rangle^{3/2}$, which quantifies the cyclone-anticyclone asymmetry. Reducing the thickness H, the PDFs become more symmetric and the skewness is reduced. This means that the confinement of the decaying flow in a thin layer weakens the cyclone-anticyclone asymmetry at fixed time. This is in qualitative agreement with previous numerical results in forced stationary conditions [32].

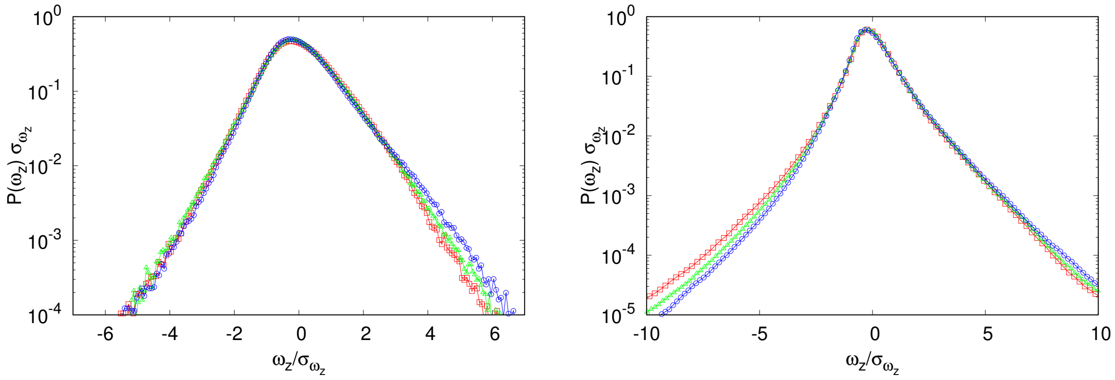

Figure 5.7: PDFs of the vertical vorticity ω_z in the experiments at time $t = 1.8T_0$ (left panel) and in the DNS at time $t = 7.1T_0$ at angular velocity $\Omega = 1$ (right panel). Symbols as in Figure 5.3.

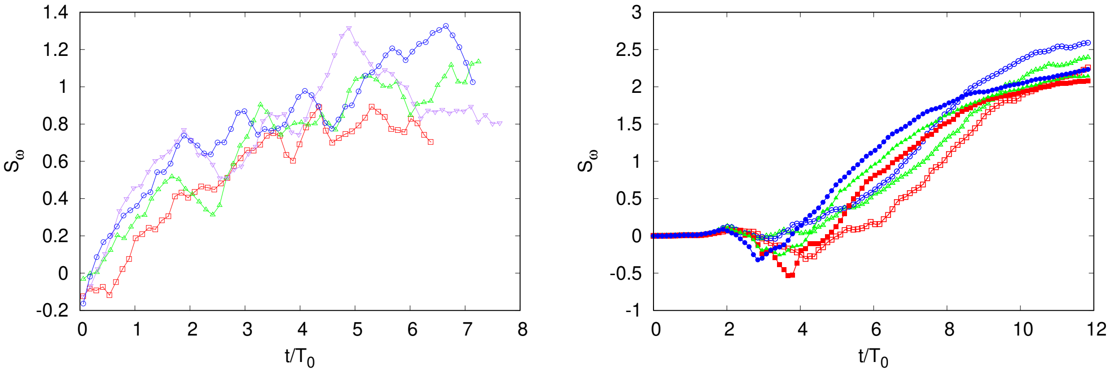

Figure 5.8: Skewness of the vertical vorticity ω_z in the experiments (left panel) and in the DNS (right panel) at angular velocity $\Omega = 1$ (empty symbols) and $\Omega = 2$ (filled symbols). Symbols as in Figure 5.3.

Because of the decay of the Rossby number, it is expected that the cyclone-anticyclone asymmetry increases with time. Previous studies [66, 71] reported a power-law growth of the skewness $S_\omega \simeq t^\gamma$ with $\gamma \approx 0.70 \pm 0.05$. Here we are interested to investigate how the height H of the fluid layer influences the growth of S_ω. The temporal evolution of S_ω is shown in Figure 5.8. In all the simulations and experiments, after an initial transient we observe the development of a positive skewness, which indicates the prevalence of cyclones over anticyclones. In the DNS, we find that the regime of positive skewness is systematically preceded by a transient in which S_ω is negative. We are not aware of previous observations of this phenomenon. After the negative transient, the skewness in the DNS grows as $S_\omega(t) \sim (t - t_*)^{0.80 \pm 0.05}$ (not shown), being t_* the time at which S_ω changes sign from negative to positive. The value of the exponent is in agreement with the results reported in [71].

The series of $S_\omega(t)$ obtained in the numerics display a clear dependence on H. Smaller H correspond to smaller values of S_ω at fixed short time. A similar dependence on H is observed also in the experimental series, even if they are more noisy. After the initial growth, the skewness saturates to almost constant values at late times both in the DNS (for $t > 8T_0$) and experiments (for $t > 4T_0$). In the numerical series with $\Omega = 2$ the asymptotic value of the skewness has not a clear dependence on H. In the experiments with $H = 24cm$ we observe a decay of S_ω at $t > 5T_0$. It is tempting to interpret this as the beginning of the long time decay of the vorticity skewness which has been reported in previous studies (e.g.[66]). Nonetheless, even after averaging over 15 independent experiments, our data displays strong temporal fluctuations which do not allow to make accurate statements concerning the late stage of the evolution of the skeweness. The inspection of the numerical series in Figure 5.8 suggests that, while the cyclone-anticyclone asymmetry

develops for all the cases with different H considered here, reaching similar values of S_ω at the end of the simulations, the main effect of the confinement of the flow in a thin layer is to delay its development.
To test this idea, in Figure 5.9 we plot the series of $S_\omega(t)$ by rescaling the times with height-dependent time scales T_H. The values of T_H have been determined by least square method, minimizing the differences between $S_\omega(t/T_H)$ at given H with respect to the case with the largest $H = H_{max}$ ($H_{max} = 32cm$ in the experiments and $H_{max} = 2\pi$ in the DNS), and fixing $T_{H_{max}} = T_0$. The collapse of the series is reasonably good, and the rescaling times T_H become larger as the thickness H is reduced. We note that the values of T_H/T_0 are identical in the DNS with $\Omega = 1$ and $\Omega = 2$. This shows that the confinement in a thin layer slows down the development of the cyclone-anticyclone asymmetry. It is interesting to note that this effect is qualitatively similar in the experiment and in the DNS, in spite of the differences between the two systems highlighted in the introduction and observed in the temporal evolution of the correlation scale (Fig. 5.3) the Reynolds mumber (Fig. 5.4) and the spectra (Fig. 5.6).

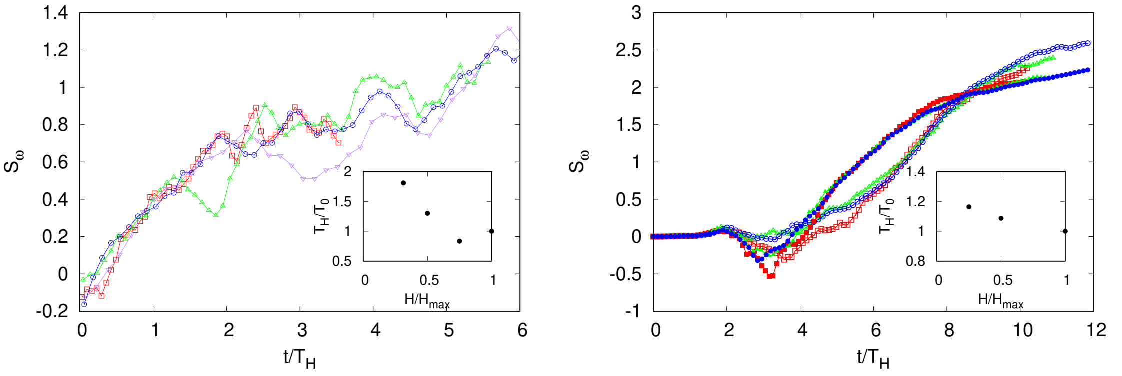

Figure 5.9: Skewness of the vertical vorticity ω_z in the experiments (left panel) and in the DNS (right panel) at angular velocity $\Omega = 1$ (empty symbols) and $\Omega = 2$ (filled symbols). Time has been rescaled with T_H. The values of T_H are shown in the insets. Symbols as in Figure 5.3.

Finally we present a result of the late-stage of the decay in the DNS. We have continued the DNS up to time $t = 24T_0$. At that time, the turbulent fluctuations are almost completely disappeared, and the velocity field consists of a single cyclonic vortex. Because in the DNS the mean vorticity is constrained to be zero, the vortex is surrounded by a sea of negative vorticity. As one can see in Figure 5.10, the PDF of the vorticity field of this fossil state of turbulence displays an interesting feature: its negative tail has a sharp cutoff at $\omega_z = -2\Omega$. In other words, at long times the total vorticity computed in the laboratory frame $\omega_z + 2\Omega$ is always positive. This result contrasts with the recovery of the symmetry at long times which has been observed in [68, 66].

As discussed in Ref. [66], the symmetry is expected to be restored only if the initial state contains a significant amount of vertical velocity, which is almost absent in our case. It would be interesting to investigate more systematically how this phenomenon is dependent on the properties of the initial velocity field and on the boundary conditions.

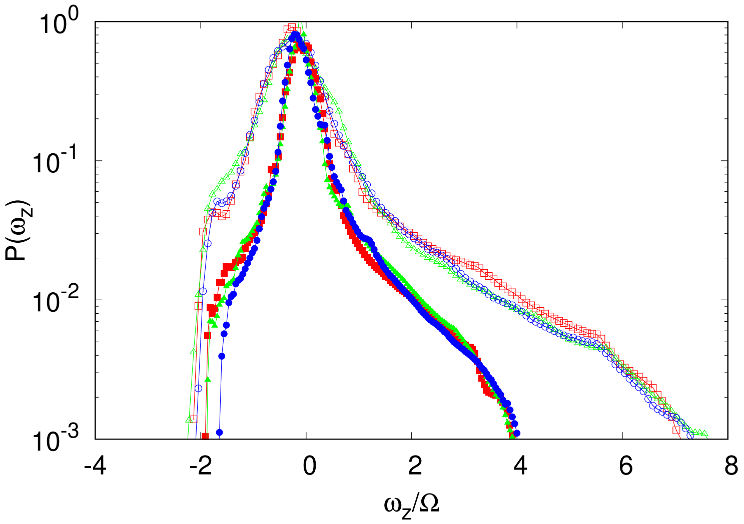

Figure 5.10: PDFs of the vertical vorticity ω_z in the numerical simulations at time $t = 24T_0$ at angular velocity $\Omega = 1$ (empty symbols) and $\Omega = 2$ (filled symbols). Symbols as in Figure 5.3.

5.5 Conclusions

The main result of our study is that the confinement of a turbulent rotating flow in a thin layer delays the development of the cyclone-anticyclone asymmetry. This effect is observed both in experiments and in numerical simulations which have structural differences in the boundary conditions, and it is therefore a robust feature of decaying rotating flows, independent on the presence of bottom friction. Our findings show that the, although the formation of the cyclone-anticyclone asymmetry is obseved both with and without vertical confinement, the height of the fluid layer is a crucial parameter to determine the temporal scale of this phenomenon. Further experiments and numerical simulations are needed to better understand how the mechanism of formation of cyclonic columnar structures are influenced by the vertical confinement.

Our results have important implication for large-scale geophysical flows, where the height of the fluid layer is typically smaller than the horizontal scales. The cyclone-anticyclone asymmetry observed in these conditions could be much weaker than what expected on the basis of experiments and

DNS with aspect ratio of order unity.

Chapter 6

Effects of rotation on the bulk turbulent convection

This chapter has been published:
F. Toselli, S. Musacchio and G. Boffetta, Effects of rotation on the bulk turbulent convection, *Journal of Fluid Mechanics*, 881, 648 (2019).
https://doi.org/10.1017/jfm.2019.764

In this work we study rotating homogeneous turbulent convection forced by a mean vertical temperature gradient by means of direct numerical simulations (DNS) in the Boussinesq approximation in a rotating frame. In the absence of rotation our results are in agreement with the "ultimate regime of thermal convection" for the scaling of the Nusselt and Reynolds numbers vs Rayleigh and Prandtl numbers. Rotation is found to increase both Nu and Re at fixed Ra with a maximum enhancement for intermediate values of the Rossby numbers, qualitatively similar, but with stronger intensity, to what observed in Rayleigh-Bénard rotating convection. Our results are interpreted in terms of a quasi-bidimensionalization of the flow with the formation of columnar structures displaying strong correlation between the temperature and the vertical velocity fields.

6.1 Introduction

Turbulent convection involves the coupling between an active temperature field transported by a turbulent flow in presence of gravity. Within this general framework, different examples of turbulent convection are characterized essentially by boundary conditions which force the flow in different ways. In the most common configurations temperature difference is parallel to gravity, as in the case of Rayleigh-Bénard (RB) convection, in which the flow is confined into a box with fixed temperatures on the two horizontal boundaries [9, 1] or for Rayleigh-Taylor (RT) convection, which is forced by two reservoirs of fluid at different temperature [11]. Another geometry, which has become very popular for numerical simulations, is the so-called *bulk turbulent convection* (BTC) in which the flow is forced by an imposed vertical temperature linear gradient. BTC is motivated by the study of the ultimate state regime predicted by [54], which is supposed to appear in RB convection when the contribution of boundary layers become negligible [45]. Moreover, it is similar to the turbulent phase of RT convection where a linear temperature (density) profile naturally appears and both RT and BTC display the ultimate state regime [61, 20, 10].

Several internal and external factors can modify the dynamical and statistical properties of turbulent convection: among the latters, rotation along the vertical axis is known to affect the efficiency of turbulent transport of heat in both RB and RT convection. The study of the effects of rotation is of great interest because of its relevance for geophysical and astrophysical applications, including convection in the oceans [63] and in the atmosphere [48, 80]), convection inside gaseous giant planets [19] or in external layer of the Sun [65]), and for technological applications [51].

Linear stability analysis, performed originally by [23] for RB shows that rotation has a stabilizing effect and this suggests that it might reduce the transfer of heat in the nonlinear, turbulent phase. However, the work by [82] shows that rotation can also increase the heat transport. This enhancement is explained by the mechanism of Ekman pumping [102, 53, 56, 52] that contributes to a vertical heat flux produced by an extra vertical circulation due to a suction of fluid at the two boundary layers. The effect of rotation in turbulent RB convection has been extensively studied by means of experiments [18, 56, 73, 58] and numerical simulations [86, 93, 92, 28]. The picture which emerges is that the heat transport between the hot and the cold plate, measured by the dimensionless Nusselt number Nu (all parameters are defined below), has a non-monotonic dependence on the rotation, identified by the dimensionless Rossby number Ro: moderate rotations enhance the heat transfer while stronger rotations bring to an important suppression of the vertical velocities and to a reduction of the heat transport.

In the case of RT convection, the effect of rotation has been studied more recently by means of both experiments [2] and DNS within the Boussinesq approximation [13]. The main result is that rotation always reduces the turbulent heat transfer in this case. The mechanism for this reduction is due to a partial decoupling and decorrelation of the temperature and the vertical velocity fields which reduces the Nusselt number. This result does not contrast with the enhancing mechanism associated to the Ekman pumping which has been observed in the RB case, because of the absence of boundary layers in the RT system.

The aim of this work is to investigate the effects of rotation on the heat transfer within the framework of the BTC, driven by a mean temperature gradient. Surprisingly, at variance with RT convection, we find a strong enhancement of the Nusselt number (at fixed Rayleigh number) induced by rotation. A detailed analysis shows that the heat flux is mainly due to the formation of convective columnar structures produced by the quasi-bidimensionalization of the flow.

The remaining of this work is organized as follow. Section 6.2 is devoted to the description of the numerical simulations while in section 6.3 we discuss the dependence of Nusselt and Reynolds number on rotation. In Section 6.4 we investigate the role played by the columnar structures generated by the rotation in the process of heat transfer. Finally, conclusions are reported in Section 6.5.

6.2 Mathematical model and numerical method

We perform extensive numerical simulations of BTC by integrating the Boussinesq equations for an incompressible flow forced by a mean unstable temperature gradient $-\gamma$ in a cubic box of size L [15, 61]. The temperature field is therefore written as $T(\mathbf{x},t) = -\gamma z + \theta(\mathbf{x},t)$, where $\theta(\mathbf{x},t)$ represents the fluctuation field. The Boussinesq equations, written in a reference frame rotating with angular velocity $\boldsymbol{\Omega} = (0,0,\Omega)$ along the z axis, read

$$\partial_t \mathbf{u} + \mathbf{u}\cdot\nabla\mathbf{u} + 2\boldsymbol{\Omega}\times\mathbf{u} = -\nabla p + \nu\nabla^2\mathbf{u} - \beta\mathbf{g}\theta \tag{6.1}$$

$$\partial_t \theta + \mathbf{u}\cdot\nabla\theta = \kappa\nabla^2\theta + \gamma w \tag{6.2}$$

where $\mathbf{u} = (u,v,w)$ is the incompressible ($\nabla\cdot\mathbf{u} = 0$) velocity field, p is the pressure, β is the thermal expansion coefficient, $\mathbf{g} = (0,0,-g)$ is gravity, ν is the kinematic viscosity and κ the thermal diffusivity.

The dimensionless parameters which govern the flow are the Rayleigh number, defined as $Ra = \beta g\gamma L^4/(\nu\kappa)$ (where L is the size of the system), the Prandtl number $Pr = \nu/\kappa$ and the Rossby number, here defined as $Ro = \sqrt{\beta g\gamma}/(2\Omega)$, which measures the (inverse) intensity of rotation as the ratio between the buoyancy and Coriolis force. When the turbulent flow reaches a statistical stationary condition, we measure velocity and temperature fluctuations and their correlation from which we compute the Reynolds number $Re = UL/\nu$ (where $U = \sqrt{\langle|\,\mathbf{u}^2\,|\rangle/3}$ is the root mean square of all velocity components) and the Nusselt number is defined as $Nu = \langle w\theta\rangle/(\kappa\gamma) + 1$ with $\langle ... \rangle$ indicating the average over the volume.

Ra	Pr	Ro	Nu	Re	Ω	ν	κ
1.1×10^7	10	∞	3.12×10^3	4.57×10^2	0	6.00×10^{-3}	6.00×10^{-4}
1.1×10^7	10	3.16×10^{-1}	5.86×10^3	6.04×10^2	0.25	6.00×10^{-3}	6.00×10^{-4}
1.1×10^7	10	1.58×10^{-1}	8.19×10^3	6.99×10^2	0.5	6.00×10^{-3}	6.00×10^{-4}
1.1×10^7	10	7.91×10^{-2}	1.14×10^4	8.12×10^2	1	6.00×10^{-3}	6.00×10^{-4}
1.1×10^7	10	3.95×10^{-2}	9.56×10^3	7.60×10^2	2	6.00×10^{-3}	6.00×10^{-4}
1.1×10^7	10	1.98×10^{-2}	9.02×10^3	7.38×10^2	4	6.00×10^{-3}	6.00×10^{-4}
2.2×10^7	1	∞	1.97×10^3	2.48×10^3	0	1.89×10^{-3}	1.89×10^{-3}
2.2×10^7	1	4.47×10^{-1}	2.92×10^3	2.94×10^3	0.25	1.89×10^{-3}	1.89×10^{-3}
2.2×10^7	1	2.23×10^{-1}	3.87×10^3	3.31×10^3	0.5	1.89×10^{-3}	1.89×10^{-3}
2.2×10^7	1	1.12×10^{-1}	5.18×10^3	3.77×10^3	1	1.89×10^{-3}	1.89×10^{-3}
2.2×10^7	1	5.59×10^{-2}	5.29×10^3	3.84×10^3	2	1.89×10^{-3}	1.89×10^{-3}
2.2×10^7	1	2.79×10^{-2}	3.43×10^3	3.41×10^3	4	1.89×10^{-3}	1.89×10^{-3}
2.2×10^7	5	∞	3.67×10^3	1.02×10^3	0	4.24×10^{-3}	0.85×10^{-3}
2.2×10^7	5	4.47×10^{-1}	4.86×10^3	1.15×10^3	0.25	4.24×10^{-3}	0.85×10^{-3}
2.2×10^7	5	2.23×10^{-1}	7.70×10^3	1.41×10^3	0.5	4.24×10^{-3}	0.85×10^{-3}
2.2×10^7	5	1.12×10^{-1}	1.10×10^4	1.64×10^3	1	4.24×10^{-3}	0.85×10^{-3}
2.2×10^7	5	5.59×10^{-2}	1.27×10^4	1.77×10^3	2	4.24×10^{-3}	0.85×10^{-3}
2.2×10^7	5	2.79×10^{-2}	8.30×10^3	1.59×10^3	4	4.24×10^{-3}	0.85×10^{-3}
2.2×10^7	10	∞	4.88×10^3	6.87×10^2	0	6.00×10^{-3}	6.00×10^{-4}
2.2×10^7	10	4.47×10^{-1}	6.50×10^3	7.78×10^2	0.25	6.00×10^{-3}	6.00×10^{-4}
2.2×10^7	10	2.23×10^{-1}	9.55×10^3	9.29×10^2	0.5	6.00×10^{-3}	6.00×10^{-4}
2.2×10^7	10	1.12×10^{-1}	1.40×10^4	1.09×10^3	1	6.00×10^{-3}	6.00×10^{-4}
2.2×10^7	10	5.59×10^{-2}	1.60×10^4	1.18×10^3	2	6.00×10^{-3}	6.00×10^{-4}
2.2×10^7	10	2.79×10^{-2}	1.34×10^4	1.13×10^3	4	6.00×10^{-3}	6.00×10^{-4}

Table 6.1: Parameters of the numerical simulations

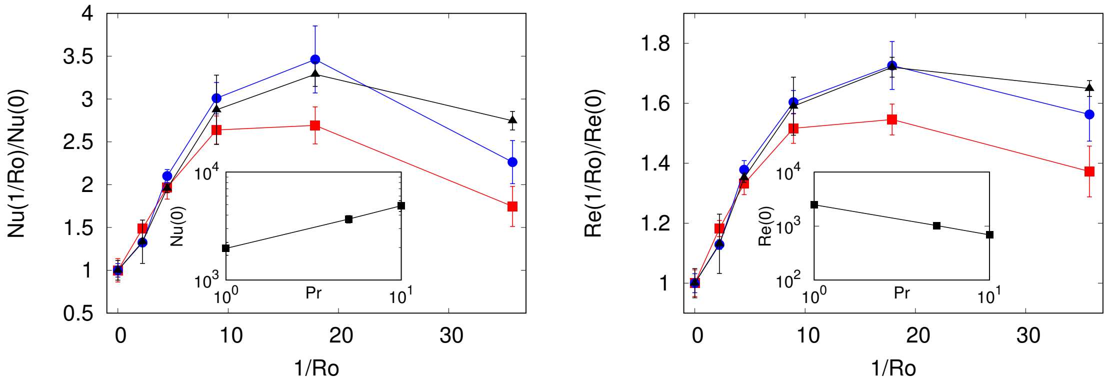

Figure 6.1: Nu (a) and Re (b) as a function of $1/Ro$ normalized with the value at $1/Ro = 0$ for simulations at $Ra = 2.2 \times 10^7$ and $Pr = 1$ (red squares), $Pr = 5$ (blue circles) and $Pr = 10$ (black triangles). The insets show the values of Nu and Re in the absence of rotation ($1/Ro = 0$) as a function of Pr. The lines represent the scaling $Nu(0) \propto Pr^{0.40}$ and $Re(0) \propto Pr^{-0.55}$.

We performed extensive direct numerical simulations of equations (6.1-6.2) by means of a fully parallel pseudo-spectral code, described in Chapter 4, at resolution $N^3 = 512^3$ in a cubic domain of size $L = 2\pi$ with periodic boundary conditions. We explore the set of parameters by considering two different Rayleigh numbers, $Ra = 1.1 \times 10^7$ and $Ra = 2.2 \times 10^7$, three values of the Prandtl number $Pr = 1$, $Pr = 5$ and $Pr = 10$ and 6 different Rossby numbers. The different Pr numbers are obtained by changing both ν and κ by keeping their product constant which fixes the value of Ra. The two different Ra are obtained by changing the mean temperature gradient γ. All parameter values for the simulations are showed in Table 6.1. The maximum value of Ra has been chosen such that in the case $Pr = 1$ and $Ro = \infty$ both the Kolmogorov scale $\eta = (\nu^3/\varepsilon)^{1/4}$ and the Batchelor scale $\ell_B = (\kappa^2\nu/\varepsilon)^{1/4}$ (where $\varepsilon = \nu\langle(\partial_i u_j)^2\rangle$ is the volume averaged kinetic dissipation rate) are well resolved. In terms of the maximum wavenumber $K_{max} = N/3$ we have $K_{max}\eta = K_{max}\ell_B = 2.4$ for the case $Pr = 1$ and $Ro = \infty$. The effects of rotation on the Kolmogorov and Batchelor scales could not be predicted a priori, but we have checked a posteriori that in the worst case we have $K_{max}\eta > 1.8$ (for $\Omega = 4$, $Pr = 1$) and $K_{max}\ell_B > 1.4$ (for $\Omega = 4$, $Pr = 10$). The duration of each simulation is $T = 100\tau$, measured in units of the characteristic time $\tau = 1/\sqrt{\beta\, g\, \gamma}$.

We found that average quantities such as Re and Nu display strong fluctuations in the time series.

Therefore as a measure of the error on the time average of these quantities we use the maximum fluctuation of the running average computed on the second half of the time series.

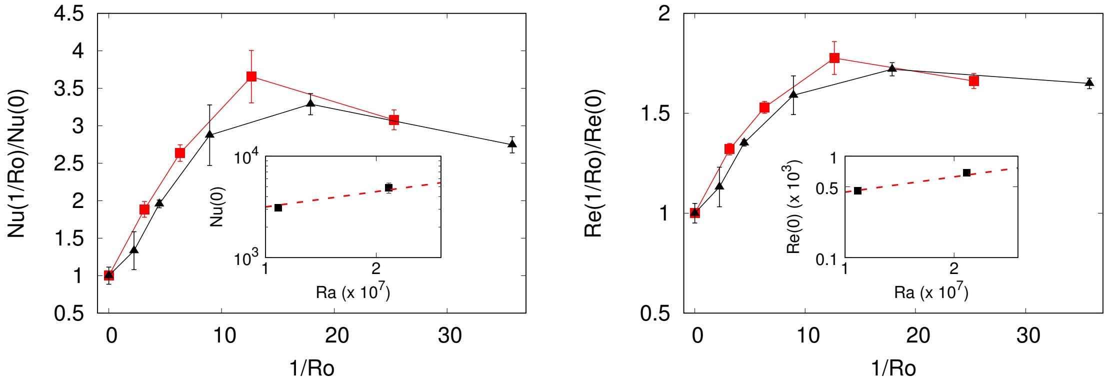

Figure 6.2: Nu (a) and Re (b) as a function of $1/Ro$ normalized with the value at $1/Ro = 0$ for simulations at $Ra = 1.1 \times 10^7$ (red squares) and $Ra = 2.2 \times 10^7$ (black triangles) for the case $Pr = 10$. The insets show the values of Nu (Re) in the absence of rotation ($1/Ro = 0$) as a function of Ra. The dashed red lines represent the scaling $Nu(0) \propto Ra^{1/2}$ and $Re(0) \propto Ra^{1/2}$.

6.3 Nusselt and Reynolds dependence on rotation

In order to study the effects of the Coriolis force on the heat transfer and the turbulence intensity, we first consider the dependence of Nu and Re on the rotation number $1/Ro$ for different values of Pr. In Fig. 6.1 we report the values of Nu and Re rescaled on their respective value in absence of rotation ($1/Ro = 0$) for the simulations at $Re = 2.2 \times 10^7$. We find a non-monotonic dependence: the heat transfer (measured by Nu) and the turbulence intensity (quantified by Re) increase with the rotation rate and they attain a maximum for an optimal value of $Ro \approx 6 \times 10^{-2}$. For stronger rotation rates they decrease slowly. The relative variation with respect to the non-rotating case ($Nu(0)$) is larger for the cases $Pr = 5$ and $Pr = 10$.

The non-monotonic behavior of Nu and Re as a function of Ro, as well as the dependence on Pr, is qualitatively similar to what has been reported in previous works for the case of turbulent RB convection [102, 89, 91, 90]. The main difference between the RB case is the magnitude of the heat transfer enhancement: in our simulations of BTC we observe a maximum relative increase of Nu of a factor 3.5. This enhancement is much larger than the increase of a factor $1.1 - 1.2$ which has been observed in the RB case for Ra in the range of $10^8 - 10^9$ [90]. Moreover, the decay at large rotation rates is much slower in BTC case than in RB case. It is worth to notice that the mechanisms which originate the heat transfer enhancement are different in RB and BTC: in the case of the RB convection, the increase of Nu is mostly due to the effects of the rotation on the boundary layers. The latters are absent on the BTC case, which is dominated by bulk effects.

In absence of rotation, the scaling of $Nu(0)$ and $Re(0)$ as a function of Pr observed in our simulations are $Nu(0) \propto Pr^{0.40}$ and $Re(0) \propto Pr^{-0.55}$

(see inset of Fig. 6.1) The scaling exponents are close to those predicted for the ultimate state of turbulent convection $Nu \propto Ra^{1/2}Pr^{1/2}$ and $Re \propto Ra^{1/2}Pr^{-1/2}$ [54] and they are in agreement with previous numerical results for RB case [20].

We do not observe a strong dependence on Ra for the rotation effects on the heat transfer and turbulent intensity. The curves of $Nu/Nu(0)$ and $Re/Re(0)$ measured for $Pr = 10$ at $Ra = 1.1 \times 10^7$ and $Ra = 2.2 \times 10^7$ are comparable within the errorbars (see Fig. 6.2). The only exception are the values of Nu and Re of the simulation at $Ra = 1.1 \times 10^7$, $Ro = 7.91 \times 10^{-2}$. The inspection of the time serie of this simulation reveals that these anomalous values are due to a single event of strong convection that influenced the whole statistics. In absence of rotation, the dependence of $Nu(0)$ and $Re(0)$ on Ra is in agreement with the ultimate-state scaling laws $Nu(0) \propto Ra^{0.5}$ and $Re(0) \propto Ra^{0.5}$.

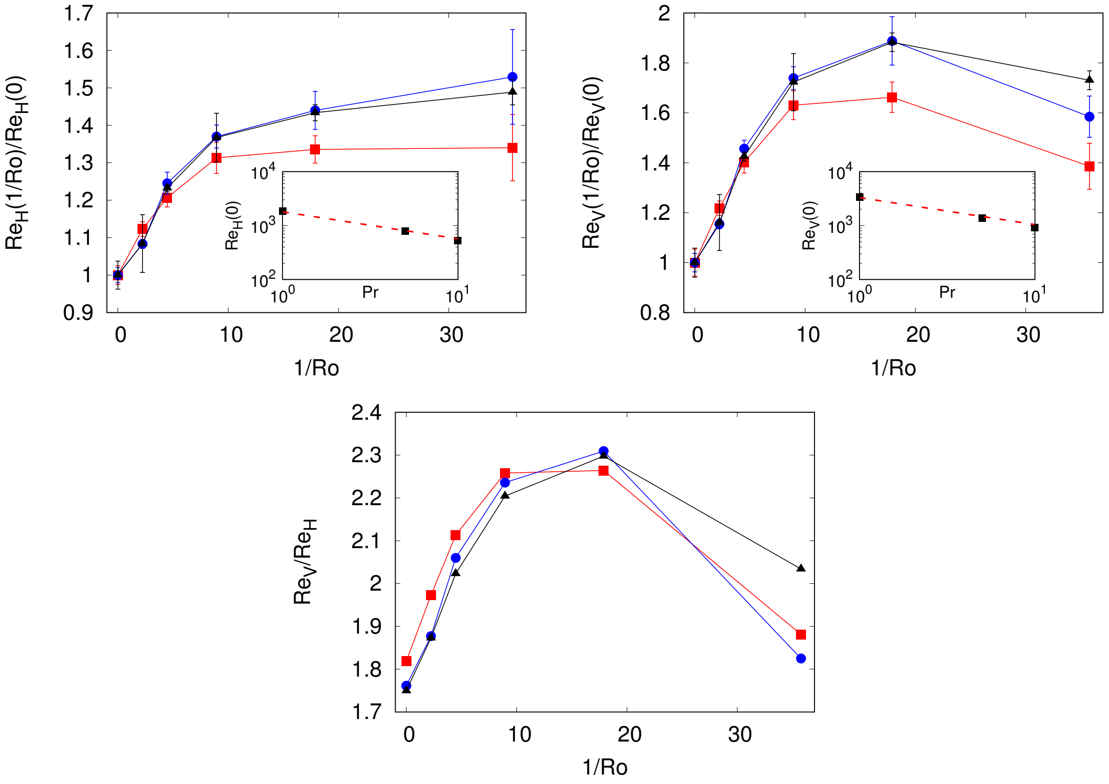

Figure 6.3: Upper panels: Re_H (a) and Re_V (b) as a function of $1/Ro$ normalized with the value at $1/Ro = 0$ for simulations at $Ra = 2.2 \times 10^7$ and $Pr = 1$ (red squares), $Pr = 5$ (blue circles) and $Pr = 10$ (black triangles). The insets show the values of Re_H and Re_V in the absence of rotation ($1/Ro = 0$) as a function of Pr. The dashed lines represent the scaling $Re_{H,V}(0) \propto Pr^{-1/2}$. Lower panel: The ratio Re_V/Re_H (c) as a function of $1/Ro$ for simulations at $Ra = 2.2 \times 10^7$ and $Pr = 1$ (red squares), $Pr = 5$ (blue circles) and $Pr = 10$ (black triangles).

The anisotropy between the horizontal and vertical velocity can be quantified by introducing the horizontal and vertical Reynolds numbers defined

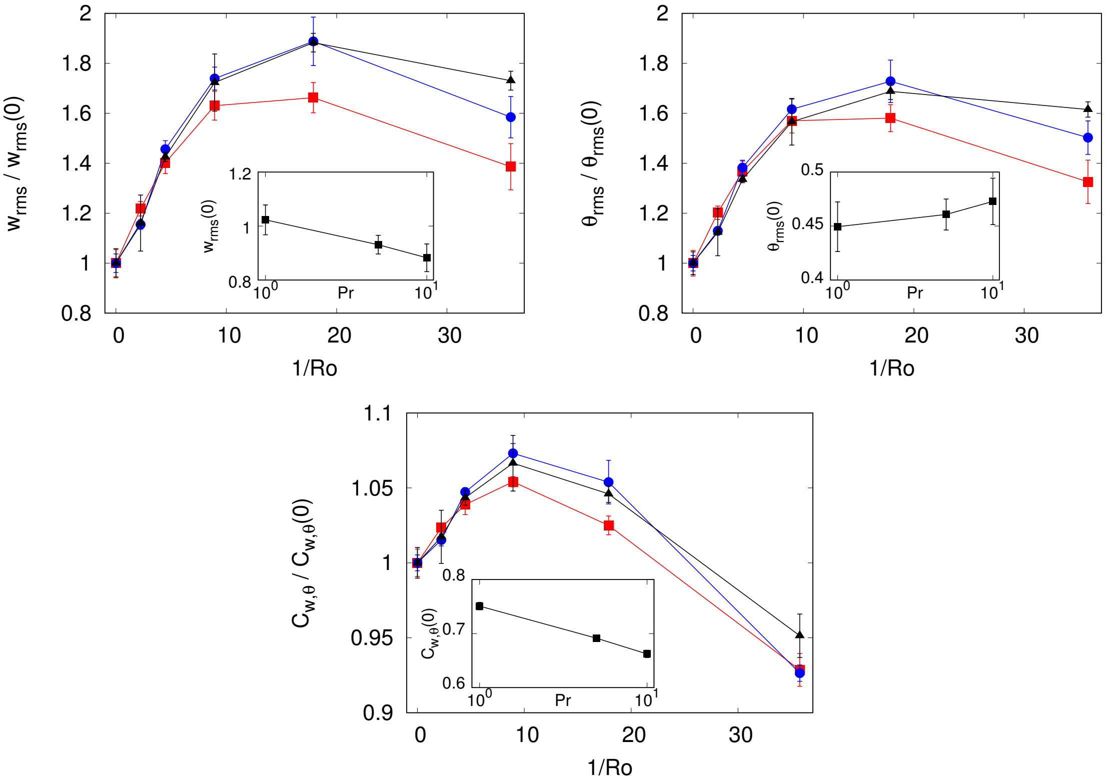

Figure 6.4: Contributions to Nu: w_{rms} (a), θ_{rms} (b) and $C_{w,\theta}$ (c) as a function of $1/Ro$ normalized with their values at $1/Ro = 0$ for simulations at $Ra = 2.2 \times 10^7$ and $Pr = 1$ (red squares), $Pr = 5$ (blue circles) and $Pr = 10$ (black triangles). The insets show the values of $w_{rms}(0)$, $\theta_{rms}(0)$ and $C_{w,\theta}(0)$ in absence of rotation as a function of Pr.

respectively as:

$$Re_H = \frac{u_{rms}L}{\nu} \; , \quad Re_V = \frac{w_{rms}L}{\nu} \; . \tag{6.3}$$

In absence of rotation the dependence of Re_H and Re_V on Pr is in agreement with the ultimate-state scalings $Re_{H,V} \propto Pr^{-1/2}$ (see insets of Fig. 6.3). The behavior of Re_V as a function of $1/Ro$ is non-monotonic and it is similar to the behavior of the total Reynolds number, while the Re_H shows a weaker monotonic increase. In Fig. 6.3 we also show the ratio Re_V/Re_H which gives information on the anisotropy between vertical and horizontal velocities. The anisotropy, which is present already at $1/Ro = 0$, is enhanced by rotation and attains a maximum for $Ro \approx 6 \times 10^{-2}$.

Besides, following [12] we decompose the Nusselt number as the product of three different contributions:

$$Nu = \frac{w_{rms}\theta_{rms}C_{w,\theta}}{\kappa\gamma} + 1 \tag{6.4}$$

where $C_{w,\theta} = \langle w\theta \rangle / (w_{rms}\theta_{rms})$ is the correlation between the vertical velocity component w and the temperature field θ . All the three factors which contribute to Nu display a non-monotonic dependence on the rotation rate (see Fig. 6.4). The largest variations are observed for the rms fluctuations of the vertical velocity and the temperature, which for $Ro = 5.59 \times 10^{-2}$ are about 80% larger than in the case $Ro = \infty$. The variation of the correlation $C_{w,\theta}$ is considerably smaller.

The dependence on Pr of w_{rms}, θ_{rms}, and $C_{w,\theta}$ in absence of rotation (shown in the insets of Fig. 6.4) has a simple physical interpretation. In order to increase Pr keeping Ra fixed, one has to increase the kinematic viscosity as $\nu \propto Pr^{1/2}$ and to decrease the thermal diffusivity as $\kappa \propto Pr^{-1/2}$. The increase of the viscosity suppresses the velocity fluctuations at small scales, and therefore causes a decrease of w_{rms}. Conversely, the reduction of the thermal diffusivity allows for the development of small-scale temperature fluctuations, and therefore causes an increase of θ_{rms}. The opposite behavior of the small-scale structures of the velocity and temperature fields at increasing Pr causes the decrease of the correlation $C_{w,\theta}$.

6.4 Columnar convective structures

The time series of the Nusselt number obtained in our simulations are characterized by strong fluctuations, which correspond to events of weak/strong convection. The standard deviation of these fluctuations is of the order of 50% of their mean values, defined as the time-average over the duration of the simulations (and corresponding to the values reported in the previous section).

We have found that, in the rotating cases, the events of strong convection are related with the formation of columnar structures aligned with the rotation axis, which are present both in the temperature field and in the vertical velocity field. As an example, we show in Figure 6.5 the field θ and w at time $t = 80\tau$, corresponding to a local maximum of the time series of Nu in the simulation with $Ra = 2.2 \times 10^7$, $Pr = 10$ and $Ro = 5.59 \times 10^{-2}$.

The presence of quasi-2D columnar structures is a distinctive feature of rotating turbulence, and has been observed both in experiments [49, 88, 37] and numerical simulations [99, 100, 7]. The formation of columnar structures has been reported also on the case of RB convection by [57]. In the case of BTC we observe a significant correlation between hot (cold) regions and rising (falling) regions in the core of these structures, which results in a strong increase of the heat flux.

In order to investigate quantitatively this phenomenon we proceed as follow. First, we measure the degree of bidimensionalization of the system during an event of strong convection, by studying how much the velocity and temperature fields (at fixed time) are correlated in the vertical direction. For

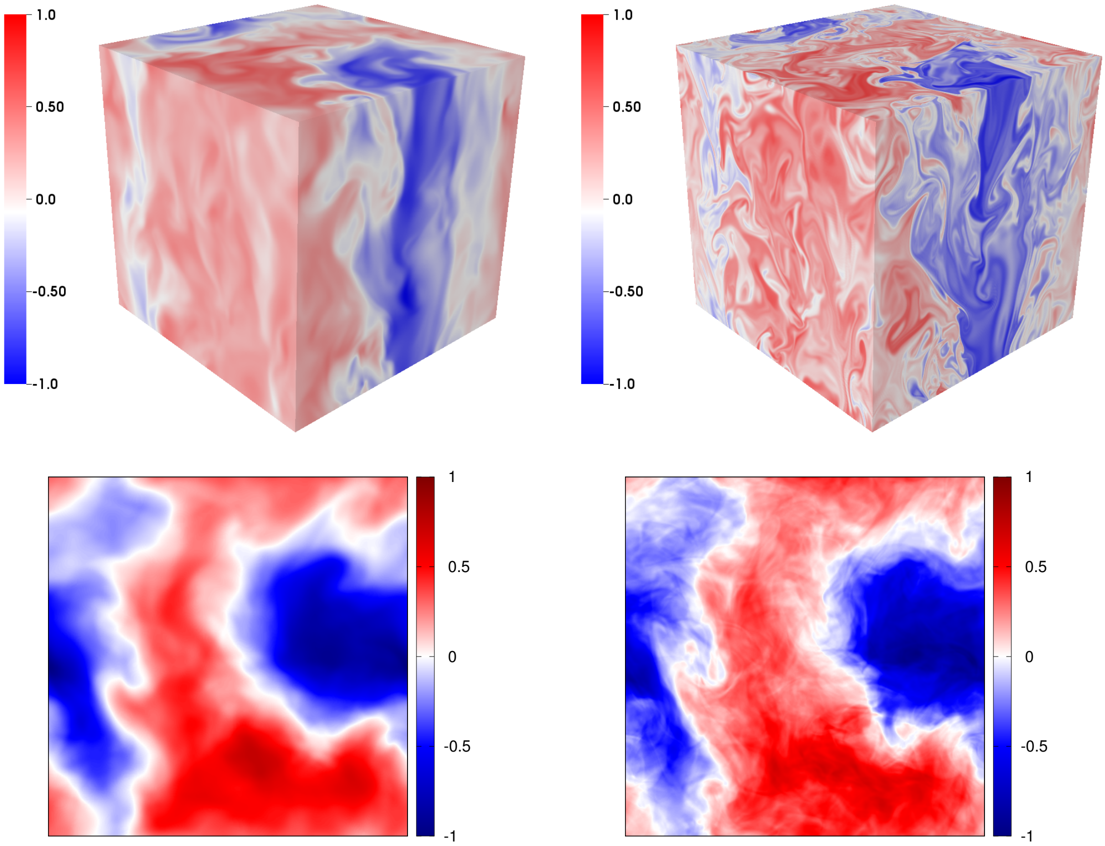

Figure 6.5: Upper panels: Vertical velocity field w (left panel) and temperature fluctuation field θ (right panel) during a strong convective event at time $t = 80\tau$ in the simulation with $Ra = 2.2 \times 10^7$, $Pr = 10$ and $Ro = 5.59 \times 10^{-2}$. Lower panels: Two-dimensional fields w^{2D} (left) and θ^{2D} (right) obtained by averaging the fields w and θ shown above along the vertical direction. Fields are rescaled with maxima of absolute values.

this purpose, we computed the vertical correlation function of u, w, θ and the z-component of the vorticity ω_z:

$$C_u(r) = \langle u(\mathbf{x} + r\hat{\mathbf{e}}_3)\, u(\mathbf{x})\rangle \tag{6.5}$$

$$C_w(r) = \langle w(\mathbf{x} + r\hat{\mathbf{e}}_3)\, w(\mathbf{x})\rangle \tag{6.6}$$

$$C_\theta(r) = \langle \theta(\mathbf{x} + r\hat{\mathbf{e}}_3)\, \theta(\mathbf{x})\rangle \tag{6.7}$$

$$C_{\omega_z}(r) = \langle \omega_z(\mathbf{x} + r\hat{\mathbf{e}}_3)\, \omega_z(\mathbf{x})\rangle \tag{6.8}$$

In Fig. 6.6 we show a comparison of the vertical correlation functions computed in the case of the simulation with $Ra = 2.2 \times 10^7$, $Pr = 10$ and $Ro = 5.59 \times 10^{-2}$ at the same time of the Figure 6.5 ($t = 80\tau$). At variance with the typical columnar vortices observed in rotating turbulence, here we do not find a strong vertical correlation of the z-component of the vorticity (see Fig. 6.6). Also the vertical correlation of horizontal velocity u decays at

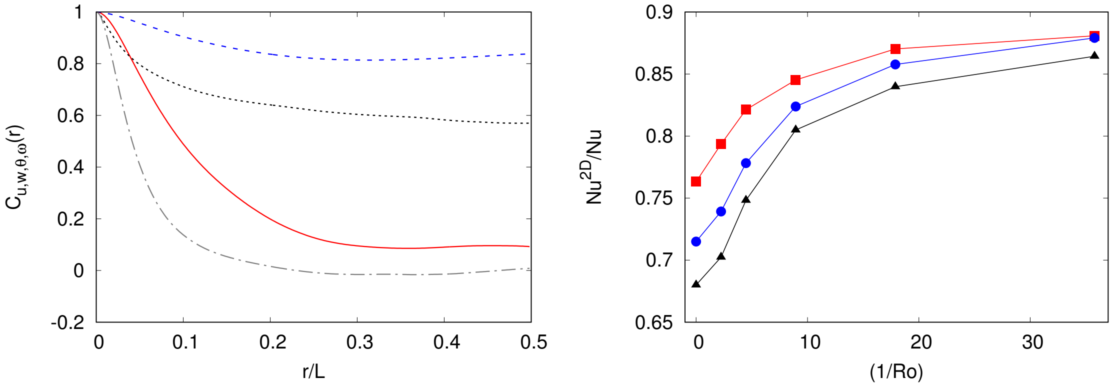

Figure 6.6: Left panel: Correlation function of horizontal velocity $C_u(r)$ (red line), vertical velocity $C_w(r)$ (blue dashed line), temperature $C_\theta(r)$ (black dotted line) and vertical vorticity $C_{\omega_z}(r)$ (grey dash-dotted line) at time $t = 80\tau$ for $Ra = 2.2 \times 10^7$, $Pr = 10$ and $Ro = 5.59 \times 10^{-2}$. Right panel: Ratio Nu^{2D}/Nu as a function of $1/Ro$ for $Ra = 2.2 \times 10^7$, $Pr = 1$ (red squares), $Pr = 5$ (blue circles) and $Pr = 10$ (black triangles)

scales larger than $1/2$ of the box size. Conversely the vertical velocity w and the temperature fields θ remains correlated through the whole domain.

This long-scale, vertical correlation lead us to introduce the $2D$ fields $w^{2D} = \langle w \rangle_z$ and $\theta^{2D} = \langle \theta \rangle_z$, defined as the average along the vertical direction of the respective $3D$ fields. In Fig. 6.5 (lower panels) we show the $2D$ fields of w^{2D} and θ^{2D} obtained for the simulation at $Ra = 2.2 \times 10^7$, $Pr = 10$ and $Ro = 5.59 \times 10^{-2}$ at time $t = 80\tau$, which confirms the spatial correlation between the hot (cold) regions and the rising (falling) regions also in the vertically averaged fields.

Despite the lack of a strong vertical correlation of ω_z, the inspection of the 2D field $\omega_z^{2D} = \langle \omega_z \rangle_z$ reveals a connection between the regions of intense heat flux, which can be identified as thermal convective columns, and cyclonic regions, i.e. those which rotates in the same direction of $\mathbf{\Omega}$. It is possible that the preferential link between convective structures and cyclones could be related with the cyclonic-anticyclonic asymmetry which is observed in rotating turbulence (for a recent review on rotating turbulence see [41]).

Finally, we introduce the $2D$ Nusselt number defined in terms of the $2D$ fields as :

$$Nu^{2D} = \langle \frac{\langle w \rangle_z \langle \theta \rangle_z}{\kappa \gamma} \rangle_{x,y} \tag{6.9}$$

where $\langle \cdots \rangle_{x,y}$ is the average over the horizontal directions x and y. The physical meaning of the ratio Nu^{2D}/Nu is the relative contribution of the 2D modes, i.e. of the columnar structures, to the total heat transport. In Figure 6.6 we show the ratio Nu^{2D}/Nu for the various Pr and Ro simulations at $Ra = 2.2 \times 10^7$. The increase of Nu^{2D}/Nu with the rotation rate demonstrates that in the limit of vanishing Ro the heat transport is dominated by the 2D modes. We also observe a systematic trend as a function of Pr: increasing Pr reduces the contribution of the 2D modes to the heat flux. This effect can be understood in terms of the reduced spatial correlation between the fields w and θ at increasing Pr, as discussed in the previous Section (see Fig. 6.4 and the related discussion).

6.5 Conclusions

We have investigated the behavior of the bulk turbulence convection (BTC) system in a rotating frame by performing extensive DNS of the Boussinesq equations for an incompressible flow in a cubic box with periodic boundary conditions in all directions. In the absence of rotation, we confirmed the consistency of the both Nu and Re scaling with Pr and Ra numbers according to the "ultimate regime of thermal convection" theory [44]. In the presence of rotation, quantified by the Rossby number Ro, we find a surprising strong enhancement of both Nu and Re for intermediate values of Ro followed by a moderate decreases for the largest Ro investigated.

A detailed analysis of the temperature and velocity fields shows that the observed heat flux enhancement at intermediate rotation is due to the formation of columnar convective structures with strong correlations between temperature and vertical velocity.

The understandig of the mechanism behind this phenomenom is still incomplete. In the RB case the non-monotonic increase of Nu is associated with the Ekman pumping and it depends on the modification of the boundary layer caused by rotation. Even if in BTC case the boundary layer is absent we still observe similarities with RB phenomenology. In particular we find a correlation between Nu and vertical velocity variations. Further studies are required in order to improve our knowledge on this phenomenon.

Chapter 7

The Kolmogorov flow in a rotating frame

This chapter is in preparation for submission to a scientific journal.

The work reports a series of massive numerical simulation of the Navier-Stokes equation by studying rotating homogeneous turbulence which occurs in the Kolmogorov flow configuration. In particular, the effects of rotation on the mean flow amplitude and on friction coefficient are investigated.

7.1 Introduction

The Kolmogorov flow is a solution of the Navier Stokes equation in which the flow motion is generated by a steady sinusoidal force that varies in space: this stationary sinusoidal shear has a wavelength equal to the length of the periodic box, where the imposed velocity is usually in the x-direction but depends on the vertical direction. Hence the Kolmogorov flow resulting motion can be considered as homogeneous in each horizontal plane (x,y-direction), but not in the vertical one (z-direction).
Indeed, the flow displays a mean velocity profile that vanishes at the zeroes of the sinusoidal force: near this nodes the velocity profile is approximately linear (Couette flow), while near the maxima of the forcing the flow velocity presents an approximate parabolic profile (Poiseuille flow). This brings to think the basic Kolmogorov flow as the combination of these different profiles forming a series of virtual channels that are not confined by material boundaries and that flow in alternate directions, having their width equal to half of the sinusoidal forcing period. The abscence of boundaries makes the Kolmogorov flow a system that allows to isolate and study the flow bulk properties (i.e. diffusion, turbulent drag) that in other systems can be hidden by the energy that is produced by the wall presence and that is transferred

into the flow, leading to the formation of more complex flow structures.
Even if generating a periodic forcing in an unbounded flow is quite difficult to appear in nature, the Kolmogorov flow is an optimal system for thoretical studies with analytical-numerical treatment and also for laboratory settings and experimental measurements. In spite of its simplicity, the Kolmogorov flow makes a good test case for studying simultaneously inhomogeneous conditions, sheared, and anisotropic features in a flow. This system is also appropriate for conducting investigations on fluid instability together with the transition towards turbulence **??**, stratification problem or viscoelastic solution **??**.

7.2 Kolmogorov flow phenomenology

To describe the Kolmogorov flow we now consider the Navier-Stokes equations:

$$\partial_t u_i + u_j \partial_j u_i = -\partial_i p + \nu \partial^2 u_i + f_i \tag{7.1}$$

with $i = x, y, z$ representing the single components of the incompressible velocity field. The base flow is forced along the x direction by the Kolmogorov body force $f_i = \delta_{i,1} F cos(kz)$ where $k = \frac{1}{L}$ is the wave number associated with the characteristic length L where the forcing acts.
In the laminar regime, when the Re number is below the critical value $Re_c = \sqrt{2}$, the Kolmogorov flow admits the following stationary solution:

$$\boldsymbol{u}(z) = (U_0 cos(kz), 0, 0) \tag{7.2}$$

with the velocity amplitude U_0 which strictly depends on the amplitude of the forcing F, being proportional to the characteristic length L and inversely proportional to the viscosity ν ($U_0 = F/\nu k^2$). The laminar regime allows to study analytically the stability of the system and its transition from laminar to a chaotic regime [64] indeed the laminar solution is found to be always stable for small-scale perturbations (i.e., when the perturbation wave number is greater than the base flow wave number $k = 1/L$) while it becomes unstable for large-scale perturbations (i.e., when the perturbation wave number is smaller than $k = 1/L$) and for $Re > Re_c$ and $Re_c = \sqrt{2}$.
In order to have a transition to a turbulent regime one need to consider high Reynolds number where $Re \gg Re_c$: in this regime the turbulent velocity field can be clearly decomposed in a mean flux U with its turbulent velocity fluctuation u'. Here the Kolmogorov flow shows an interesting property: the mean velocity still presents a monochromatic profile $\overline{u_1(\boldsymbol{x}, t)} = U cos(kz)$ similar to the laminar regime, where the overbar represents the average over the time t and the two horizontal directions x, y. Moreover the new amplitude

of the mean velocity U has a non trivial dependence that cannot be predicted a priori.

Thanks to this property one can still consider the Kolmogorov flow in the turbulent regime, like a series of virtual channels respectively separated by virtual walls where the mean velocity sinusoidal profile is equal to zero. On the other hand, inside each channel, the velocity field presents a sinusoidal profile having a maximum at the center of each virtual channel.

7.2.1 Momentum budget

The momentum budget can be studied by considering the Navier-Stokes equation 7.1 and by taking the space-time average only for the x velocity component that is the only one to be non zero according to the forcing (averages along y and z components are zero because of isotropy due to the absence of forcing term).

After the space-time average operation, the equation can be reduced to a profile equation:

$$\partial_z \overline{(u_x u_z)} = \nu \partial_z^2 \overline{u_x} + f_x \tag{7.3}$$

with $f_x = Fcos(kz)$ being the deterministic sinusoidal forcing. Since the mean velocity profile is also described by a sinusoidal profile, one can make the hypotesis, following 7.3 that all the mean quantities still depend on z according the following relation:

$$\begin{aligned} \partial_z^2 \overline{u_x} &= -k^2 U cos(kz) \\ \overline{\partial_z (u_x u_z)} &= kS cos(kz) \end{aligned} \tag{7.4}$$

which represent respectively the viscous term and the Reynolds stress terms. It is crucial to note that the sinusoidal profile of the Reynolds stress term in 7.4 is not trivial and derives from this hypotesis. Indeed, taking into account that both the viscous and forcing term present a sinusoidal behaviour, this allows to assume that also the Reynolds stress term in the Kolmogorov flow should present a sinusoidal profile depending on z which is monochromatic and with an amplitude S. This property has been observed and verified through numerical simulations results [14].

Hence at this point a simple algebraic relation for the amplitude coefficients of these three scalar quantities can be found as:

$$kS = -\nu k^2 U + F \qquad \rightarrow \qquad F = \frac{S}{L} + \frac{\nu U}{L^2} \tag{7.5}$$

Finally, one can introduce two dimensionless coefficients by defining the friction (or drag) coefficient for the Kolmogorov flow as the ratio between the work done by the sinusoidal forcing and the mean flow kinetic energy:

$$f = \frac{FL}{U^2} \tag{7.6}$$

and the stress coefficient as:

$$\sigma = \frac{S}{U^2}. \tag{7.7}$$

Therefore is possible to rewrite the momentum budget equation 7.5 as

$$f = \sigma + \frac{1}{Re} \tag{7.8}$$

which in the laminar regime, in the fixed point where $S = 0$, brings to the well know friction factor relation with the Reynolds number:

$$f_{lam} = \frac{1}{Re}. \tag{7.9}$$

As long as Reynolds has low values the laminar solution is stable, but when the turbulence increases, the growth of Reynold brings to the instability with the friction factor becoming larger than f_{lam}.

7.3 Rotating Kolmogorov flow

In a rotating frame the Navier-Stokes equation are the following

$$\partial_t \boldsymbol{u} + \boldsymbol{u} \cdot \nabla \boldsymbol{u} = -\frac{1}{\rho}\nabla p + \nu \nabla^2 \boldsymbol{u} + \boldsymbol{f} - 2\boldsymbol{\Omega} \times \boldsymbol{u} \tag{7.10}$$

In this case the dimensionless parameter of $Ro = \frac{U_0}{2\Omega L}$, relating the ratio between the inertial and the Coriolis forces, can be introduced. We can now consider the same Kolmogorov unbounded system where the flow is forced along the x direction as $f_i = \delta_{i,1} F cos(z/L)$ and the system is rotating with a uniform angular velocity $\Omega \hat{z}$ along the vertical direction.

7.3.1 The laminar regime

The presence of the Coriolis force induces a deviation of the initial flow, creating a non-zero component on the other horizontal direction y.
Indeed, considring a rotating frame, the laminar solution becomes

$$\boldsymbol{u}(z) = \left(\frac{U cos(kz)}{1 + Ek^{-2}}, -\frac{Ek^{-1} U cos(kz)}{1 + Ek^{-2}}, 0 \right) \tag{7.11}$$

and depends on the Ekman number defined as $Ek = \nu k^2 / 2\Omega$, which represents the ratio between the viscous force and Coriolis force. Therefore the

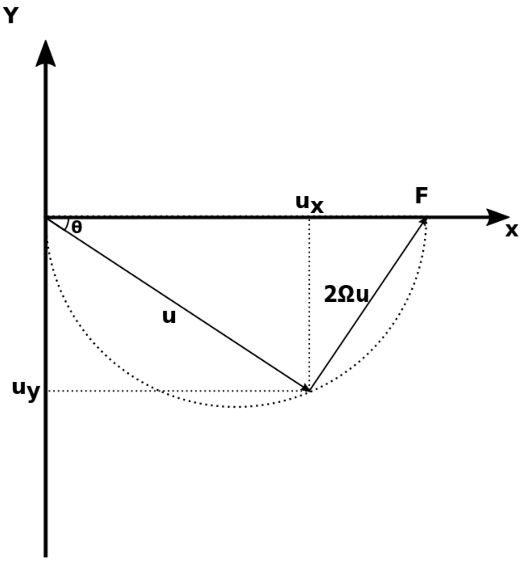

Figure 7.1: Scheme of the vectors direction in the rotating Kolmogorov system: the forcing F is orientated along the x axis, the velocity field is deviated of an angle θ while the second vector component is due to the Coriolis force.

Ekman number can be also expressed as the ratio $Ek = \frac{Ro}{Re}$, indeed the non rotating case is recovered with $Ek \to \infty$.

Even with the presence of rotation, the monochromatic solution is still a Kolmogorov flow, where the direction of the velocity is no more aligned with the external force along x. The velocity is rotated clock-wise by an angle $\theta = arctan(Ek^{-1})$ with respect to the direction of the external force $\boldsymbol{f}$, and also its amplitude intensity is reduced by a factor $(1 + Ek^{-2})^{-1/2}$. Hence the final espression for the velocity is:

$$||\boldsymbol{u}|| = \frac{U|cos(kz)|}{\sqrt{1+Ek^{-2}}}. \tag{7.12}$$

Figure 7.1 outlines the balance, in the laminar regime, between three force vectors which form a triade: the external forcing of amplitude F along the horizontal axis, the viscous force proportional to U and the rotation force proportional to Ω that are orthogonal.

7.3.2 The turbulent regime

Increasing the Reynolds number and considering the transition to the turbulent regime, an analogous of relations 7.11 and 7.12 does not exist. Here an exact expression for the velocity is still missing and needs to be achieved through numerical simulations.

In principle, in the turbulent regime, the balance will be between the three forces contributios of Figure 7.1 with the addition of the Reynolds stress forces. Hence, the momentum budget equation 7.3 in the rotating frame for the two horizontal component can be written as:

$$\partial_z \overline{(u_x u_z)} = \nu \partial_z^2 \overline{u_x} + 2\Omega \overline{u_y} + f_x \tag{7.13}$$

$$\partial_z \overline{(u_y u_z)} = \nu \partial_z^2 \overline{u_y} - 2\Omega \overline{u_x} \tag{7.14}$$

where it is easy to see that the Reynolds stress term will be also divided in two components x, y.

Making the same assumption of 7.4 one can also hypothesize a sinusoidal behavior for the stress forces and write the final relation for the mean quantities:

$$\begin{aligned} \overline{u_x} &= U_x cos(kz) \\ \overline{u_y} &= U_y cos(kz) \\ \overline{u_x u_z} &= S_x sin(kz) \\ \overline{u_y u_z} &= S_y sin(kz) \end{aligned} \tag{7.15}$$

where both the velocity and the stress terms components have different amplitude according to the rotation intensity with their modules being simply $U = \sqrt{U_x^2 + U_y^2}$ and $S = \sqrt{S_x^2 + S_y^2}$.

In first approximation the dominant contribution of the Reynolds stress term can be assumed. Indeed, with this hypothesis, it stands to reason that the viscous dissipation, proportional to U, becomes negligible in comparison with the stress force vector of module S.

Furthermore, making a second assumption according to which these two vectors remain aligned in the same direction, a similar triadic relation as in Fig. 7.1 of the laminar case can be recovered, with the stress vector replacing the viscous term.

In this case, the prediction for the deviating rotation angle can be obtained as:

$$tan(\theta) = \frac{2\Omega UL}{\sigma U^2} = \frac{1}{\sigma EkRe} \propto \frac{1}{Ro} \tag{7.16}$$

Now, substituting the mean quantites 7.15 in the two components of the momentum budget equation 7.13 and 7.14 one can obtain the following relations:

$$\frac{S_x}{L} + \frac{\nu}{L^2} u_x = 2\Omega u_y + F \tag{7.17}$$

$$\frac{S_y}{L} + \frac{\nu}{L^2} u_y = -2\Omega u_x \tag{7.18}$$

Finally, if the velocity and stress vectors are aligned, starting from 7.17 and 7.18, the sum squared of the two components brings to the compact relation:

$$\left(\frac{S}{L} + \frac{\nu U}{L^2} \right)^2 + 4\Omega^2 U^2 = F^2 \tag{7.19}$$

that can be rewritten in terms of adimensional parameters as

$$\left(\sigma + \frac{1}{Re}\right)^2 + \frac{1}{Ro^2} = f^2 \tag{7.20}$$

However, an alignment between the stress and the velocity vectors cannot be predicted a priori and needs to be studied in detail (see 7.5). The main results are presented hereafter.

7.4 Numerical simulations and modelling

We performed extensive Direct Numerical Simulations of the Navier-Stokes equation under rotation

$$\partial_t \boldsymbol{u} + \boldsymbol{u} \cdot \nabla \boldsymbol{u} = -\frac{1}{\rho} \nabla p + \nu \nabla^2 \boldsymbol{u} + \boldsymbol{f} - 2\boldsymbol{\Omega} \times \boldsymbol{u} \tag{7.21}$$

in a cubic domain of size $L_{box} = 2\pi$ with periodic boundary conditions, fixed viscosity, Kolmogorov forcing at the scale $L = 1$ and different values of the forcing amplitude F. Starting from a turbulent statistically stationary state, reached after several large-scale eddy turnover times $T = \langle \boldsymbol{u}^2 \rangle / 2\epsilon$, the Coriolis force is turned on and the same rotation regime is explored for each forced flow.

In order to compute the mean profiles from which to obtain the amplitudes by fitting equations 7.15, a solid statistics (i.e., good convergence of mean quantities with an average over many T) is needed. Finally, after the rotating system reaches a stationary regime, the other statistical properties of the flow can be computed. Since the value of F determines different velocity amplitudes, and therefore diverse Reynolds number. This required the use of different resolutions of the cubic domain to be simulated.

Moreover, several increasing rotation intensities are explored for each different forcing, taking care to explore the same Rossby number range in every simulation series. Since rotation induces a reduction of the velocity fields, we choose rotation intensities that still allow a turbulent regime in the system. To clarify, all simulation parameters are shown in Table 7.1.

F	Re	Ω	U	ϵ	η	τ_η	T
0.008	220	0.005	0.22	9×10^{-4}	3.25×10^{-2}	1.05	35.0
0.008	188	0.01	0.19	7×10^{-4}	3.46×10^{-2}	1.19	38.4
0.008	129	0.02	0.13	4×10^{-4}	3.98×10^{-2}	1.58	43.0
0.008	95	0.04	0.09	2×10^{-4}	4.73×10^{-2}	2.24	47.5
0.512	1984	0.005	1.98	5.08×10^{-1}	6.66×10^{-3}	0.045	4.91
0.512	1734	0.05	1.73	4.33×10^{-1}	6.93×10^{-3}	0.048	4.94
0.512	1399	0.1	1.40	3.30×10^{-1}	7.41×10^{-3}	0.055	5.17
0.512	869	0.2	0.87	1.41×10^{-1}	9.16×10^{-3}	0.084	6.71
0.512	768	0.3	0.77	8.63×10^{-2}	1.04×10^{-2}	0.11	8.10
1.024	2013	0.125	2.01	5.09×10^{-1}	6.65×10^{-3}	0.044	6.97
1.024	1368	0.25	1.37	4.81×10^{-1}	6.75×10^{-3}	0.046	4.51
1.024	1119	0.5	1.12	2.51×10^{-1}	7.95×10^{-3}	0.063	5.82

Table 7.1: Parameters of the simulations: F is the amplitude of the forcing, $U = \sqrt{U_x^2 + U_y^2}$ is the amplitude of the mean velocity profile, $Ro = U/2\Omega L$, $Re = UL/\nu$, $\epsilon = \nu\langle(\partial \boldsymbol{u})\rangle$ is the mean energy dissipation, $\eta = (\nu^3/\epsilon)^{1/4}$ is the Kolmogorov scale, $\tau_\eta = (\nu/\epsilon)^{1/2}$ is the Kolmogorov time scale, and $T = \langle \boldsymbol{u}^2\rangle/2\epsilon$ is the large-scale eddy turnover time. The viscosity $\nu = 10^{-3}$ and the integral scale $L = 1$ are fixed for all simulation. Simulations with forcing $F = 0.008$ are done at resolution $N = 128$, $F = 0.512$ at $N = 512$, and $F = 1.024$ at high resolution $N = 1024$.

7.5 Results

We firstly analyse vertical profiles computing ensemble average for both the velocity and Reynolds stress components, in each forced simulation and for every rotation intensity. As one can observe from figure 7.2 the two velocity components present a cosine profile, reaching maxima at the boundaries and in the middle of the cubic domain (i.e, $L_z = 0 = 2\pi$ and $L_z = \pi$). Viceversa the mean stress component profiles are well approximated by a sinusoidal function being clearly null in association of the maxima energy input values and becoming important in the inversion velocity regions (i.e., virtual channels boundary).

Hence the hypothesis of equation 7.15 is justified and both the sinusoidal behaviours are verified. This allows to introduce the velocity and stress vectors defining their modules as $U = \sqrt{U_x^2 + U_y^2}$ and $S = \sqrt{S_x^2 + S_y^2}$.

We now focus on the study of the rotating turbulent behavior, studying in particular on the friction coefficient $f = FL/U^2$ and the stress coefficient $\sigma = S/U^2$ and their dependence on $Ro = \frac{U}{2\Omega L}$ rotation parameter.

Our numerical simulations start from the work of [69] where fully develeped regime is reached in a Kolmogorov flow system in absence of rotation. Indeed, the black and magenta lines shown in Figure 7.3, respectively represent the friction factor f and the stress coefficient σ dependence on Re number in a non-rotating domain. According to 7.8, in absence of rotation, their

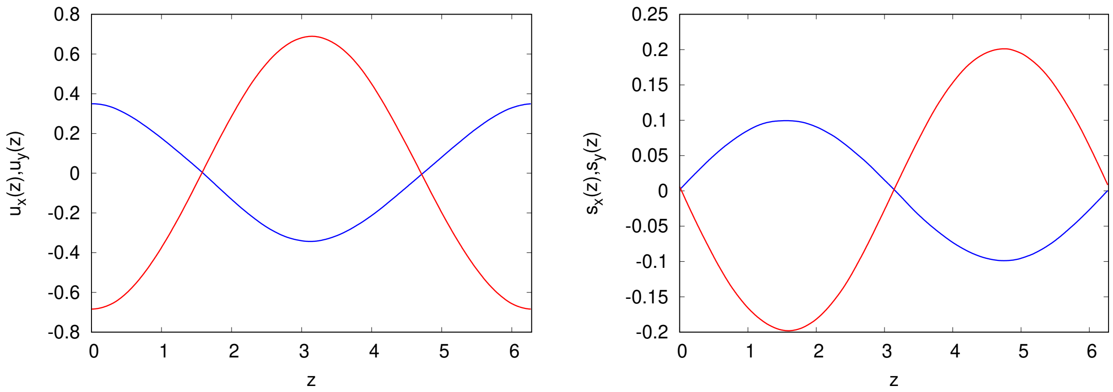

Figure 7.2: The figure show an example of vertical averaged profiles for the velocity component (left panel) and stress vectors components (right panel). Blue lines represent the x component while red lines indicate y component.

variation is always equal to the inverse Reynolds number while, as one can see from the figure, they follow to a good approximation a relation of the type $a+\frac{b}{Re}$ with coefficients a and b properly obtained from fitting equations (see [69]).

As previously said, the aim of the work is to study the physical behaviour of friction and stress coefficient in presence of rotation. In Figure 7.3 are shown the two coefficient, f and σ, as a function of Re, where different symbols represent the three different forcing $F = 0.008$, $F = 0.512$ and $F = 1.024$ while each dot represents a different rotation intensity explored in simulations.

Physically, as rotation increases, the amplitude of the mean flow velocity decreases leading to an increase in the friction factor according the exact relation $f = \frac{C}{Re^2}$. Indeed, starting from the definition of f and writing the velocity in terms of the Reynolds number, the previous relation can be obtained with the constant $C = \frac{FL^3}{\nu^2}$. The three curves (blue, red and green) represent the behaviour of f which is verified to be a curve $\propto 1/Re^2$, here shown in a log scale.

Moreover, another information is given by the Figure 7.4 where, in the left panel, the two coefficients behaviour is plotted as a function of the Rossby parameter. Here as long as the rotation increases, the growth of both f and σ is confirmed. Furthermore, the other interesting result is that all data of the friction coefficient f at different forcing present the same decreasing dependence with Rossby, showing a collapse of their curves. The same thing, with a different behavior, occurs for the stress coefficient σ. The above mentioned collapse could indicate that we have reached the same asymptotic regime expected at high Reynolds.

On the right panel of Figure 7.4 we show the decrease of the Reynolds number

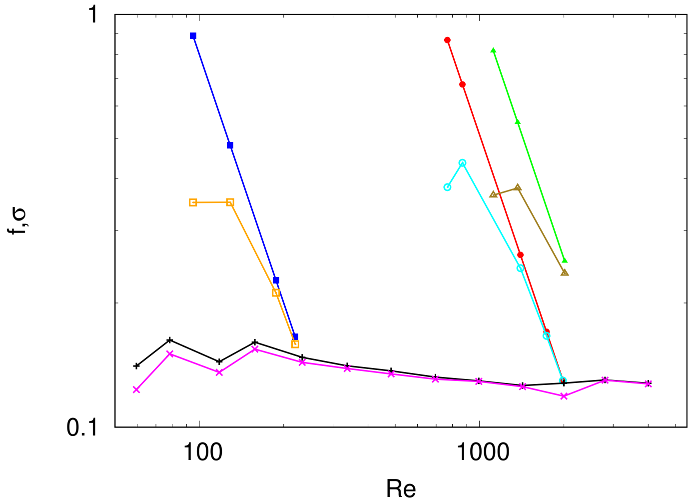

Figure 7.3: Three different simulated external forcing in presence of rotation are shown: the external forcing $F = 0.008$ (squares), forcing at $F = 0.512$ (circles) and forcing $F = 1.024$ (triangles). All filled symbols are referring to the friction factor $f = FL/U^2$ (respectively the blue, red and green lines) while the empty symbols refer to the stress coefficient $\sigma = S/U^2$ (respectively the orange, cyan and olive line). Black and magenta series refer to the work [69] where f and σ dependence on Reynolds is studied in absence of rotation.

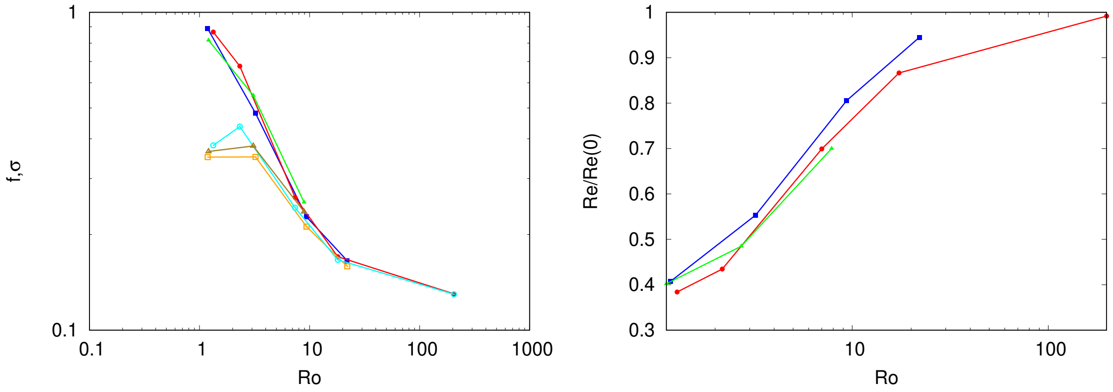

Figure 7.4: Left panel: Friction factor f and stress coefficient σ dependence on rotation (Ro number) at three different forcing of the flow ($F = 0.008$, $F = 0.512$ and $F = 1.024$). Symbols as in Figure 7.3. Right panel: Re dependence on rotation. The Re values are normalized with their corresponding $Re(0)$ in absence of rotation. Different symbols for the three external forcings as in Figure 7.3.

with the increasing rotation, due to the suppression of velocities. We show the Re normalized with its value $Re(0)$ in a fully turbulent system in absence of rotation: even if diverse external forces produce different velocity fields, by decreasing the Rossby number the same relatively decrease of Reynolds is achieved in all simulations and a collapse of the curves is obtained. This indicates that the same regime is therefore investigated.

However, it is important to note that, considering absolute Reynolds values, even for the simulation presenting the maximum of rotation and the minimum external forcing, a fully developed turbulent regime still persists. This can be also verified from values of the Re number in table 7.1.

Finally we investigate if, with the action of rotation, the amplitude of mean velocity and the stress vectors can still present an alignment in terms of the angle direction. We can firtsly define the angles $\theta_U = atan(\frac{U_y}{U_x})$ formed by the velocity vector components u_x and u_y together with the angular values of $\theta_S = atan(\frac{S_y}{S_x})$ and then we study their dependence with the rotation intensity. The increasing of rotation should bring to a growth of the angles deviation.

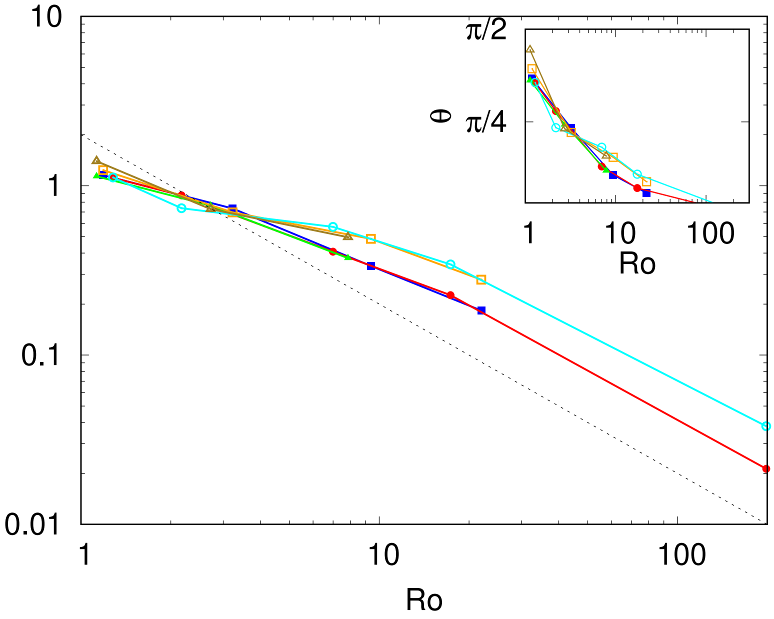

Figure 7.5: Velocity vector angles θ_u (filled symbols) and stress vector angles θ_S (empty symbols) dependence on the Ro number at three differente forcing. Symbols shape and line colours as in Figure 7.3. The dashed line represents the prediction 7.16 where $tan(\theta) \propto 1/Ro$.

Results are presented in Figure 7.5 where the inset shows that both θ_U and θ_S have their values between 0 and $\pi/2$. In the limit of $Ro \to \infty$ the Kolmogorov in absence of rotation is recovered, presenting vanishing angular values. Here, both the stress and velocity vectors tend to orient aligning along the external force direction. Furthermore, at low rotation, also the relative difference between the two angles is vanishing.

As long as rotation increases both angles orientation present a behaviour that follows the prediction of 7.16 (black dashed line $\propto 1/Ro$) confirming the hypothesis that the vector directions remain aligned within the error bars. To better understand the behaviour, angles of Figure 7.5 are displayed in a logarithmic scale.

Afterwards, angles continue their growth up to be identical at an intermediate Rossby number where their values measure $\theta = \pi/4$. Finally, at very low Rossby numbers, the rotation hugely impacts on the velocity field which ends in a significant reduction of the amplitude U, with an increase in the measurements uncertainty, and a theoretical prediction is still missing.

For this reason the behaviour at very high rotations is not totally understood and further studies need to be conducted in order to have a better comprehension of the system.

7.6 Conclusions

After a theoretical description of the Kolmogorov flow, we investigated the system under a rotating regime by performing Direct Numerical Simulation of the Navier-Stokes equations in a cubic box with periodic boundary conditions subjected to rotation. Firstly, even in a rotating turbulent regime, the mean profiles of velocity and stress vectors can be still represented with sinusoidal function.

The dependence of the friction factor f and the stress coefficient σ, in presence of a growing rotation, is studied showing a curve collapse of their behaviours and confirming the quantities growth according to the physics of the system: the velocity amplitude decrease with the rise of rotation, hence the friction factor shows the same kind of increment at different forcing.

Moreover, the angular orientation of the velocity vector and the Reynolds stress vector is investigated for a wide range of rotation intensities. An alignment of these quantities is observed for very low rotation, where the stress and velocity vectors align along the forcing direction. The range of intermediate rotation still presents an alignment with a grow of the angular deviation which follows the theoretical prediction 7.16.

Neverthelss, further studies need to be conducted for the range of high rotations which acts highly suppressing the velocity fields resulting in a significant suppression of its amplitude. Here a theoretical description is still missing.

Bibliography

[1] G. Ahlers, S. Grossmann, and D. Lohse. Heat transfer and large scale dynamics in turbulent Rayleigh-Bénard convection. *Rev. Mod. Phys.*, 81:503, 2009.

[2] K. A. Baldwin, M. M. Scase, and R. J. Hill. The inhibition of the Rayleigh-Taylor instability by rotation. *Sci. Rep.*, 5:11706, 2015.

[3] P. Bartello, O. Métais, and M. Lesieur. Coherent structures in rotating three-dimensional turbulence. *J. Fluid Mech.*, 273:1–29, 1994.

[4] G. K. Batchelor. Computation of the energy spectrum in homogeneous two-dimensional turbulence. *Phys. Fluids*, 12(12):II–233–II–239, 1969.

[5] F. Bellet, F. Godeferd, J. Scott, and C. Cambon. Wave turbulence in rapidly rotating flows. *J. Fluid Mech.*, 562:83–121, 2006.

[6] H. Ben-Gida, R. Gurka, and A. Liberzon. Openpiv-matlab—an open-source software for particle image velocimetry; test case: Birds' aerodynamics. *SoftwareX*, 12:100585, 2020.

[7] L. Biferale, F. Bonaccorso, I. M. Mazzitelli, M. A. T. van Hinsberg, A. S. Lanotte, S. Musacchio, P. Perlekar, and F. Toschi. Coherent structures and extreme events in rotating multiphase turbulent flows. *Phys. Rev. X*, 6:041036, 2016.

[8] D. Biskamp. *Nonlinear magnetohydrodynamics*. Cambridge University Press, 1997.

[9] E. Bodenschatz, W. Pesch, and G. Ahlers. Recent developments in Rayleigh-Bénard convection. *Annu. Rev. Fluid Mech.*, 32:709–778, 2000.

[10] G. Boffetta, F. De Lillo, A. Mazzino, and L. Vozella. The ultimate state of thermal convection in Rayleigh–Taylor turbulence. *Physica D*, 241:137–140, 2012.

[11] G. Boffetta and A. Mazzino. Incompressible Rayleigh–Taylor turbulence. *Annu. Rev. Fluid Mech.*, 49:119–143, 2017.

[12] G. Boffetta, A. Mazzino, and S. Musacchio. Effects of polymer additives on Rayleigh-Taylor turbulence. *Phys. Rev. E*, 83:056318, 2011.

[13] G. Boffetta, A. Mazzino, and S. Musacchio. Rotating Rayleigh-Taylor turbulence. *Phys. Rev. Fluids*, 1:054405, 2016.

[14] V. Borue and S. A. Orszag. Numerical study of three-dimensional kolmogorov flow at high reynolds numbers. *J. Fluid Mech.*, 306:293–323, 1996.

[15] V. Borue and S. A. Orszag. Turbulent convection driven by a constant temperature gradient. *J. Scientific Comp.*, 12:305–351, 1997.

[16] L. Bourouiba and P. Bartello. The intermediate rossby number range and two-dimensional–three-dimensional transfers in rotating decaying homogeneous turbulence. *J. Fluid Mech.*, 587:139–161, 2007.

[17] J. Braithwaite. *Essential Fluid Dynamics: For Scientists*. Morgan & Claypool Publishers, 2017.

[18] E. Brown, A. Nikolaenko, D. Funfschilling, and G. Ahlers. Heat transport in turbulent Rayleigh-Bénard convection: Effect of finite top-and bottom-plate conductivities. *Phys. Fluids*, 17:075108, 2005.

[19] F. H. Busse. Convection driven zonal flows and vortices in the major planets. *Chaos*, 4:123, 1994.

[20] E. Calzavarini, D. Lohse, F. Toschi, and R. Tripiccione. Rayleigh and Prandtl number scaling in the bulk of Rayleigh–Bénard turbulence. *Phys. Fluids*, 17:055107, 2005.

[21] A. Celani, S. Musacchio, and D. Vincenzi. Turbulence in more than two and less than three dimensions. *Phys. Rev. Lett.*, 104(18):184506, 2010.

[22] D. C. Champeney and R. M. Fuoss. Fourier transforms and their physical applications. *Phys. Today*, 26(10):57, 1973.

[23] S. Chandrasekhar. Hydromagnetic and Hydrodynamic Stability. *Clarendon, Oxford*, 1961.

[24] A. G. Chatterjee, M. K. Verma, A. Kumar, R. Samtaney, B. Hadri, and R. Khurram. Scaling of a fast fourier transform and a pseudo-spectral fluid solver up to 196608 cores. *J. Parallel Distrib. Comput.*, 113:77–91, 2018.

[25] J. S. Cheng, S. Stellmach, A. Ribeiro, A. Grannan, E. M. King, and J. M. Aurnou. Laboratory-numerical models of rapidly rotating convection in planetary cores. *Geophys. J. Int.*, 201(1):1–17, 2015.

[26] M. Chertkov, C. Connaughton, I. Kolokolov, and V. Lebedev. Dynamics of energy condensation in two-dimensional turbulence. *Phys. Rev. Lett.*, 99(8):084501, 2007.

[27] J. Y. N. Cho and E. Lindborg. Horizontal velocity structure functions in the upper troposphere and lower stratosphere: 1. observations. *Journal of Geophysical Research: Atmospheres*, 106(D10):10223–10232, 2001.

[28] K. L. Chong, Y. Yang, S.-D. Huang, J.-Q. Zhong, R. J. A. M. Stevens, R. Verzicco, D. Lohse, and K.-Q. Xia. Confined Rayleigh-Bénard, Rotating Rayleigh-Bénard, and Double Diffusive Convection: A unifying view on turbulent transport enhancement through coherent structure manipulation. *Phys. Rev. Lett.*, 119:064501, 2017.

[29] J. W. Cooley and J. W. Tukey. An algorithm for the machine calculation of complex fourier series. *Math. Comput.*, 19(90):297–301, 1965.

[30] P. A. Davidson, P. J. Staplehurst, and S. B. Dalziel. On the evolution of eddies in a rapidly rotating system. *J. Fluid Mech.*, 557:135, 2006.

[31] D. Deirmendjian. Electromagnetic scattering on spherical polydispersions. Technical report, Rand Corp Santa Monica CA, 1969.

[32] E. Deusebio, G. Boffetta, E. Lindborg, and S. Musacchio. Dimensional transition in rotating turbulence. *Phys. Rev. E*, 90(2):023005, 2014.

[33] P. F. Embid and A. J. Majda. Low froude number limiting dynamics for stably stratified flow with small or finite rossby numbers. *Geophysical & Astrophysical Fluid Dynamics*, 87(1-2):1–50, 1998.

[34] E. Ferrero, L. Mortarini, M. Manfrin, A. Longhetto, R. Genovese, and R. Forza. Boundary-layer stress instabilities in neutral, rotating turbulent flows. *Boundary Layer Meteorol.*, 130(3):347, 2009.

[35] I. T. Foster and P. H. Worley. Parallel algorithms for the spectral transform method. *SIAM J. Sci. Comput.*, 18(3):806–837, 1997.

[36] U. Frisch. *Turbulence: the legacy of AN Kolmogorov*. Cambridge university press, 1995.

[37] B. Gallet, A. Campagne, P.-P. Cortet, and F. Moisy. Scale-dependent cyclone-anticyclone asymmetry in a forced rotating turbulence experiment. *Phys. Fluids*, 26:035108, 2014.

[38] B. Gallet, A. Campagne, P.-P. Cortet, and F. Moisy. Scale-dependent cyclone-anticyclone asymmetry in a forced rotating turbulence experiment. *Phys. Fluids*, 26(3):035108, 2014.

[39] J.-N. Gence and C. Frick. Naissance des corrélations triples de vorticité dans une turbulence statistiquement homogène soumise à une rotation. *Comptes Rendus de l'Académie des Sciences-Series IIB-Mechanics*, 329(5):351–356, 2001.

[40] F. S. Godeferd and L. Lollini. Direct numerical simulations of turbulence with confinement and rotation. *J. Fluid Mech.*, 393:257–308, 1999.

[41] F. S. Godeferd and F. Moisy. Structure and dynamics of rotating turbulence: a review of recent experimental and numerical results. *Appl. Mech. Rev.*, 67(3):030802, 2015.

[42] H. H. Goldstine. *A History of Numerical Analysis from the 16th through the 19th Century*, volume 2. Springer Science & Business Media, 2012.

[43] H. P. Greenspan. *The theory of rotating fluids*. CUP Archive, 1968.

[44] S. Grossmann and D. Lohse. Scaling in thermal convection: a unifying theory. *J. Fluid Mech.*, 407:27–56, 2000.

[45] S. Grossmann and D. Lohse. Fluctuations in turbulent Rayleigh–Bénard convection: the role of plumes. *Phys. Fluids*, 16:4462–4472, 2004.

[46] C. Guervilly, D. W. Huges, and C. A. Jones. Large-scale vortices in rapidly rotating rayleigh-bénard convection. *J. Fluid Mech.*, 758:407–435, 2014.

[47] G. J. Hakim and A. K. Canavan. Observed cyclone–anticyclone tropopause vortex asymmetries. *J. Atmos. Sci.*, 62(1):231–240, 2005.

[48] D. L. Hartmann, L. A. Moy, and Q. Fu. Tropical convection and the energy balance at the top of the atmosphere. *J. Climate*, 14:4495–4511, 2001.

[49] E. J. Hopfinger, F. K. Browand, and Y. Gagne. Turbulence and waves in a rotating tank. *J. Fluid Mech.*, 125:505–534, 1982.

[50] L. Jacquin, O. Leuchter, C. Cambonxs, and J. Mathieu. Homogeneous turbulence in the presence of rotation. *J. Fluid Mech.*, 220:1–52, 1990.

[51] J. P. Johnston. Effects of system rotation on turbulence structure: a review relevant to turbomachinery flows. *Int. J. Rotating Mach.*, 4:97–112, 1998.

[52] K. Julien, S. Legg, J. McWilliams, and J. Werne. Hard turbulence in rotating Rayleigh-Bénard convection. *Phys. Rev. E*, 53:R5557, 1996.

[53] E. M. King, S. Stellmach, J. Noir, U. Hansen, and J. M. Aurnou. Boundary layer control of rotating convection systems. *Nature*, 457:301, 2009.

[54] R. H. Kraichnan. Turbulent thermal convection at arbitrary Prandtl number. *Phys. Fluids*, 5:1374–1389, 1962.

[55] R. H. Kraichnan. Inertial ranges in two-dimensional turbulence. *Phys. Fluids*, 10(7):1417–1423, 1967.

[56] R. P. J. Kunnen, H. J. H. Clercx, and B. J. Geurts. Breakdown of large-scale circulation in turbulent rotating convection. *Europhys. Lett.*, 84:24001, 2008.

[57] R. P. J. Kunnen, H. J. H. Clercx, and B. J. Geurts. Vortex statistics in turbulent rotating convection. *Phys. Rev. E*, 82:036306, 2010.

[58] R. P. J. Kunnen, R. J. A. M. Stevens, J. Overkamp, C. Sun, G. F. van Heijst, and H. J. H. Clercx. The role of Stewartson and Ekman layers in turbulent rotating Rayleigh–Bénard convection. *J. Fluid Mech.*, 688:422–442, 2011.

[59] M. Li, C. Garrett, and E. Skyllingstad. A regime diagram for classifying turbulent large eddies in the upper ocean. *Deep Sea Res. Part I*, 52(2):259–278, 2005.

[60] M. J. Lighthill and J. Lighthill. Waves in fluids cambridge university press cambridge, 1978.

[61] D. Lohse and F. Toschi. Ultimate state of thermal convection. *Phys. Rev. Lett.*, 90:034502, 2003.

[62] A. Longhetto, L. Montabone, A. Provenzale, H. Didelle, C. Giraud, D. Bertoni, and R. Forza. Coherent vortices in rotating flows: a laboratory view. *Nuovo Cimento Soc. Ital. Fis., C*, 25(2), 2002.

[63] J. Marshall and F. Schott. Open-ocean convection: Observations, theory, and models. *Rev. Geophys.*, 37:1–64, 1999.

[64] L. D. Meshalkin and I. G. Sinai. Investigation of the stability of a stationary solution of a system of equations for the plane movement of an incompressible viscous liquid. *J. Appl. Math. Mech.*, 25(6):1700–1705, 1961.

[65] M. S. Miesch. The coupling of solar convection and rotation. In *Hel. Diag. Solar Conv. Act.*, pages 59–89. Springer, 2000.

[66] F. Moisy, C. Morize, M. Rabaud, and J. Sommeria. Decay laws, anisotropy and cyclone–anticyclone asymmetry in decaying rotating turbulence. *J. Fluid Mech.*, 666:5–35, 2011.

[67] C. Morize and F. Moisy. Energy decay of rotating turbulence with confinement effects. *Phys. Fluids*, 18(6):065107, 2006.

[68] C. Morize, F. Moisy, and M. Rabaud. Decaying grid-generated turbulence in a rotating tank. *Phys. Fluids*, 17(9):095105, 2005.

[69] S. Musacchio and G. Boffetta. Turbulent channel without boundaries: The periodic kolmogorov flow. *Phys. Rev. E*, 89(2):023004, 2014.

[70] S. Musacchio and G. Boffetta. Condensate in quasi-two-dimensional turbulence. *Physical Review Fluids*, 4(2):022602, 2019.

[71] A. Naso. Cyclone-anticyclone asymmetry and alignment statistics in homogeneous rotating turbulence. *Phys. Fluids*, 27(3):035108, 2015.

[72] S. Nazarenko. *Wave turbulence*, volume 825. Springer Science & Business Media, 2011.

[73] J. J. Niemela, S. Babuin, and K. R. Sreenivasan. Turbulent rotating convection at high Rayleigh and Taylor numbers. *J. Fluid Mech.*, 649:509–522, 2010.

[74] V. V. Nosov, V. M. Grigoriev, P. G. Kovadlo, V. P. Lukin, E. V. Nosov, and A. V. Torgaev. Coherent structures in turbulent atmosphere. In *Fifteenth International Symposium on Atmospheric and Ocean Optics/Atmospheric Physics*, volume 7296, page 729609. International Society for Optics and Photonics, 2009.

[75] D. Pekurovsky. P3dfft: A framework for parallel computations of fourier transforms in three dimensions. *SIAM J. Sci. Comput.*, 34(4):C192–C209, 2012.

[76] P. Perlekar and R. Pandit. Statistically steady turbulence in thin films: direct numerical simulations with ekman friction. *New J. Phys.*, 11(7):073003, 2009.

[77] N. A. Phillips. Geostrophic motion. *Rev. Geophys.*, 1(2):123–176, 1963.

[78] O. Praud, J. Sommeria, and A. M. Fincham. Decaying grid turbulence in a rotating stratified fluid. *J. Fluid Mech.*, 547:389–412, 2006.

[79] M. Raffel, C. E. Willert, F. Scarano, C. J. Kähler, S. T. Wereley, and J. Kompenhans. *Particle image velocimetry: a practical guide*. Springer, 2018.

[80] S. Rahmstorf. The thermohaline ocean circulation: A system with dangerous thresholds? *Climatic Change*, 46(3):247–256, 2000.

[81] O. Reynolds. An experimental investigation of the circumstances which determine whether the motion of water shall be direct or sinuous, and of the law of resistance in parallel channels. *Phil. Trans. R. Soc. London*, pages 935–982, 1883.

[82] H. T. Rossby. A study of Bénard convection with and without rotation. *J. Fluid Mech.*, 36:309–335, 1969.

[83] L. M. Smith and Y. Lee. On near resonances and symmetry breaking in forced rotating flows at moderate rossby number. *J. Fluid Mech.*, 535:111–142, 2005.

[84] L. M. Smith and F. Waleffe. Transfer of energy to two-dimensional large scales in forced, rotating three-dimensional turbulence. *Phys. Fluids*, 11(6):1608–1622, 1999.

[85] L. M. Smith and V. Yakhot. Bose condensation and small-scale structure generation in a random force driven 2d turbulence. *Phys. Rev. Lett.*, 71(3):352, 1993.

[86] M. Sprague, K. Julien, E. Knobloch, and J. Werne. Numerical simulation of an asymptotically reduced system for rotationally constrained convection. *J. Fluid Mech.*, 551:141–174, 2006.

[87] B. Sreenivasan and P. A. Davidson. On the formation of cyclones and anticyclones in a rotating fluid. *Phys. Fluids*, 20(8):085104, 2008.

[88] P. J. Staplehurst, P. A. Davidson, and S. B. Dalziel. Structure formation in homogeneous freely decaying rotating turbulence. *J. Fluid Mech.*, 598:81–105, 2008.

[89] R. J. A. M. Stevens, H. J. H. Clercx, and D. Lohse. Optimal Prandtl number for heat transfer in rotating Rayleigh–Bénard convection. *New J. Phys.*, 12:075005, 2010.

[90] R. J. A. M. Stevens, H. J. H. Clercx, and D. Lohse. Heat transport and flow structure in rotating Rayleigh–Bénard convection. *Eur. J. Mech. B/Fluids*, 40:41–49, 2013.

[91] R. J. A. M. Stevens, J. Overkamp, D. Lohse, and H. J. H. Clercx. Effect of aspect ratio on vortex distribution and heat transfer in rotating Rayleigh-Bénard convection. *Phys. Rev. E*, 84:056313, 2011.

[92] R. J. A. M. Stevens, R. Verzicco, and D. Lohse. Radial boundary layer structure and Nusselt number in Rayleigh–Bénard convection. *J. Fluid Mech.*, 643:495–507, 2010.

[93] R. J. A. M. Stevens, J.-Q. Zhong, H. J. H. Clercx, G. Ahlers, and D. Lohse. Transitions between turbulent states in rotating Rayleigh-Bénard convection. *Phys. Rev. Lett.*, 103:024503, 2009.

[94] P. Tabeling, S. Burkhart, O. Cardoso, and H. Willaime. Experimental study of freely decaying two-dimensional turbulence. *Phys. Rev. Lett.*, 67(27):3772, 1991.

[95] Z. J. Taylor, R. Gurka, G. A. Kopp, and A. Liberzon. Long-duration time-resolved piv to study unsteady aerodynamics. *IEEE Trans. Instrum. Meas.*, 59(12):3262–3269, 2010.

[96] L. J. A. Van Bokhoven, C. Cambon, L. Liechtenstein, F. S. Godeferd, and H. J. H. Clercx. Refined vorticity statistics of decaying rotating three-dimensional turbulence. *J. Turbul.*, page N6, 2008.

[97] P. Vorobieff and R. E. Ecke. Vortex structure in rotating rayleigh-benard convection. *Physica D*, 123(1-4):153–160, 1998.

[98] J. M. Wallace and P. V. Hobbs. *Atmospheric science: an introductory survey*, volume 92. Elsevier, 2006.

[99] P. K. Yeung and Y. Zhou. Numerical study of rotating turbulence with external forcing. *Phys. Fluids*, 10:2895–2909, 1998.

[100] K. Yoshimatsu, M. Midorikawa, and Y. Kaneda. Columnar eddy formation in freely decaying homogeneous rotating turbulence. *J. Fluid Mech.*, 677:154–178, 2011.

[101] Z. Zhang, Y. Lu, and H. Hsu. Detecting ocean currents from satellite altimetry, satellite gravity and ocean data. In *Dynamic Planet*, pages 17–22. Springer, 2007.

[102] J.-Q. Zhong, R. J. A. M. Stevens, H. J. H. Clercx, R. Verzicco, D. Lohse, and G. Ahlers. Prandtl-, Rayleigh-, and Rossby-number dependence of heat transport in turbulent rotating Rayleigh-Bénard convection. *Phys. Rev. Lett.*, 102:044502, 2009.